University of Crete

Department of Physics

Institute of Electronic Structure and Laser

Master Thesis

Vardakis Konstantinos

Optical Techniques to Enhance the Sensitivity of Optical Microscopy

Supervisor of the Master Thesis: Prof. Dimitris G. Papazoglou

Comittee Members: Dr. Von Klitzing Wolf

Prof. Rakitzis Peter

Graduate Program in Photonics & Nanoelectronics

Crete 2020

Table of Contents

Abstract

Much of the knowledge that we have from our world stems from images. Using optics and cameras, we can map how much light a sample absorbs or refracts and from that deduce the composition or physical structure of the sample. On the other hand, a limiting factor in optical microscopy is the sensitivity to minute refractive index changes. For example, when imaging biological cells, labeling has to be used since the minute changes in the real and imaginary part of the refractive index, induced by the cell's inner workings, are practically invisible. Label-free imaging of the constituents of a living cell is still an open challenge

In this master thesis we explored novel techniques that involve the use of optical cavities towards a goal to enhance the resolution of optical microscopy. Our study was focused on using theoretical tools and numerical simulations to analyze the behavior of optical cavities when used in combination with imaging systems. Based on our analysis we have designed such complex optical systems, optimized to be used for imaging applications.

Περίληψη

Πολλές από τις γνώσεις που έχουμε για τον κόσμο μας, πηγάζουν από εικόνες. Χρησιμοποιώντας οπτικά στοιχεία και κάμερες, μπορούμε να χαρτογραφήσουμε πόσο φως απορροφάται ή διαθλάται από ένα δείγμα και από αυτό να συμπεράνουμε την σύσταση ή την φυσική δομή του δείγματος. Αφετέρου, ένας περιοριστικός παράγοντας στην οπτική μικροσκοπία είναι η ευαισθησία σε μικρές αλλαγές του δείκτη διάθλασης. Για παράδειγμα, όταν απεικονίζουμε βιολογικά κύτταρα, πρέπει να γίνεται χρήση ετικετών, καθώς οι παραμικρές αλλαγές στο πραγματικό και το φανταστικό μέρος του δείκτη διάθλασης, το οποίο οφείλεται στις εσωτερικές διεργασίες του κυττάρου, είναι πρακτικά αόρατες. Η μη χρήση ετικετών στην οπτική απεικόνιση ενός ζωντανού κυττάρου, είναι ακόμα μία ανοικτή πρόκληση.

Ο σκοπός της παρούσας μεταπτυχιακής εργασίας είναι να εξερευνήσουμε καινοτόμες τεχνικές, βασιζόμενες σε χρήση οπτικών κοιλοτήτων, με σκοπό την βελτίωση της διακριτικής ικανότητας στην οπτική μικροσκοπία. Η μελέτη μας εστιάστηκε στην χρήση θεωρητικών εργαλείων και αριθμητικών προσομοιώσεων ώστε να αναλύσουμε την συμπεριφορά των οπτικών κοιλοτήτων όταν αυτές συνδυάζονται με συστήματα οπτικής απεικόνισης. Σύμφωνα με την ανάλυσή μας, έχουμε σχεδιάσει σύνθετα οπτικά συστήματα, βελτιστοποιημένα ώστε να χρησιμοποιηθούν για εφαρμογές απεικόνισης.

Acknowledgements

I would like to thank my supervisor Prof. Dimitris G. Papazoglou and Dr. Von Klitzing Wolf for our collaboration on this project. Also, I would like to thank Prof. Peter Rakitzis for accepting to be a committee member for my Master thesis.

It is hard to express my gratitude for my collaboration with Debapriya Pal, a currently PhD student in Netherlands, on this project. I made a new friend and wish him all the best for his current research!

Moreover, I could not forget the rest of the BEC laboratory team: Dr. Bolpasi Vasiliki, Dr. Vasilakis Giorgos, PhD Drougakis Giannis, MSc Tzardis Vangelis and PhD Pareek Vinay. Thank you all very much for the good times and the help you offered!

Finally, I would like to thank my family, especially my mother Vougia Despoina, for all the sacrifices they have made to support me through all my studies and special thanks to my best friends Andronikos Chatzis and Despoina Mentzaki for advising and supporting me when I was in need for.

Introduction

Humans, curious beings, have always been trying to explain physical phenomena by making observations. This led to the development of physical sciences where we -people- try to explore and understand our world in both a macroscopic and microscopic level. Human eye, is an embedded imaging system that helps us image the world around. But eyes have a limit on the range they function. For this reason, scientists have developed techniques that allow to image objects in both macroscopic and microscopic scale.

Optical microscopy is an imaging technique where light interacts with some specimen (for example a biological cell) and by collecting the light after the interaction, an image of the specimen can be formed. The simplest and most well-known microscopy imaging technique is the bright field microscopy [1] where we illuminate a sample with white light from below and we observe it from above, like in light microscopes. The sample appears dark in a bright background. Another one, is the dark field microscopy [2] which forms images in an opposite way to the brightfield microscopy. The specimen is illuminated with white light but only scattered light is collected in the end, forming a bright image of the sample in a dark background. Finally, one frequently used technique is the fluorescent microscopy [3] where the sample gets excited with a particular wavelength and then sample reemits in a different wavelength which we collect to form the image.

As stated in the abstract, we want to explore a new optical imaging technique that involves optical cavities. As a result, the first two chapters are devoted to the theoretical background needed for optical cavities, while the third chapter contains theoretical simulations on the imaging system we designed. Finally, in the last chapter, we present some first experimental results on the operation an optical cavity experimentally.

Chapter 1 – Light Propagation in Optical Systems

1.1 Geometrical Optics and Paraxial Approximation

Geometrical optics, is a field of optics, where under the condition that the wavelength $\lambda \to 0$, the propagation of an electromagnetic light wave can be described with geometric light rays. These rays are related to the flow of energy in the electromagnetic field. They are straight lines in the case of homogeneous medium while they are curved in the case of inhomogeneous medium.

Paraxial approximation, takes into account that the rays form a small angle to the optical axis of the system or else that the propagation direction of the light deviates only slightly from some optical axis. This approximation allows great simplifications in calculations for some optical system. It is used both in ray tracing and in Gaussian optics, as light passes through a simple optical system (e.g. refractive plane) or a complex one (e.g. combined optical elements like lenses and mirrors).

By defining the angle of the ray to the optical axis with the letter β and considering paraxial approximation, the following Taylor expansion simplifications emerge:

$$cos\beta \cong 1 \quad , \quad sin\beta \cong \beta \quad , \quad tan\beta \cong \beta \tag{1}$$

with β measured in radians.

1.1.1 Ray Matrix Representation in Paraxial Approximation

Ray transfer matrix analysis is a mathematical method that uses matrices to describe ray propagation through an optical system, under the paraxial approximation. It connects the height and inclination of the ray in the input plane to those in the output plane, as the ray progresses through an optical system. Height is defined on a transverse plane to the optical axis and inclination is measured from the optical axis to the ray.
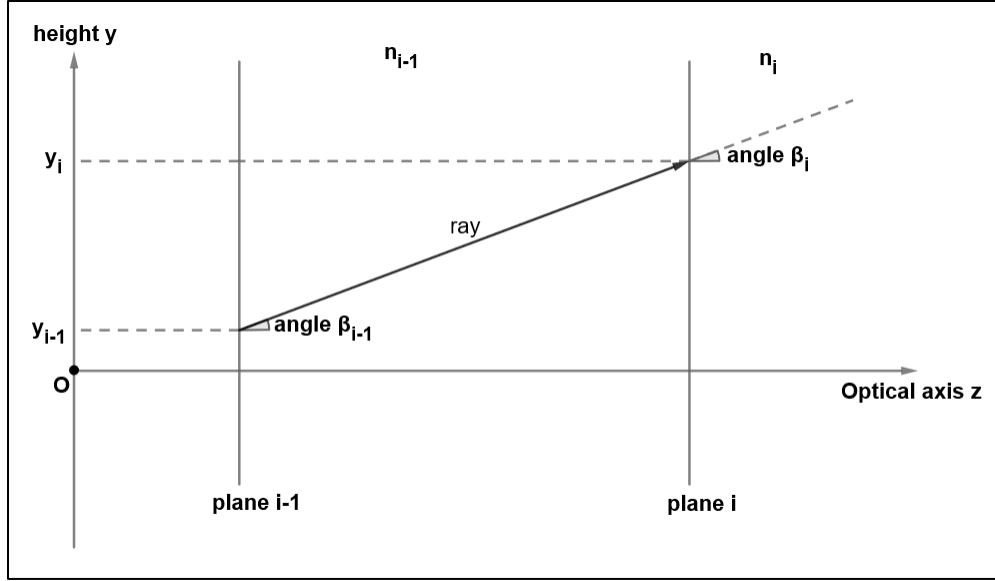
Fig. 1 *Representation of a ray propagation on the y-z plane*

Both are described as a column vector, namely ray vector. Therefore, the form of the ray vector will be:

$$\begin{bmatrix} y_i \\ n_i \cdot \beta_i \end{bmatrix} \tag{2}$$

where, y_i is the height of the ray, β_i the inclination (angle) of the ray measured from optical axis z in radians and n_i is the index of refraction of the medium

As ray propagates through an optical system, the ray vectors of the initial transverse plane to the final transverse plane are connected through a 2×2 transformation matrix which describes the optical system between these transverse planes.

$$\begin{bmatrix} y_i \\ n_i \cdot \beta_i \end{bmatrix} = \begin{bmatrix} A & B \\ C & D \end{bmatrix} \cdot \begin{bmatrix} y_{i-1} \\ n_{i-1} \cdot \beta_{i-1} \end{bmatrix} \tag{3}$$

This transformation matrix is often referred to as ABCD matrix and the whole approach as ABCD matrix theory which will be analyzed later.

1.2 Validity Limits of the Paraxial Approximation

In natural sciences, the approximations of Eq.(1) are widely used to simplify calculations in many problems. However, those terms are only the first non-zero terms in Taylor expansion approximation. This means, that they give good accuracy for small angles while more terms of the expansion are needed to improve accuracy for bigger angles. As a result, it is necessary to study the range of angles that the approximation of Eq.(1) works adequately.
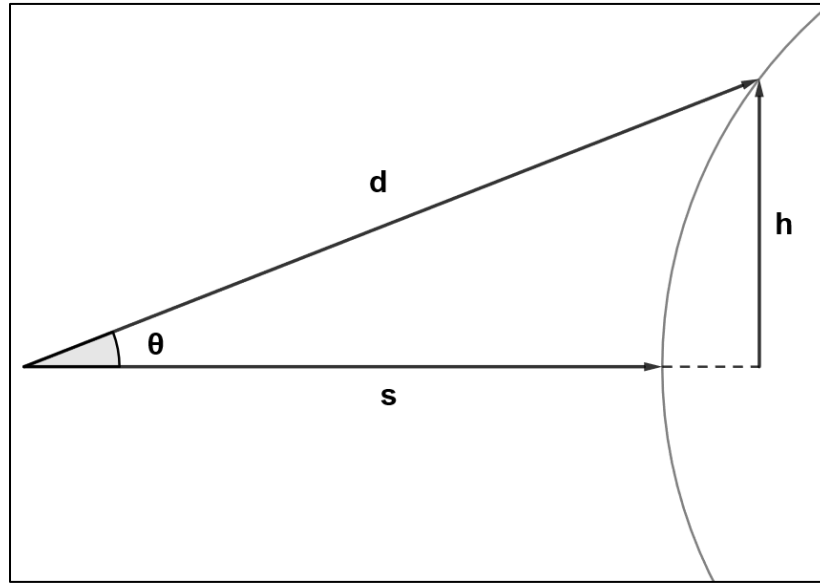

Fig. 2 *Ray d inclined by angle θ to the optical axis, incident to a spherical surface.*

In the image above, one can see that for increasing inclination θ, the approximation produces increasing errors (dashed line). [4]

Applying Pythagoras's theorem,

$$\frac{d}{s} \cong \sqrt{1 + \left(\frac{h}{s}\right)^2} \tag{4}$$

But $d \cong s$ for every $\frac{d}{s} \leq 1.1$, and as a result,

$$\frac{h}{s} \leq 0.458 \implies \theta \leq 24.6° \tag{5}$$

Assuming m is an error term (obviously $m < 1$),

$$\frac{d}{s} \leq 1 + m \tag{6}$$

it can be concluded that,

$$\frac{h}{s} \leq \sqrt{2m + m^2} \tag{7}$$

However, for $m \ll 1$ (e.g. 0.1) the term $2m$ is much larger than m^2 and therefore,

$$\frac{h}{s} \leq \sqrt{2m} \tag{8}$$

In Fig. 2, numerical aperture NA is defined as the following product:

$$NA = n \, sin\theta \tag{9}$$

Where n is the refractive index of the medium in object space and θ is the maximum half-angle of the cone of rays that the optical system collects from the object.

However, in paraxial approximation $sin\theta \approx tan\theta$ and Eq.(9) turns to $NA \approx n \, tan\theta$. As a result, for $n = 1$ in object space,

$$NA = h/s \tag{10}$$

In the following table, one can see what is the maximum error for different values of the inclination.

θ	m	NA
2.5⁰	0.09%	0.04
8⁰	0.99%	0.14
17⁰	4.67%	0.29
24⁰	9.91%	0.41
30⁰	16.67%	0.50
35⁰	24.51%	0.57
40⁰	35.20%	0.64
45⁰	50%	0.71

Table 1 *Error term m for different angles θ and Numerical Aperture NA.*

From the table above, it is obvious that the approximation performs poorly as the angle increases and the rate of change for the error is not stable but also increases with increasing angle. As far as the error stays under 16.67% for angles less than 30° it is safe to say that for that range of angles, paraxial approximation gives a decent accuracy.

1.3 ABCD Matrix Theory

ABCD matrix theory connects the input parameters[5] (height and inclination) of a ray in the paraxial approximation, to the output parameters of the same ray as it travels through an optical system:

$$\begin{bmatrix} y_i \\ n_i \cdot \beta_i \end{bmatrix} = \begin{bmatrix} A & B \\ C & D \end{bmatrix} \cdot \begin{bmatrix} y_{i-1} \\ n_{i-1} \cdot \beta_{i-1} \end{bmatrix} \tag{11}$$

or

$$\begin{bmatrix} y_i \\ n_i \cdot \beta_i \end{bmatrix} = M \cdot \begin{bmatrix} y_{i-1} \\ n_{i-1} \cdot \beta_{i-1} \end{bmatrix} \tag{12}$$

The above ABCD matrix M describes the optical system and traces the light's path. When light propagates through an optical system, three basic transformations can occur with optical surfaces. Light can just displace itself through a surface and can be refracted or reflected by system's optical surfaces.

For some complex optical system in which all the above transformations can occur, one can find the total matrix that describes this system, simply by multiplying the individual basic interaction matrices (the next one times the previous one):

$$\begin{bmatrix} y_i \\ n_i \cdot \beta_i \end{bmatrix} = M_i \cdot M_{i-1} \cdot \ldots \cdot M_1 \cdot \begin{bmatrix} y_1 \\ n_1 \cdot \beta_1 \end{bmatrix} \tag{13}$$

Subsequently, the three basic transformation matrices will be derived assuming that paraxial approximation applies.

For the following derivations, will be consider the following definition: refractive index n of the medium, will be positive when ray displaces to the positive of the optical axis and negative when displaces to the negative of the optical axis.
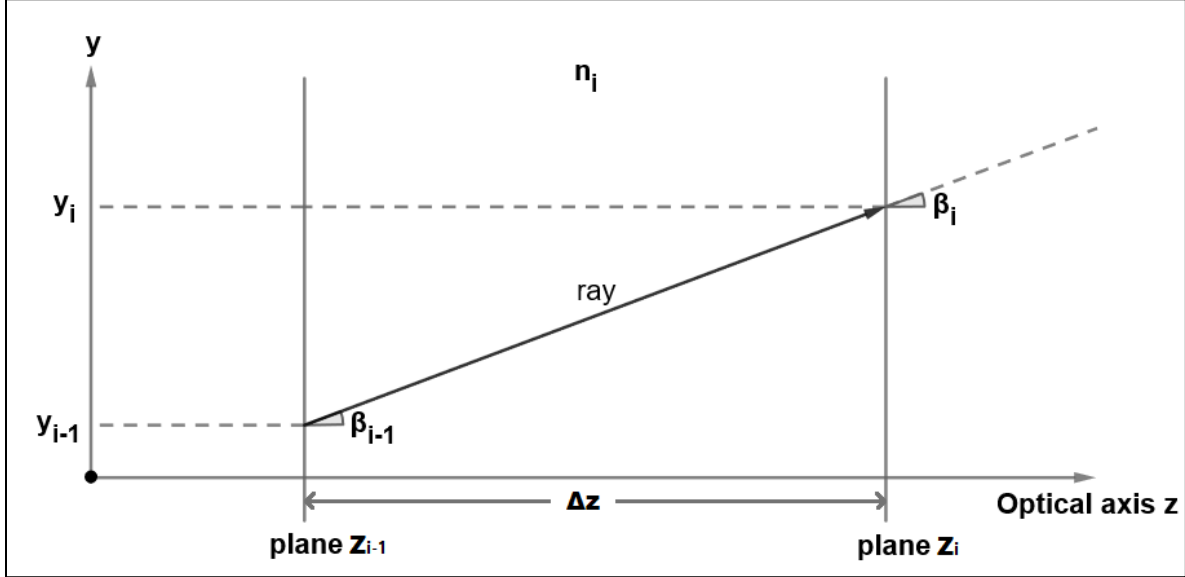
1.3.1 Optical Displacement Transformation Matrix

Fig. 3 Optical displacement.

Taking into account Eq.(1), the following can be derived:

$$y_i \approx y_{i-1} + \Delta z \cdot \beta_{i-1}$$
$$\beta_i = \beta_{i-1} \tag{14}$$

where dz is the algebraic value of the displacement of the ray on z axis.

Assuming that during the displacement there is no change in the index of refraction n_i of the medium, one can get:

$$y_i \approx y_{i-1} + \frac{\Delta z}{n_i} n_i \cdot \beta_{i-1}$$
$$n_i \beta_i = n_i \beta_{i-1} \tag{15}$$

The above equations can be written in matrix representation as follows:

$$\begin{bmatrix} y_i \\ n_i \cdot \beta_i \end{bmatrix} = \begin{bmatrix} 1 & \frac{\Delta z}{n_i} \\ 0 & 1 \end{bmatrix} \cdot \begin{bmatrix} y_{i-1} \\ n_i \cdot \beta_{i-1} \end{bmatrix} \tag{16}$$

which concludes that the matrix for the displacement of a ray is defined as:

$$M = \begin{bmatrix} 1 & D \\ 0 & 1 \end{bmatrix} = \begin{bmatrix} 1 & \frac{\Delta z}{n} \\ 0 & 1 \end{bmatrix} \tag{17}$$

The same result occurs when the ray is displaced to the -z of the optical axis because then $\Delta z < 0$ and $n < 0$ (by definition).
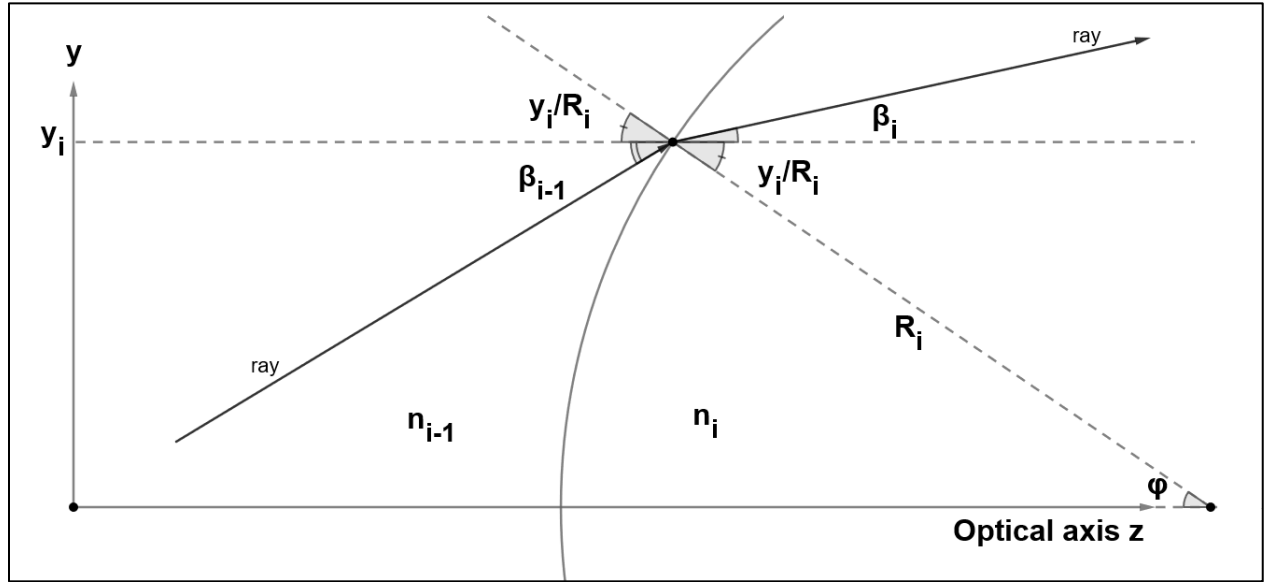
1.3.2 Optical Refraction Transformation Matrix

Fig. 4 Optical refraction from spherical surface of radius R_i.

The height of the ray on the spherical interface remains the same, meaning $y_i = y_{i-1}$.

Taking into account Eq.(1) , the following can be derived:

$$\varphi \approx y_i/R_i \tag{18}$$

while from Fig. 4 the next two relations can be acquired:

$$\theta_i = \beta_i + \varphi \text{ and } \theta_{i-1} = \beta_{i-1} + \varphi \tag{19}$$

From Eq.(1) and Snell's Law, one can get:

$$n_{i-1}\theta_{i-1} = n_i\theta_i \tag{20}$$

Combining all the above equations, the result written in matrix representation is the following:

$$\begin{bmatrix} y_i \\ n_i \cdot \beta_i \end{bmatrix} = \begin{bmatrix} 1 & 0 \\ -\dfrac{(n_i - n_{i-1})}{R_i} & 1 \end{bmatrix} \cdot \begin{bmatrix} y_{i-1} \\ n_{i-1} \cdot \beta_{i-1} \end{bmatrix} \tag{21}$$

which concludes that the matrix describing the refraction of light, in paraxial approximation, from spherical surfaces is defined as:

$$M = \begin{bmatrix} 1 & 0 \\ -P & 1 \end{bmatrix} = \begin{bmatrix} 1 & 0 \\ -\dfrac{(n_i - n_{i-1})}{R_i} & 1 \end{bmatrix} \tag{22}$$

where $P = (n_i - n_{i-1})/R_i$ is defined as the optical power of the refractive surface and R_i can be either negative or positive for concave or convex refractive surface respectively.
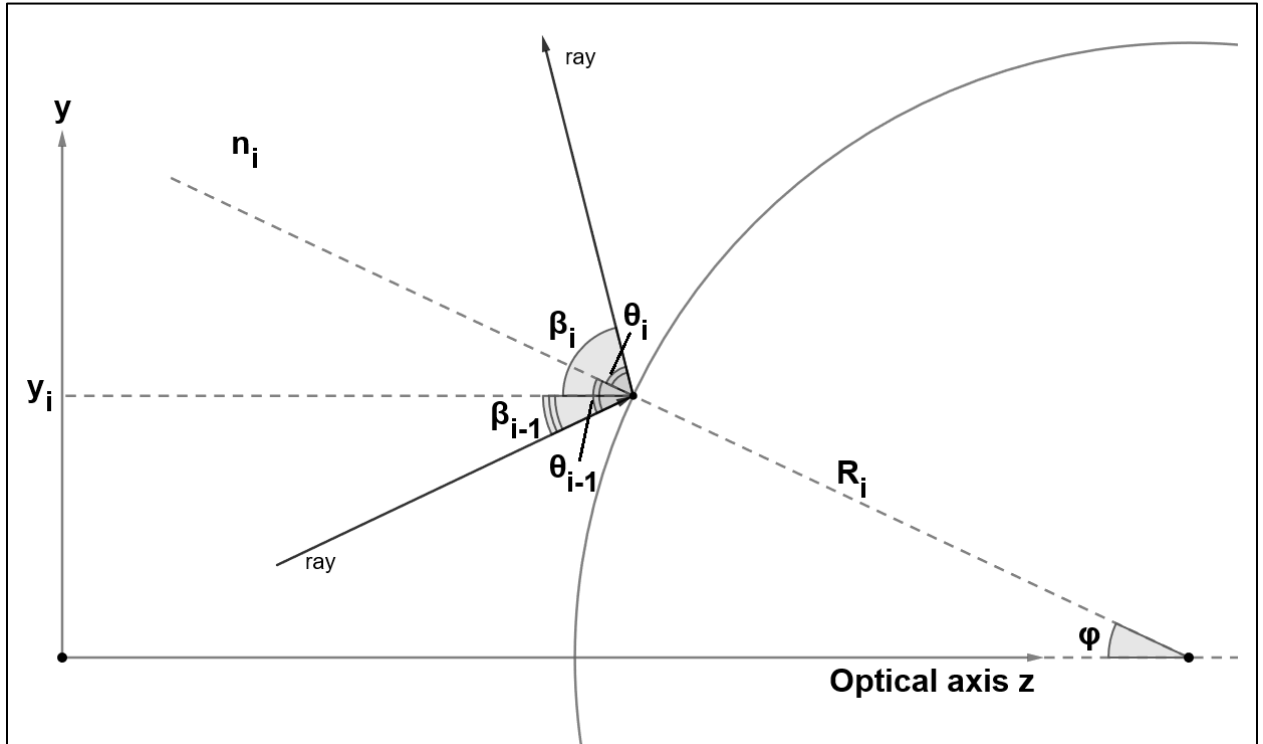
1.3.3 Optical Reflection Transformation Matrix

Fig. 5 *Optical reflection from spherical surface of radius R_i.*

The height of the ray slightly before and slightly after the reflection, remains the same, meaning $y_i = y_{i-1}$.

Taking into account Eq.(1), the following can be derived:

$$\varphi \approx y_i/R_i \tag{23}$$

while from Fig. 5 the next two relations can be acquired:

$$\beta_{i-1} = \theta_{i-1} - \varphi \text{ and } \beta_i = \theta_i + \varphi \tag{24}$$

and by subtracting the two equations of Eq.(24), considering that $\theta_{i-1} = \theta_i$, one gets:

$$\beta_i = 2\varphi + \beta_{i-1} \tag{25}$$

and while ray remains in the same medium due to reflection, there is no change in the refractive index, $n_i = n_{i-1}$. Eq.(25) can be written as:

$$\beta_i n_i = 2\varphi n_i + \beta_{i-1} n_i \tag{26}$$

Combining all the above, the result written in matrix representation is the following:

$$\begin{bmatrix} y_i \\ n_i \cdot \beta_i \end{bmatrix} = \begin{bmatrix} 1 & 0 \\ \dfrac{2n_i}{R_i} & 1 \end{bmatrix} \cdot \begin{bmatrix} y_{i-1} \\ n_i \cdot \beta_{i-1} \end{bmatrix} \tag{27}$$

indicating that the matrix describing the reflection of light, in paraxial approximation, from spherical surfaces is defined as:

$$M = \begin{bmatrix} 1 & 0 \\ -P & 1 \end{bmatrix} = \begin{bmatrix} 1 & 0 \\ \dfrac{2n_i}{R_i} & 1 \end{bmatrix} \tag{28}$$

where $P = -2n_i/R_i$ again, is defined as the optical power of the reflecting surface and R_i can be either negative or positive for concave or convex refractive surface respectively.

One can conclude to the same result by using refraction transformation matrix of Eq.(22). Considering negative and positive refractive indices, as defined earlier, and that the ray stays at the same medium (meaning that refractive index does not change):

$$M = \begin{bmatrix} 1 & 0 \\ -\dfrac{(n_i - n_{i-1})}{R_i} & 1 \end{bmatrix} = \begin{bmatrix} 1 & 0 \\ -\dfrac{(-n_i - n_i)}{R_i} & 1 \end{bmatrix} = \begin{bmatrix} 1 & 0 \\ \dfrac{2n_i}{R_i} & 1 \end{bmatrix} \tag{29}$$

When the ray is moving to the negative of the optical axis and gets reflected, the reflection matrix is not the same as Eq.(28). Using again refraction transformation matrix of Eq.(22) and considering negative and positive refractive indices, as defined earlier, and that the ray stays at the same medium:

$$M = \begin{bmatrix} 1 & 0 \\ -\dfrac{(n_i - n_{i-1})}{R_i} & 1 \end{bmatrix} = \begin{bmatrix} 1 & 0 \\ -\dfrac{n_i - (-n_i)}{R_i} & 1 \end{bmatrix} = \begin{bmatrix} 1 & 0 \\ -\dfrac{2n_i}{R_i} & 1 \end{bmatrix} \tag{30}$$

Where now $P = 2n_i/R_i$ is the optical power.

1.3.4 Sign conversions in Bibliography

Unfortunately, the sign of a radius of curvature of a convex and a concave spherical surface is not defined in a coherent way in the bibliography [5] [6] [7] [8] . This causes a lot of confusion especially when analyzing the behavior of optical cavities, where light repeatedly bounces back and forth. This discrepancy in the bibliography makes it very difficult to extract information from different sources.

A solution is to use the optical power to describe the subcomponents of an optical system. All bibliography is in coherence here, since a converging optical system is described by positive optical power, while a diverging optical system by negative optical power. The direction of propagation does not affect this property so this is very simple to be implemented in the case of an optical cavity.

In more detail, for reflection matrices, when the surface of incidence is concave, light converges and optical power P is always positive, while in the case of convex, light diverges and optical power P is always negative.

The table that follows makes clear that no matter what description one uses, optical power depends only on the surface of incidence. Whether radius of curvature is positive or negative, depends only on the optical power, as defined in the present text.
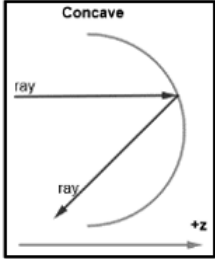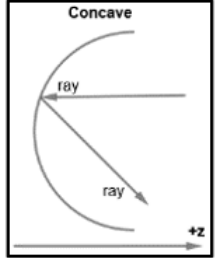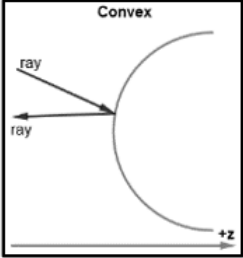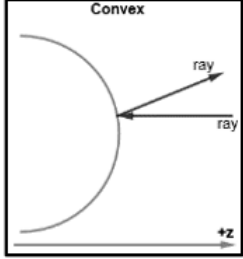
Type of Surface & displacement	Optical Power P	Radius of Curvature R_i
	$P > 0$ $$P = -\frac{2n_i}{R_i}$$	$R_i < 0$
	$P > 0$ $$P = \frac{2n_i}{R_i}$$	$R_i > 0$
	$P < 0$ $$P = -\frac{2n_i}{R_i}$$	$R_i > 0$
	$P < 0$ $$P = \frac{2n_i}{R_i}$$	$R_i < 0$

Table 2 Optical power depends on the surface of incidence and radius of curvature on the optical power.

1.3.5 Properties of ABCD Matrices

It is necessary to point out some properties of the ABCD matrices defined above. For square matrices of equal size, the following property applies:

$$det(M_1 \cdot M_2 \cdot ... \cdot M_i) = det(M_1) \cdot det(M_2) \cdot ... \cdot det\ (M_i) \tag{31}$$

For random optical system, the final ABCD matrix M that describes it, will derive from several multiplications of displacement, refraction and/or reflection matrices.

It is obvious that all determinants of the matrices that were derived is equal to 1 and as a result of Eq.(31), every ABCD matrix M that describes a random optical system, in paraxial approximation, will have the following property:

$$\boldsymbol{det(M) = 1} \tag{32}$$

This is a very useful relation, which allows to check the validity of a resultant matrix which describes some optical system.

Chapter 2 – Optical Cavities

An optical cavity (or optical resonator) is comprised of two mirrors (curved or not) with high reflectivity, placed one opposite to the other. As a result, when light enters the cavity, is being reflected back and forth due to multiple reflections on both mirrors and light performs some kind of oscillation inside it.
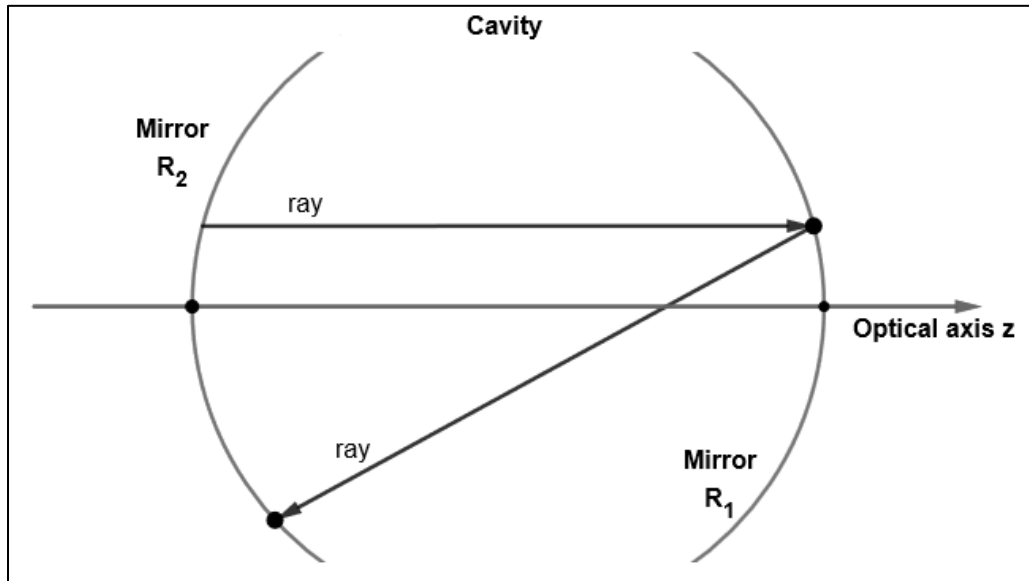

Fig. 6 *An optical cavity.*

2.1 Stability Condition for Optical Cavities

Stable cavities are defined as those that allow light to remain inside them after multiple reflections, while unstable cavities make light diverge and leave the cavity after multiple reflections.

In geometrical optics, when the ray starts from one mirror and reaches back to the same mirror again, one roundtrip has been performed. In order to treat stability, unit cell is defined as the total matrix that represents one roundtrip inside the cavity.

The general case will be considered here, meaning that mirrors will be of the same type (either both concave or both convex) or of different types (concave and convex). This means that radii of curvature that will be used, have undetermined sign in order for the general case to be covered.

In the next images, all possible types of cavities are depicted and the ray moving from mirror 2 and back again has completed one roundtrip.
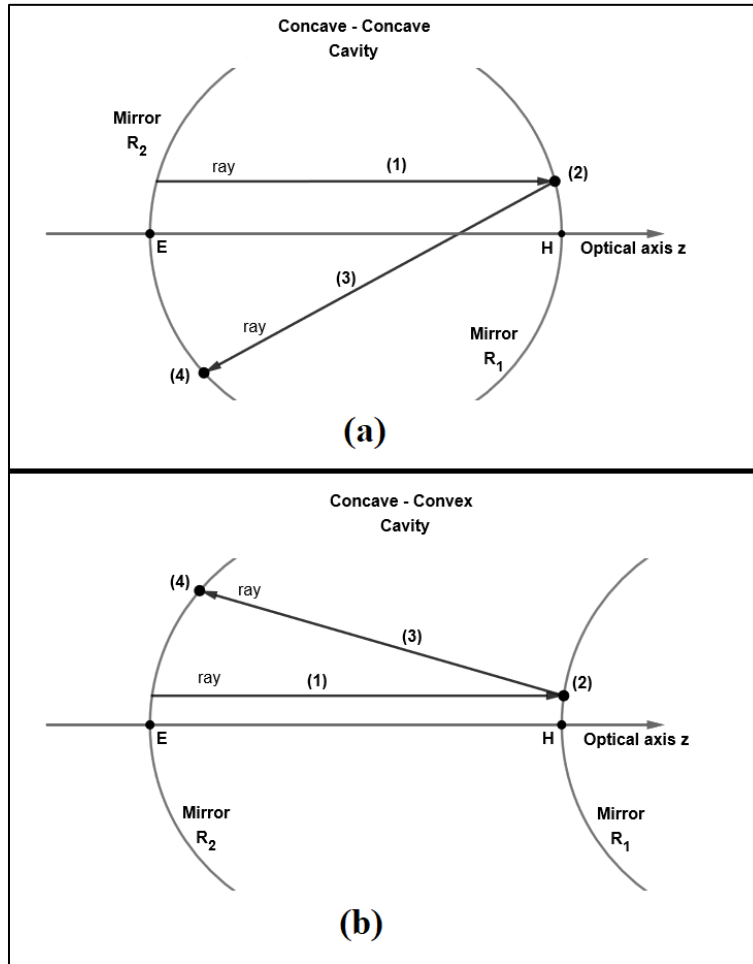

Fig. 7 *Two different types of cavities, (a) concave-concave and (b) concave-convex.*
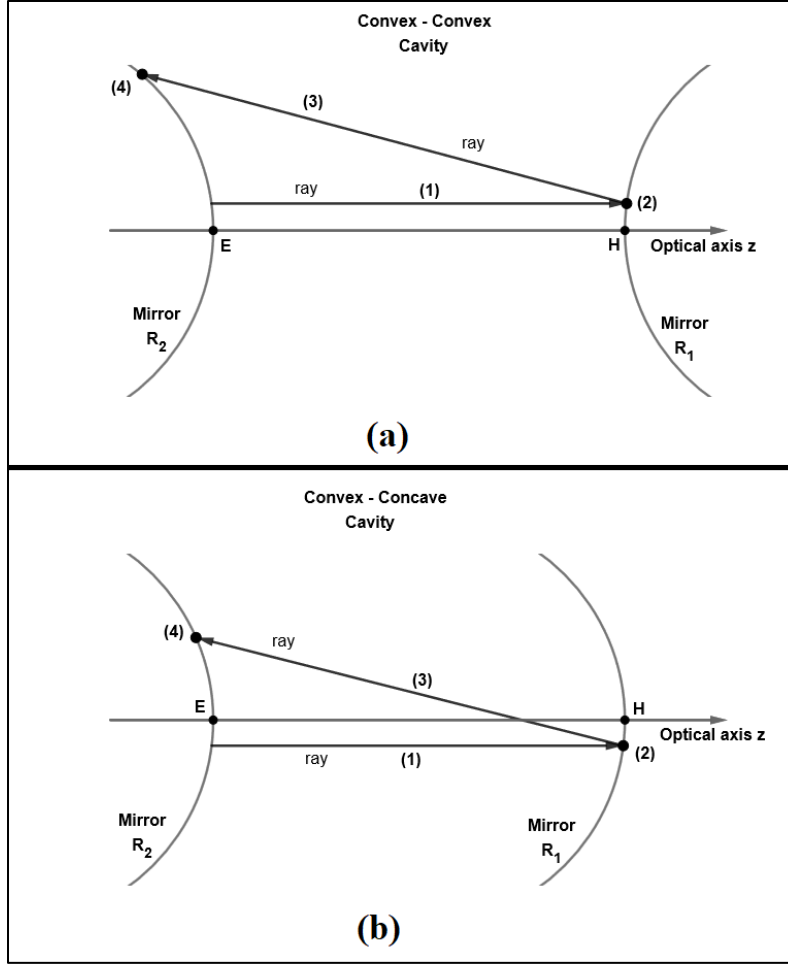
Fig. 8 *Two different types of cavities, (a) convex-convex and (b) convex-concave.*

In all the cases above, the ray is confined inside an optical cavity of length $L \equiv EH > 0$, propagating in air - index of refraction $n = 1$. It starts from mirror 2 on the left following path (1) and gets reflected from mirror 1, which has radius of curvature R_1 (algebraic value). Then follows path (3) until it reaches back to mirror 2 again, which has radius of curvature R_2 (algebraic value) and get reflected. The total path of the ray that was described, constitutes one roundtrip (or else one unit cell) for the ray.

To find the total matrix that describes one roundtrip for the ray, the total path is broken to one displacement matrix for path 1, followed by a reflection matrix for mirror 1, again a displacement matrix for path 2, ending with a reflection matrix for mirror 2. The ABCD matrix representation follows:

24

$$M = \begin{bmatrix} 1 & 0 \\ -\dfrac{2}{R_2} & 1 \end{bmatrix} \cdot \begin{bmatrix} 1 & L \\ 0 & 1 \end{bmatrix} \cdot \begin{bmatrix} 1 & 0 \\ \dfrac{2}{R_1} & 1 \end{bmatrix} \cdot \begin{bmatrix} 1 & L \\ 0 & 1 \end{bmatrix} \tag{33}$$

and by simplifying the total matrix, the result is:

$$M = \begin{bmatrix} \dfrac{R_1 + 2L}{R_1} & \dfrac{2LR_1 + 2L^2}{R_1} \\ \dfrac{2R_2 - 2R_1 - 4L}{R_1 R_2} & \dfrac{(R_1 + 2L)R_2 - 4LR_1 - 4L^2}{R_1 R_2} \end{bmatrix} = \begin{bmatrix} A & B \\ C & D \end{bmatrix} \tag{34}$$

What follows, are the equations for 2 consecutive unit cells (index of refraction $n = 1$):

$$\begin{bmatrix} y_{m+1} \\ \beta_{m+1} \end{bmatrix} = \begin{bmatrix} A & B \\ C & D \end{bmatrix} \cdot \begin{bmatrix} y_m \\ \beta_m \end{bmatrix} \tag{35}$$

$$\begin{bmatrix} y_{m+2} \\ \beta_{m+2} \end{bmatrix} = \begin{bmatrix} A & B \\ C & D \end{bmatrix} \cdot \begin{bmatrix} y_{m+1} \\ \beta_{m+1} \end{bmatrix} \tag{36}$$

with $m = 0, 1, 2, \dots$.

Starting from Eq.(35),

$$\begin{cases} y_{m+1} = Ay_m + B\beta_m \\ \beta_{m+1} = Cy_m + D\beta_m \end{cases} \Rightarrow \begin{cases} y_{m+1} - Ay_m = B\beta_m \\ \beta_{m+1} - Cy_m = D\beta_m \end{cases} \tag{37}$$

and dividing both equations to eliminate β_m ,

$$\frac{y_{m+1} - Ay_m}{\beta_{m+1} - Cy_m} = \frac{B}{D} \tag{38}$$

the result is:

$$B\beta_{m+1} - BCy_m = D(y_{m+1} - Ay_m) \tag{39}$$

The Ay_{m+1} term is added on both sides for later use,

$$Ay_{m+1} + B\beta_{m+1} - BCy_m = Ay_{m+1} + D(y_{m+1} - Ay_m) \tag{40}$$

The equation above is a sequence that involves both the ray height and the inclination. Proceeding with Eq.(36), only the first equation that arises is needed in order to eliminate inclination from the sequence,

$$y_{m+2} = Ay_{m+1} + B\beta_{m+1} \tag{41}$$

Substitute Eq.(41) into Eq.(40) the result is:

$$y_{m+2} - (A + D)y_{m+1} + (AD - BC)y_m = 0 \tag{42}$$

But from Eq.(32), $(AD - BC) = det(M) = 1$, and Eq.(1.42) can be written as:

$$y_{m+2} - (A + D)y_{m+1} + y_m = 0 \tag{43}$$

The sequence of Eq.(43) is the discrete analogous of the harmonic oscillator differential equation[5]. As a result, exponential solutions are expected, that will either have real exponent and in this case the ray will deviate from the cavity, or imaginary one and the ray will oscillate inside the cavity. So, imaginary solutions must be imposed.

$$\underline{\text{Solution:}} \quad y_m = y_0 \cdot e^{i \cdot m \cdot \theta} \tag{44}$$

Imposing Eq.(42) into Eq.(41),

$$y_0 \cdot e^{i \cdot (m+2) \cdot \theta} - (A + D) \cdot y_0 \cdot e^{i \cdot (m+1) \cdot \theta} + y_0 \cdot e^{i \cdot m \cdot \theta} = 0 \tag{45}$$

and factorizing,

$$y_0 \cdot e^{i \cdot m \cdot \theta} \cdot \left(e^{i \cdot 2 \cdot \theta} - (A + D) \cdot e^{i \cdot \theta} + 1 \right) = 0 \tag{46}$$

the result is:

$$\left(e^{i \cdot \theta} \right)^2 - (A + D) \cdot e^{i \cdot \theta} + 1 = 0 \tag{47}$$

which is a quadratic equation with $e^{i \cdot \theta}$ as variable and the discriminant is,

$$\Delta = (A + D)^2 - 4 \tag{48}$$

Because $e^{i \cdot \theta} = cos\theta + i \cdot sin\theta$ is in general an imaginary number ($\epsilon\ \mathbb{C}$), the discriminant must be negative number ($\Delta < 0$) and the solutions are,

$$e^{\pm\, i \cdot \theta} = \frac{(A + D) \pm i \cdot \sqrt{4 - (A + D)^2}}{2} \tag{49}$$

or written in another form,

$$e^{\pm\, i \cdot \theta} = \frac{(A + D)}{2} \pm i \cdot \sqrt{1 - \left(\frac{A + D}{2} \right)^2} = cos\theta \pm i \cdot sin\theta \tag{50}$$

Consequently, from Eq.(42) and Eq.(48) the height of the ray inside the cavity, measured with respect to the optical axis is:

$$y_m = y_0 \cdot \left(\frac{(A + D)}{2} \pm i \cdot \sqrt{1 - \left(\frac{A + D}{2} \right)^2} \right)^m \tag{51}$$

or else,

$$y_m = y_0 \cdot (cos\theta \pm i \cdot sin\theta)^m \tag{52}$$

The real part of the solution in Eq.(48) is of interest which is equal to a cosine term, for which the well-known inequality $-1 \leq cos\theta \leq 1$ applies, resulting in:

$$-1 \leq \frac{A + D}{2} \leq 1 \tag{53}$$

or by adding 1 in all parts,

$$0 \leq \frac{A + D + 2}{4} \leq 1 \tag{54}$$

Using the values of A and D from Eq.(32), the result is:

$$0 \leq \frac{(R_1 + L)R_2 - LR_1 - L^2}{R_1 R_2} \leq 1 \tag{55}$$

and by factorizing,

$$0 \leq \left(1 + \frac{L}{R_1}\right) \cdot \left(1 - \frac{L}{R_2}\right) \leq 1 \tag{56}$$

Eq.(54) is the stability condition for random cavities and can be written as:

$$0 \leq g_1 \cdot g_2 \leq 1 \tag{57}$$

Where $g_1 = \left(1 + \frac{L}{R_1}\right)$, $g_2 = \left(1 - \frac{L}{R_2}\right)$, L = length of the cavity and R_i = radius of curvature of each mirror taking either positive or negative values depending on the occasion as described in Table 2.

2.1.1 Mapping for Stable Cavities

The following plot of Eq.(57) shows in which regions stable cavities exist , for different values of the parameters g_1 and g_2.
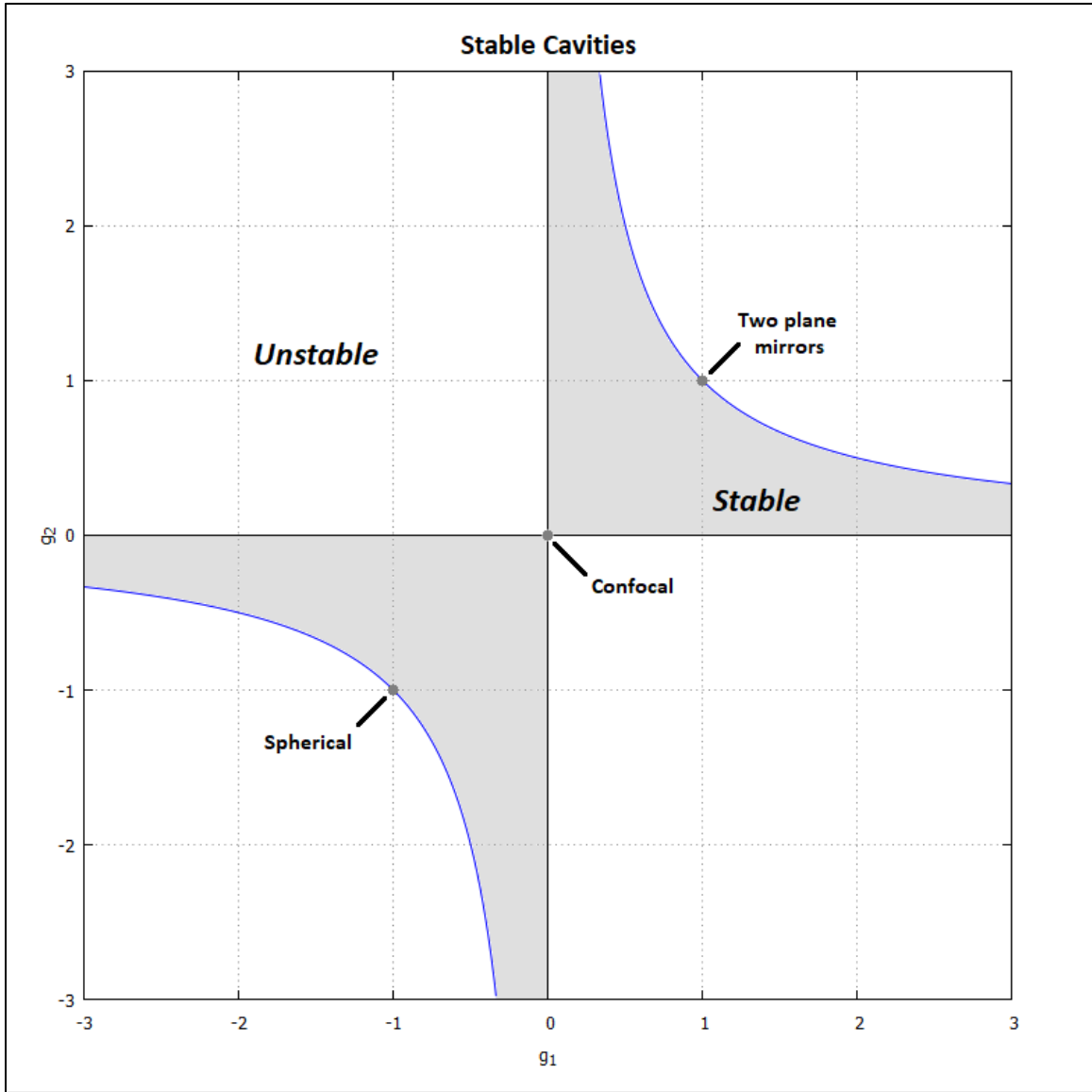

Fig. 9 *Mapping for stable cavities - g_2 versus g_1*

Moreover, is also useful to map stable cavities by using Eq.(56). The following plot shows the stable regions for different values of both radii of curvature as they are defined in Table 2.
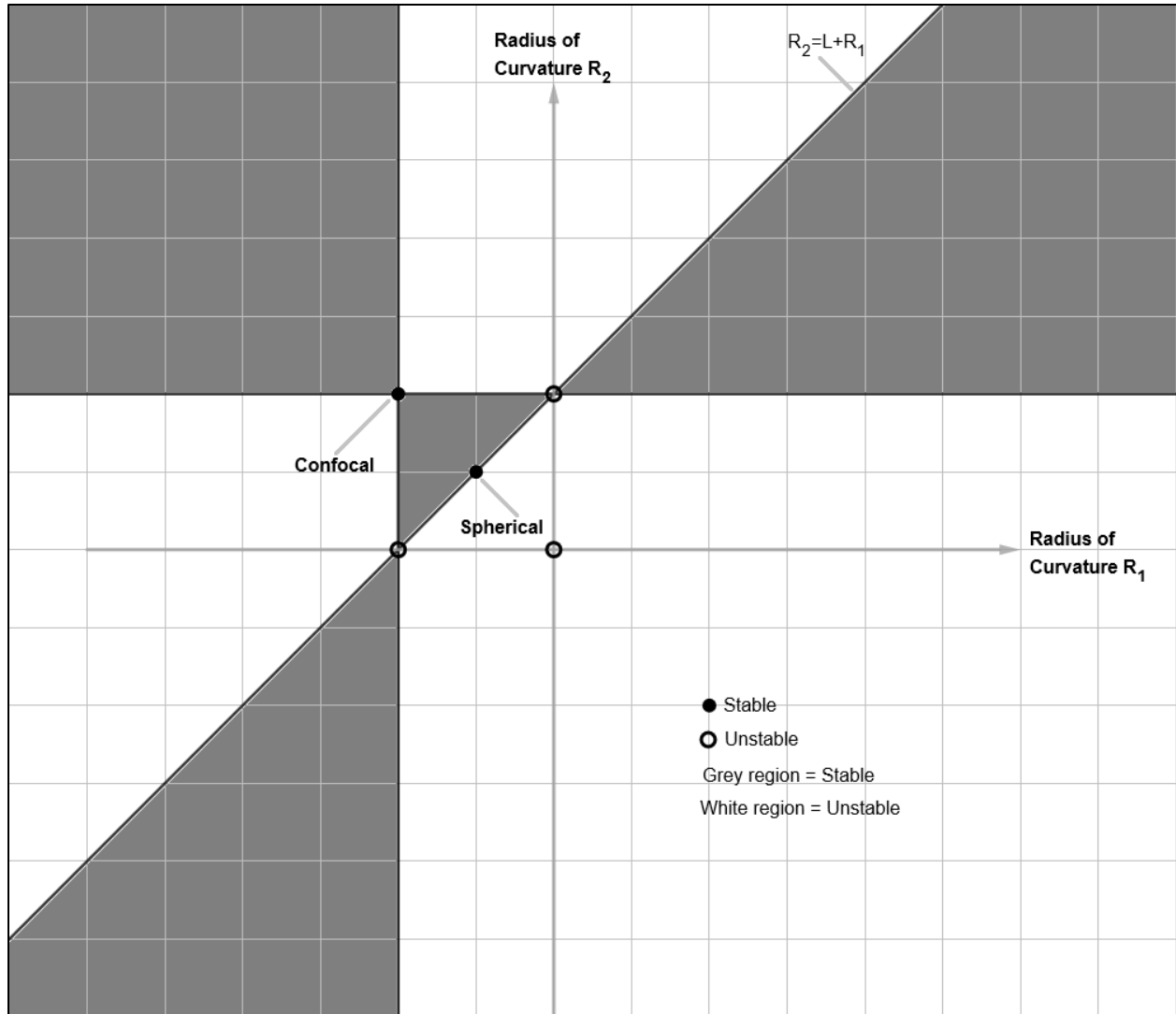
Fig. 10 *Mapping for stable cavities - R_2 versus R_1*

In the figures above, two types of stable cavities are pointed out, spherical cavity and confocal cavity with the later being a strong candidate to be tested experimentally (in the next chapter this will be more obvious). Furthermore, the two plane mirrors cavity is stated too, but is stable only under one extra condition, that the rays must always be parallel to the optical axis in order to remain inside the cavity.

The following figures depict the geometry of the pointed cavities.
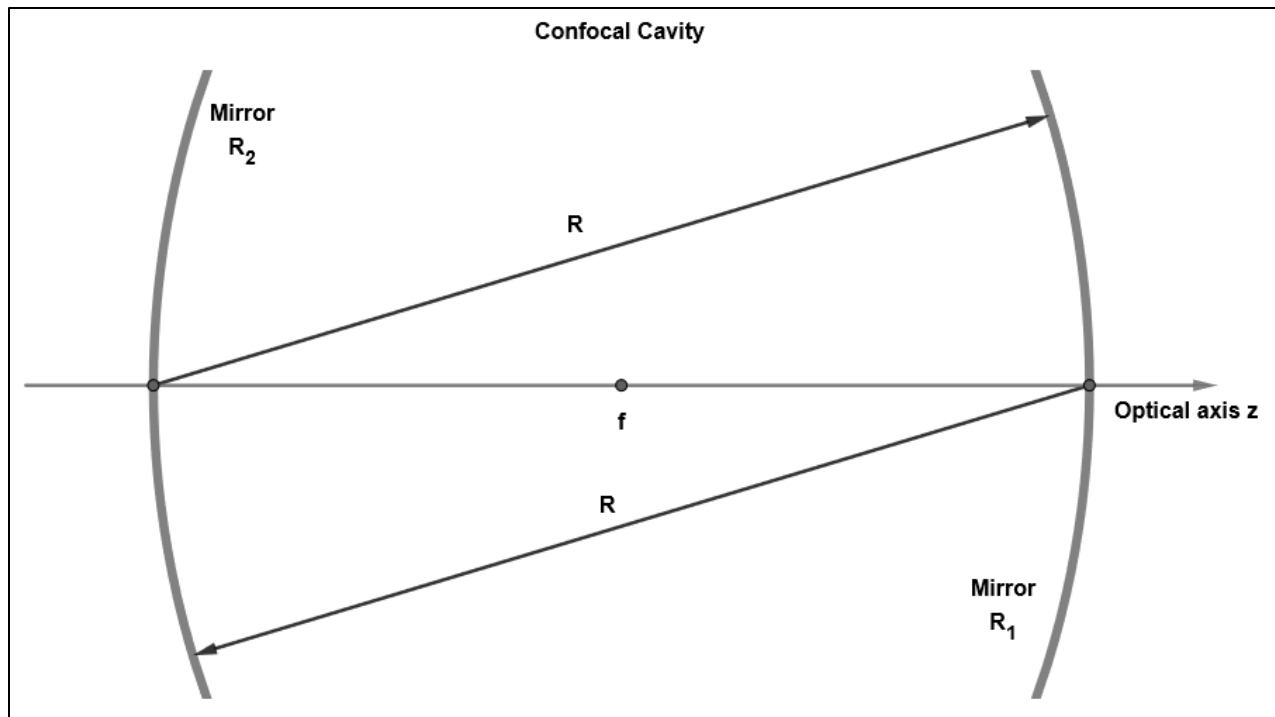
Fig. 11 *Geometry of confocal cavity.*
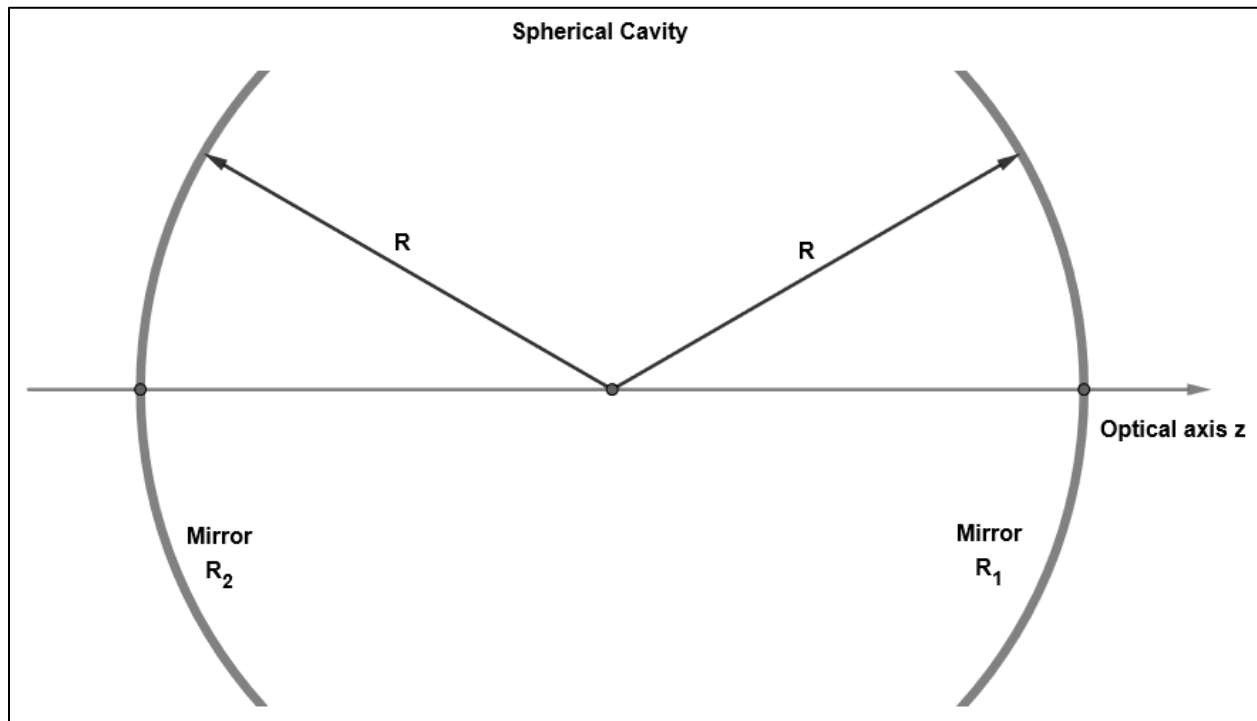
Fig. 12 *Geometry of spherical cavity.*

2.1.2 Geometrical Operation of Cavities

In this section, some numerical simulations [Ref: D. G. Papazoglou (2020)] will be presented in order to visualize how light rays oscillate or not inside a cavity. These numerical simulations were created in Maxima [9], a computer algebra system, which is a free computer software. The code that was developed to perform these numerical simulations uses ABCD matrix theory.

In the following examples, rays will enter different types of cavities (with R_1 being the radius of curvature of the right mirror, R_2 of the left mirror and L the cavity length), in different configurations (different initial height y_0 and different initial inclination β_0 both with respect to the optical axis).

Example 1

Confocal cavity with $|R_1| = |R_2| = L = 10 \ cm$. Rays enter the cavity at $y_0 = 1 \ cm$ without some initial inclination, $\beta_0 = 0$,
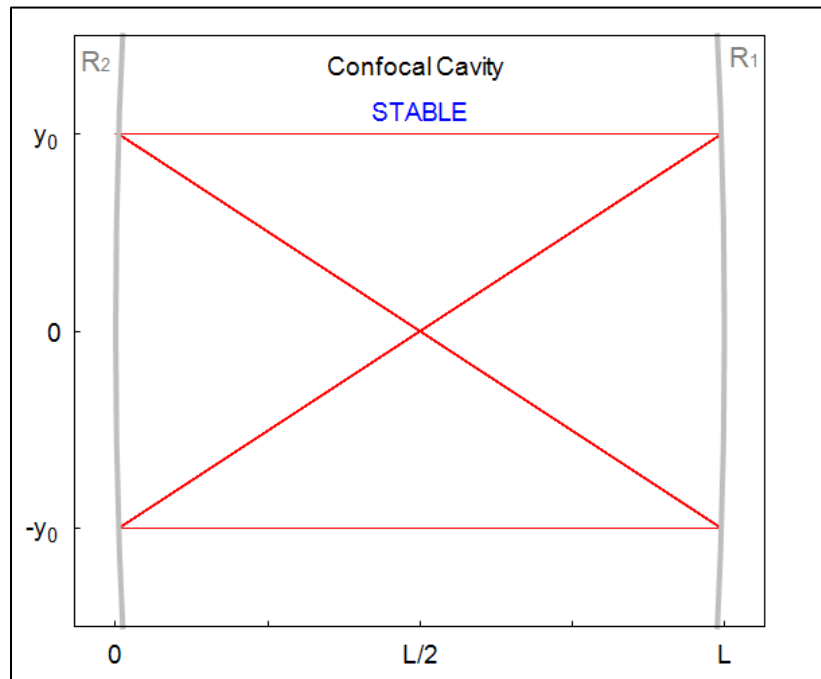

Fig. 13 *Path of the rays inside the cavity after 50 roundtrips.*
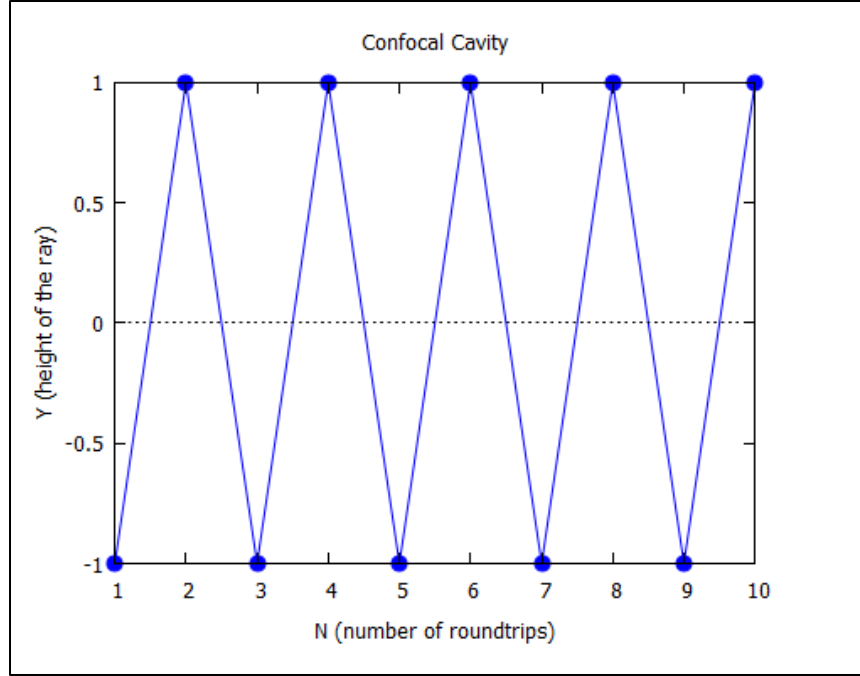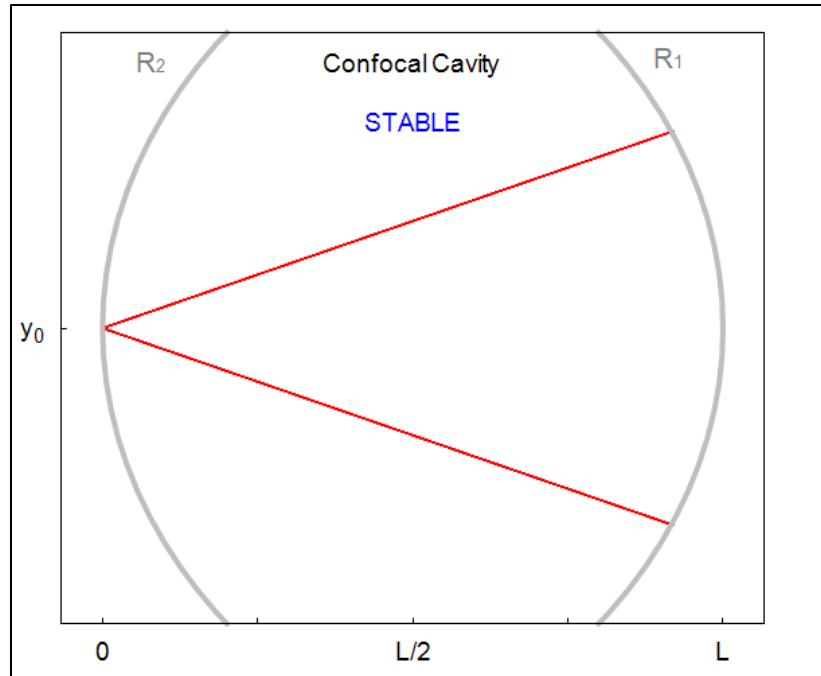
Fig. 14 *Height of the ray inside the cavity as a function of the number of roundtrips.*

In this configuration it is obvious that the cavity is stable and rays oscillate inside the cavity with a period of two roundtrips, meaning that every two roundtrips the rays reach at the same height.

Example 2

Confocal cavity with $|R_1| = |R_2| = L = 10\ cm$. Rays enter the cavity on the optical axis, $y_0 = 0$, with initial inclination of $\beta_0 = 0.4\ rad$,

Fig. 15 *Path of the rays inside the cavity after 50 roundtrips.*
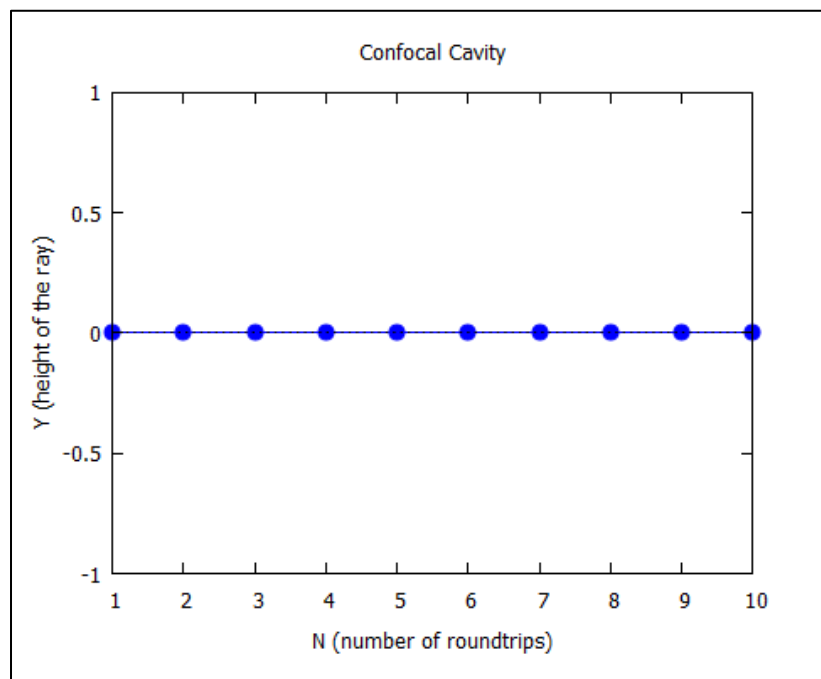

Fig. 16 *Height of the ray inside the cavity as a function of the number of roundtrips.*

In this configuration, light rays are always on the same initial height after each roundtrip and the light is limited inside the cavity.

Example 3

Cavity with one flat mirror, $|R_2| \rightarrow \infty$, the other curved with radius of curvature of $|R_1| = 40 \, cm$ and cavity length of $L = 10cm$. Rays enter the cavity at $y_0 = 0.5 \, cm$ with initial inclination of $\beta_0 = 0.1 \, rad$,
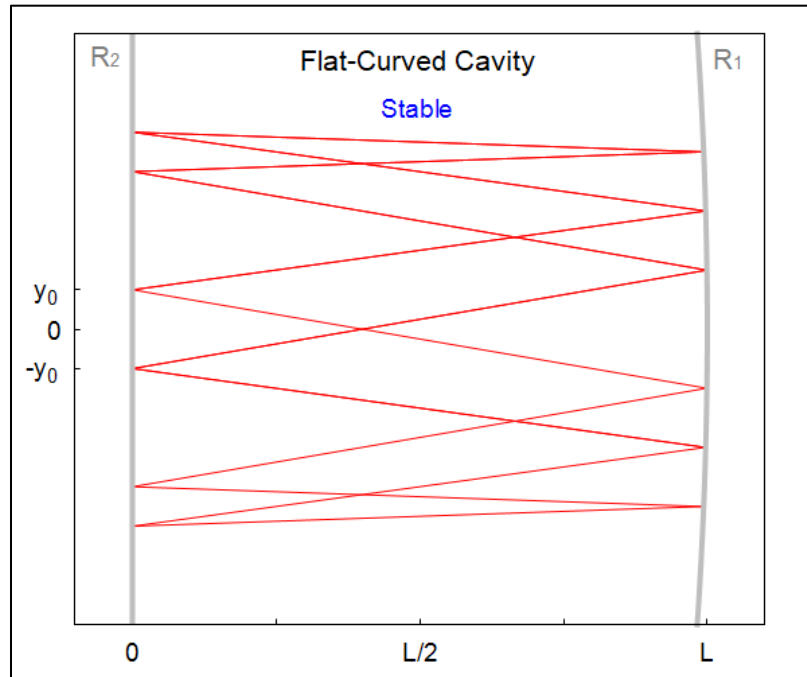

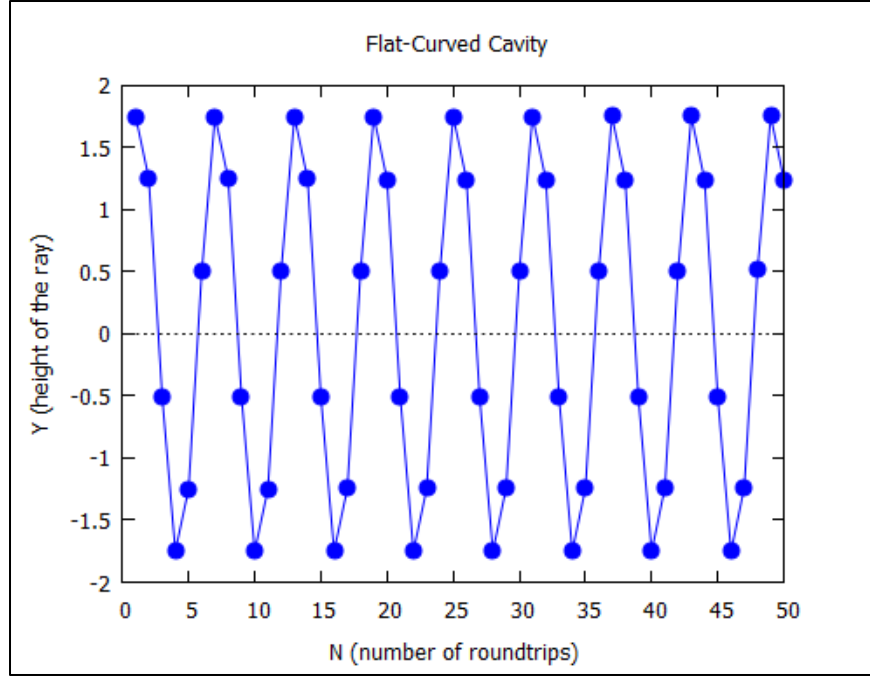**Fig. 17** *Path of the rays inside the cavity after 50 roundtrips.*

Fig. 18 *Height of the ray inside the cavity as a function of the number of roundtrips.*

This cavity is a stable one and from Fig. 18 it is obvious that the rays have a period of six roundtrips.

Example 4

Spherical cavity with $|R_1| = |R_2| = 5\ cm$ and cavity length of $L = 10\ cm$. Rays enter the cavity at $y_0 = 0.5\ cm$ with initial inclination of $\beta_0 = -0.1\ rad,$
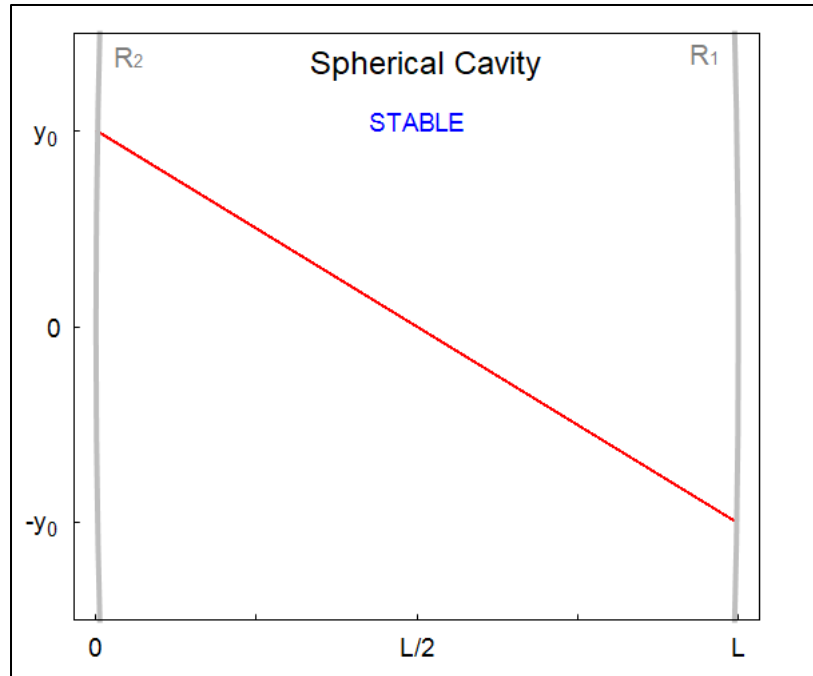
Fig. 19 *Path of the rays inside the cavity after 50 roundtrips.*
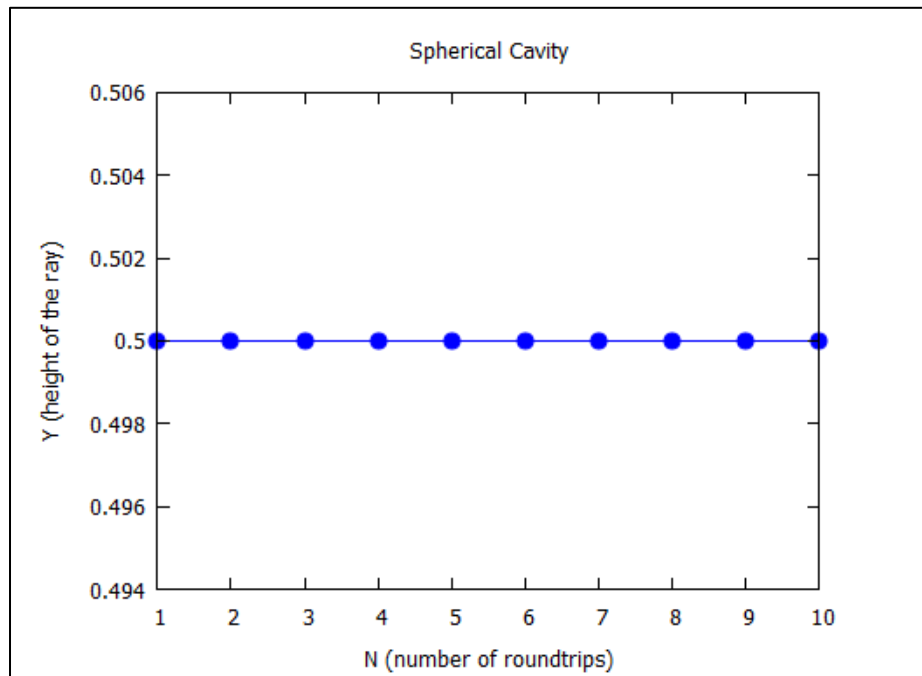

Fig. 20 *Height of the ray inside the cavity as a function of the number of roundtrips.*

From more simulations on spherical cavities, it was made clear that light is confined inside these cavities if and only if it enters so that its path passes from the middle of the optical axis at L/2. Only then a spherical cavity is stable.

Example 5

Spherical cavity with $|R_1| = |R_2| = 5\ cm$ and cavity length of $L = 10\ cm$. Rays enter the cavity at $y_0 = 0.9\ cm$ with initial inclination of $\beta_0 = -0.1\ rad$,
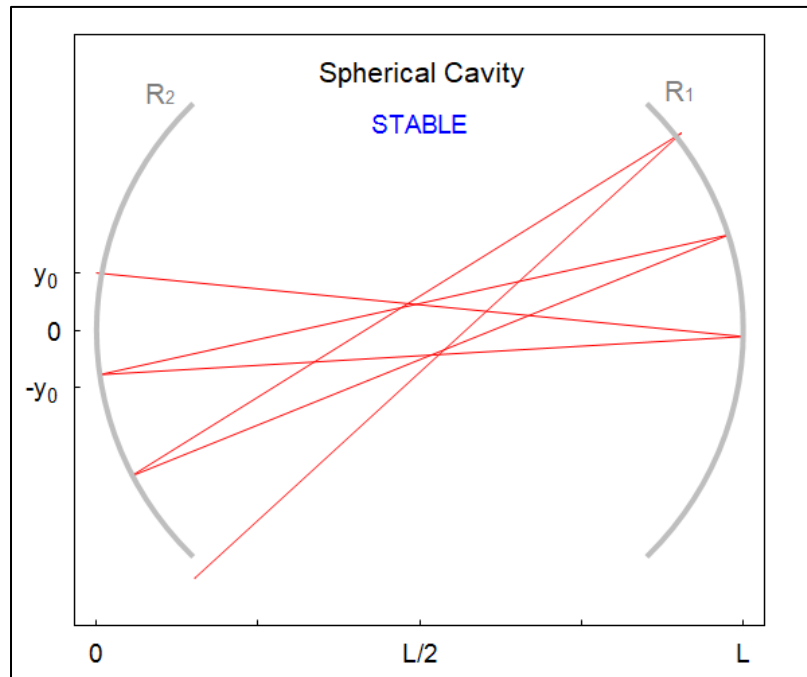

Fig. 21 *Path of the rays inside the cavity after 50 roundtrips.*

As the path of the rays does not pass through the middle of the optical axis at L/2, light will eventually leave the cavity after some roundtrips. In these cases spherical cavity is not stable.

Example 6

Random cavity with $|R_1| = 11\ cm$, $|R_2| = 12\ cm$ and cavity length of $L = (|R_1| + |R_2|)/3$. Rays enter the cavity at $y_0 = 0.9\ cm$ with initial inclination of $\beta_0 = 0.3\ rad$,
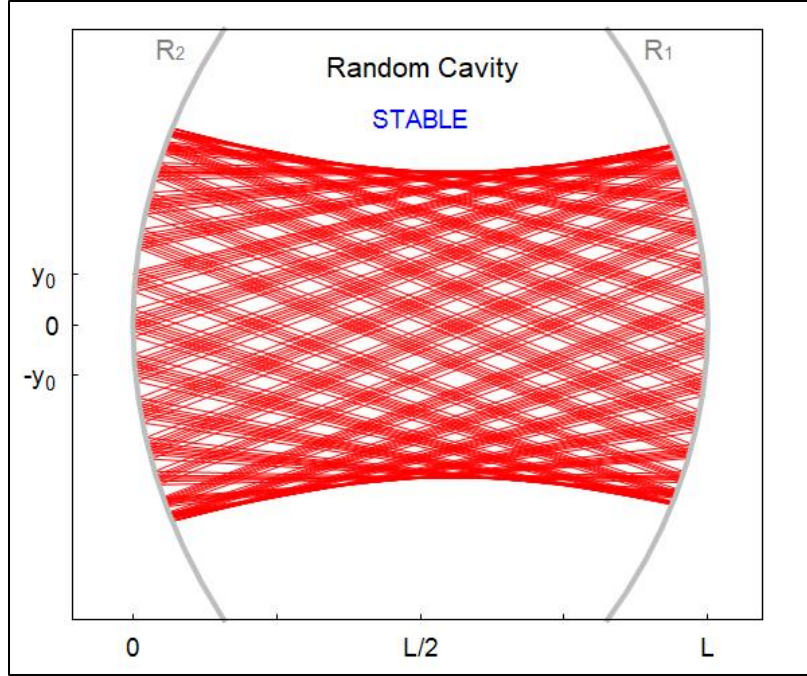
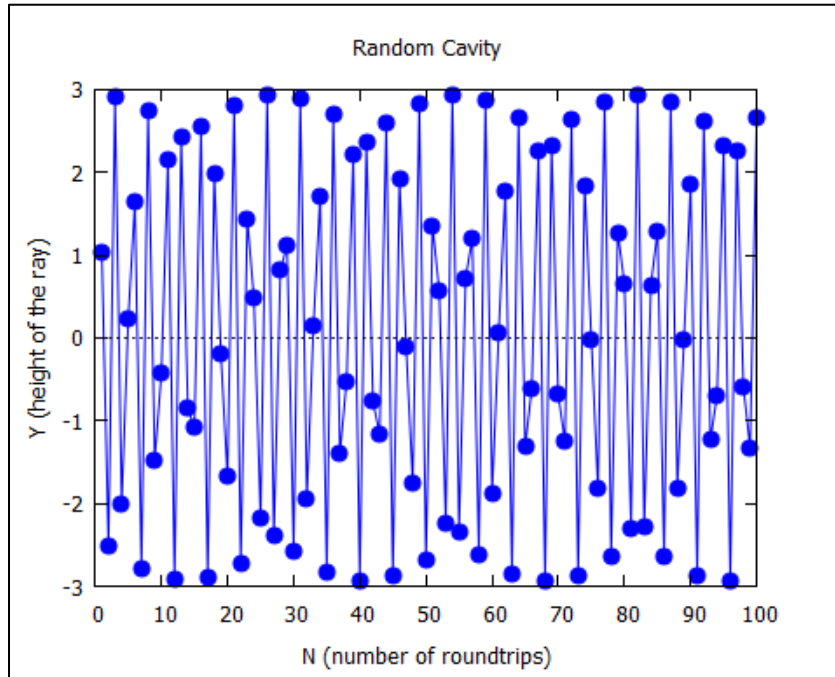***Fig. 22*** *Path of the rays inside the cavity after 100 roundtrips.*

Fig. 23 *Height of the ray inside the cavity as a function of the number of roundtrips.*

The rays inside this cavity seem to follow some periodicity and the cavity is a stable one.

2.2 Gaussian Beams

In most cases of laser light beams, the Gaussian beam profile describes the light that is emitted. Gaussian beam is a monochromatic electromagnetic wave whose both transverse electric and transverse magnetic field amplitudes, and as a result its intensity profile, are described by a Gaussian function.

In what is to follow, the space distribution function will be derived in paraxial approximation.

The time independent wave equation is given by:

$$\nabla^2 E + k^2 E = 0 \tag{58}$$

Where $k = 2\pi n/\lambda_0$ is the wavenumber and n is the index of refraction of the medium.

For the spatial solution of the above equation, one can think that the wave will have some amplitude E_o , it will propagate almost as a plane wave $\exp(ikz)$ and almost means that there will be a factor of deviation $\psi(x, y, z)$ from plane wave[5]. As a result, the expected solution will take the following form:

$$E(x, y, z) = E_o \psi(x, y, z)\exp(-ikz) \tag{59}$$

Substituting Eq.(59) to the wave equation Eq.(58) , the result is:

$$\frac{\partial^2 \psi}{\partial x^2} + \frac{\partial^2 \psi}{\partial y^2} + \frac{\partial^2 \psi}{\partial z^2} - i2k\frac{\partial \psi}{\partial z} = 0 \tag{60}$$

But in paraxial approximation the term $\partial^2\psi/\partial z^2$ is small compared to the rest of the terms, and Eq.(60) can be simplified to the paraxial wave equation:

$$\frac{\partial^2 \psi}{\partial x^2} + \frac{\partial^2 \psi}{\partial y^2} - i2k\frac{\partial \psi}{\partial z} = 0 \tag{61}$$

2.2.1 Propagation of a Gaussian Beam

Assuming cylindrical symmetry, the beam profile will be a function of the radial coordinate $r = \sqrt{x^2 + y^2}$:

$$\psi_0 = exp\left\{-i\left[P(z) + \frac{kr^2}{2q(z)}\right]\right\}$$

(62)

The deviation factor ψ_0 should contain a function $P(z)$ which will change the phase of the wave as it propagates through z axis and also a function $q(z)$ in the denominator of the Gaussian profile to change the field as it spreads out with r. Eq.(62) will be imposed to the differential equation Eq.(61) and the functions $P(z)$ and $q(z)$, which are functions of the propagation distance remain to be determined. The result is:

$$\psi_0\left\{\left[\left(\frac{k}{q(z)}\right)^2 (q'(z) - 1)\right]r^2 - 2k\left[P'(z) + \frac{i}{q(z)}\right]\right\} = 0$$

(63)

In order Eq.(63) to be valid $\forall r$, the following relations must occur:

$$q'(z) - 1 = 0$$

(64)

and

$$P'(z) + \frac{i}{q(z)} = 0$$

(65)

By integrating Eq.(64) the function of q is derived:

$$q(z) = z + q(z = 0)$$

(66)

Eq.(62) has to contain a real part for Electric field of Eq.(59) to change in the transverse plane xy. This means that $q(z = 0)$ has to be an imaginary number:

$$q(z = 0) = q_0 = iz_0$$

(67)

Calculating Eq.(62) on $z = 0$:

$$\psi_0(z = 0) = exp[-iP(z = 0)]exp\left(-\frac{kr^2}{2z_0}\right) \tag{68}$$

and the following quantity is defined, considering that the wavenumber $k = 2\pi n/\lambda_0$:

$$w_0^2 = \frac{2z_0}{k} = \frac{\lambda_0 z_0}{\pi n} \tag{69}$$

or

$$z_0 = \frac{\pi n w_0^2}{\lambda_0} \tag{70}$$

where w_0 is known as the minimum spot size (waist on z = 0) of the beam and z_0 (also symbolized in bibliography as z_R) is known as the Rayleigh range.

Considering Eq.(67) the inverse of Eq.(66) is computed:

$$\frac{1}{q(z)} = \frac{1}{R(z)} - i\frac{\lambda_0}{\pi n w^2(z)} \tag{71}$$

where the two new defined functions $R(z)$ and $w(z)$ are the radius of curvature of the beam and the waist of the beam, respectively:

$$R(z) = z\left[1 + \left(\frac{z_0}{z}\right)^2\right] = z\left[1 + \left(\frac{\pi n w_0^2}{z\lambda_0}\right)^2\right] \tag{72}$$

$$w^2(z) = w_0^2\left[1 + \left(\frac{z}{z_0}\right)^2\right] = w_0^2\left[1 + \left(\frac{z\lambda_0}{\pi n w_0^2}\right)^2\right] \tag{73}$$

Finally, $P(z)$ can be determined by integrating Eq.(65):

$$iP(z) = ln\left[1 - i\left(\frac{z}{z_0}\right)\right] \tag{74}$$

Which can be simplified considering polar coordinates of complex numbers: $c = |c|e^{i\theta}$, where $c = a + ib$, $|c| = \sqrt{a^2 + b^2}$ and $\theta = atan\left(\frac{b}{a}\right)$:

$$iP(z) = ln\left[1 + \left(\frac{z}{z_0}\right)^2\right]^{1/2} - i\,atan\left(\frac{z}{z_0}\right) \tag{75}$$

or using Eq.(73):

$$iP(z) = ln\left[\frac{w(z)}{w_0}\right] - i\,atan\left(\frac{z}{z_0}\right) \tag{76}$$

All parameters of Eq.(62) have been calculated and the free space solution under paraxial approximation (or also known as fundamental Gaussian mode) of the Electric field is:

$$E(x,y,z) = E_o\frac{w_0}{w(z)}exp\left[-\frac{r^2}{w^2(z)}\right]exp\left\{-i\left[kz + \frac{kr^2}{2R(z)} - atan\left(\frac{z}{z_0}\right)\right]\right\} \tag{77}$$

In the following image, one can clearly see the geometrical meaning of all the parameters defined earlier while the beam spreads.
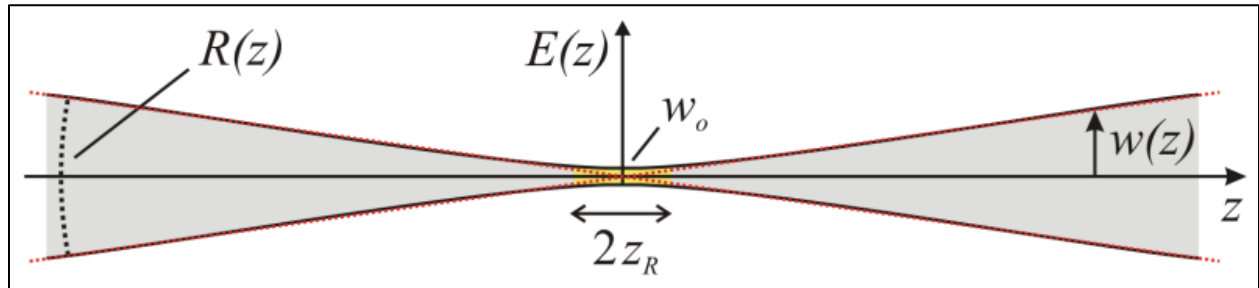

Fig. 24 *Geometrical parameters of a Gaussian beam as it propagates (taken from* [4]*).*

2.2.2 Properties of Gaussian Beams

Some important things that have to be pointed are following.

Twice the value of the polar coordinate r in which the Electric field of Eq.(77) drops to half of it's total value, is named as FWHM (Full Width at Half Maximum), and is defined as:

$$FWHM = 2\sqrt{ln2}\, w(z) \tag{78}$$

In most bibliographies, this value is referred instead of the beam waist, but they are linearly analogous quantities and there is not much difference on which one refers to.

Rayleigh range z_0 of Eq.(70) is the point on the optical axis, where the surface of the beam's spot on a transverse plane, gets doubled, or the point where the waist of the beam gets $w(z_0) = \sqrt{2}w_0$.

Fig. 13 shows the dependence of Rayleigh range as a function of the minimum waist for different wavelengths.
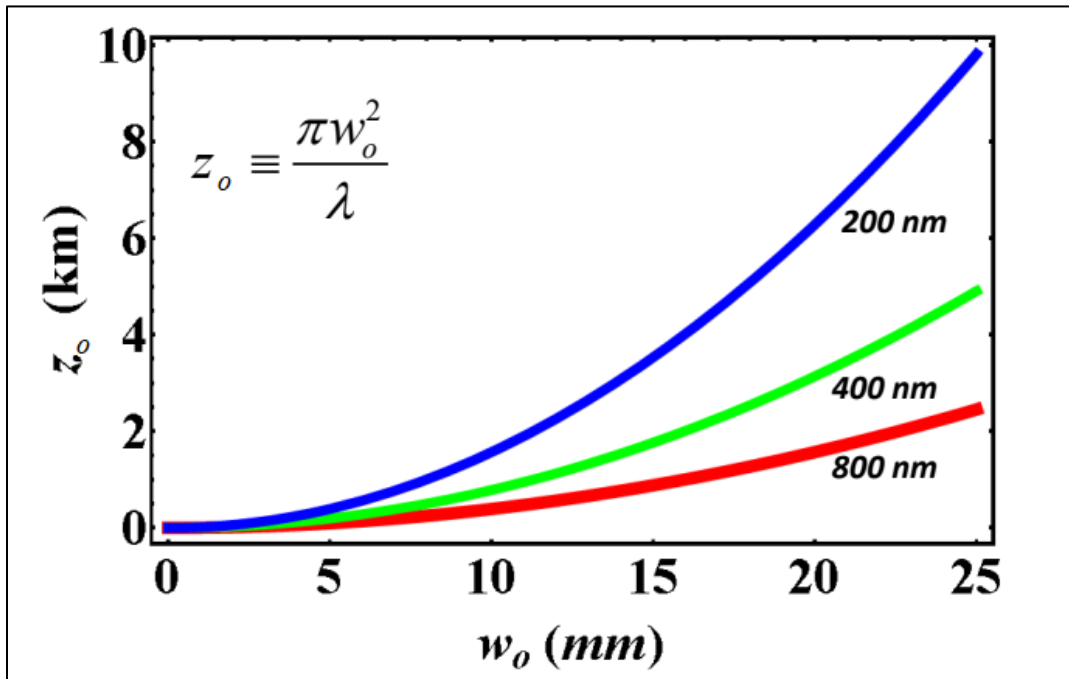

Fig. 25 *Dependence of Rayleigh range with the beam waist for different wavelengths (taken from [4]).*

It's clear that for increasing values of wavelength of the same waist, the Rayleigh range decreases, meaning that higher wavelength beams spread faster. To make this point clear, we have performed

44

numerical simulations using Virtual Lab wave propagation code (*wP*) which models the propagation of optical waves in a 1D+1 scheme using the angular spectrum approach [Ref: *wP* Virtual Lab open source wave propagator, D. G. Papazoglou (2015)].
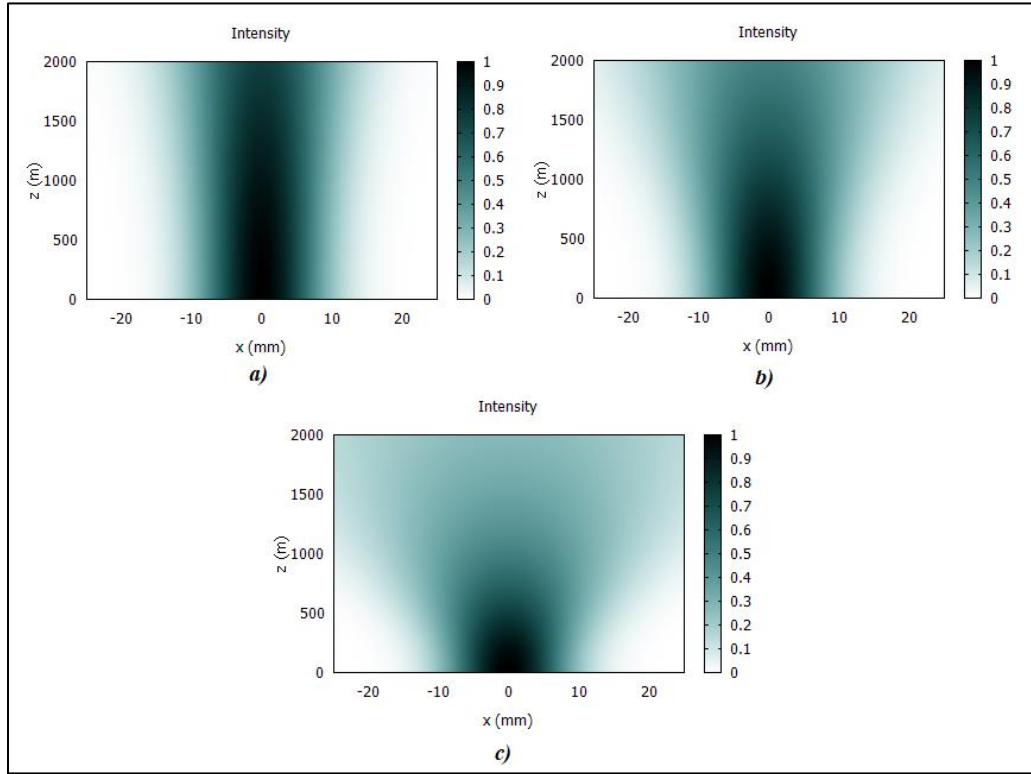

Fig. 26 *In all figures, intensities come from Electric fields that have the same FWHM=20mm (same waste) on z=0. a) refers to 200nm, b) to 400nm and c) to 800nm. Vertical axis z refers to the propagation axis and the horizontal is a transverse x direction to the propagation.*

Furthermore, from Fig. 26, one more information can be extracted, that for the same wavelength, a beam of smaller waist, spreads faster than one with a higher waist. The following simulations [Ref: *wP* Virtual Lab open source wave propagator, D. G. Papazoglou (2015)], make this point clear.

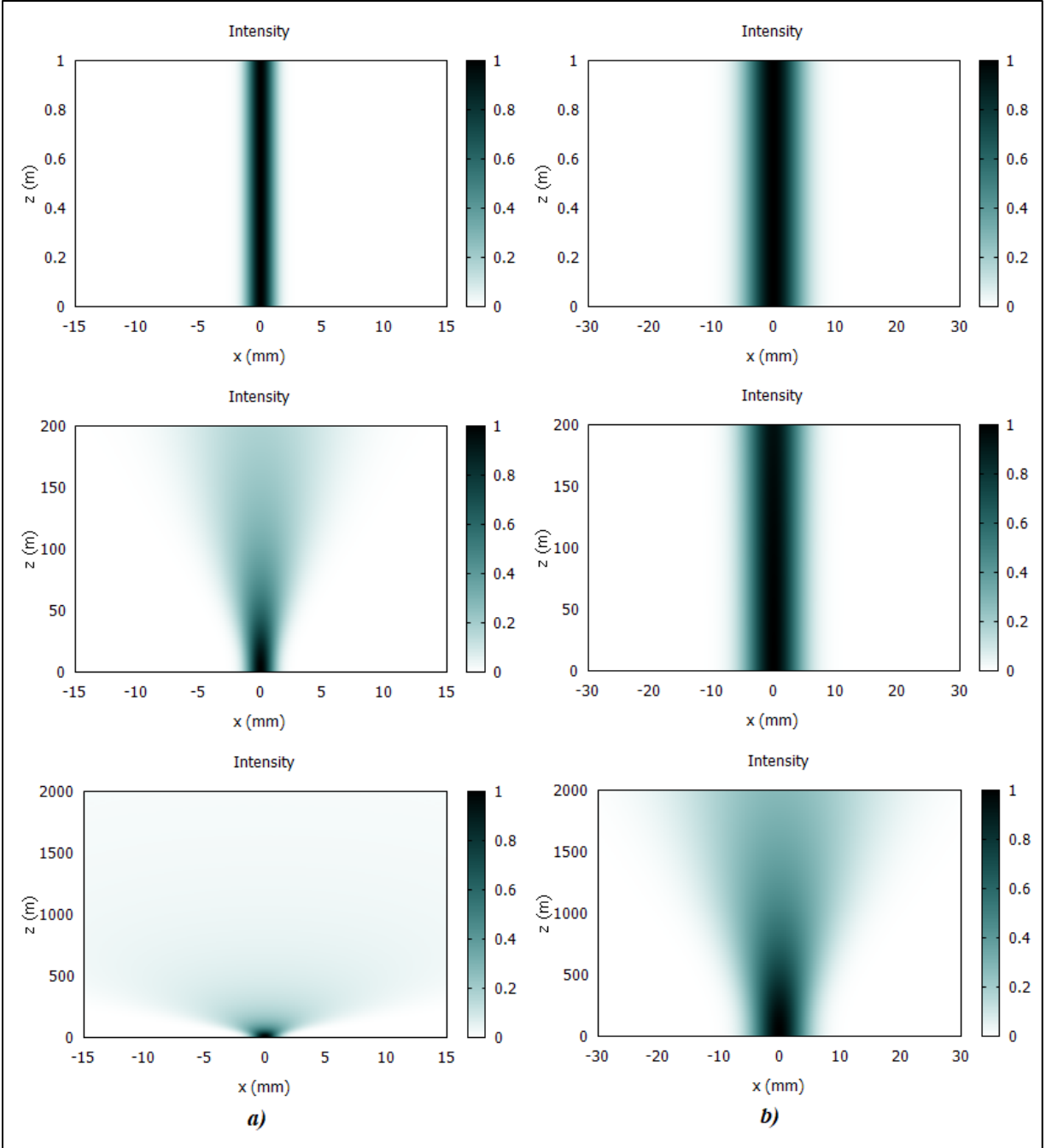***Fig. 27*** *All figures are of the same wavelength λ=200nm. The first three vertical figures named as a) refer to a FWHM=2.5mm (minimum waist on z=0), while those in b) to a FWHM=10mm. Vertical axis z refers to the propagation axis the horizontal is a transverse x direction to the propagation.*

2.2.3 ABCD Matrix Theory for Gaussian Beams

It is necessary to state that ABCD matrix theory, as described in paragraph 1.3, applies also to Gaussian beams giving information about the evolution of the beam as it propagates through an optical system.

For a Gaussian beam propagating through an optical system, from z_1 to z_2 , of a given ray transfer matrix $\begin{bmatrix} A & B \\ C & D \end{bmatrix}$, the following equation describes its propagation,

$$\begin{bmatrix} q(z_2) \\ 1 \end{bmatrix} = \begin{bmatrix} A & B \\ C & D \end{bmatrix} \begin{bmatrix} q(z_1) \\ 1 \end{bmatrix} \tag{79}$$

where $q(z)$ is the complex quantity for Gaussian beams of Eq.(66). Through matrix multiplication one can result in the following equations,

$$\begin{cases} q(z_2) = Aq(z_1) + B \\ \quad 1 = Cq(z_1) + D \end{cases} \tag{80}$$

Dividing these two equations by parts, the result is,

$$q(z_2) = \frac{Aq(z_1) + B}{Cq(z_1) + D} \tag{81}$$

From Eq.(71) it is obvious that by knowing the complex quantity q at some point z, it is possible to find the radius of curvature R and the waist w of the Gaussian beam of wavelength λ_0 , at this specific point z. An example follows to make things clear.

For a Gaussian beam being displaced by distance d in air (n=1) from z_1 to z_2 , the ray transfer matrix is $\begin{bmatrix} 1 & d \\ 0 & 1 \end{bmatrix}$. As a result, Eq.(81) yields,

$$q(z_2) = q(z_1) + d \tag{82}$$

Meaning that the complex quantity $q(z)$ have changed only by its' real part by d, as the beam propagated from z_1 to z_2.

2.3 Resonant Optical Cavities

2.3.1 Modes Inside Cavities

Gaussian beams propagating inside cavities can be described by certain wave functions depending the way they propagate. If a Gaussian beam inside a cavity displays cylindrical symmetry, then Eq.(77) is the one that describes that kind of Gaussian beam. In this section, different ways of propagation of a Gaussian beam inside a cavity, will be introduced. These different ways of propagation are known as Transverse Electric and Magnetic modes or TEM_{nm} modes and the fundamental mode TEM_{00} is given by Eq.(77).

By looking for solutions of Eq.(61) with no cylindrical symmetry $\left(\nabla_\varphi^2 \neq 0\right)$, one can get the higher modes $TEM_{n,m}$:

$$
\begin{aligned}
E(x,y,z) = E_o H_n &\left[\frac{\sqrt{2}x}{w(z)}\right] H_m \left[\frac{\sqrt{2}y}{w(z)}\right] \frac{w_0}{w(z)} exp\left[-\frac{r^2}{w^2(z)}\right] \\
&exp\left\{-i\left[kz + \frac{kr^2}{2R(z)} - (1+n+m)atan\left(\frac{z}{z_0}\right)\right]\right\}
\end{aligned}
\tag{83}
$$

with n and m being integers $(n,m = 0,1,2,...)$ and they refer to the transverse directions (x and y) to the propagation axis z.

The last exponential term of Eq.(83) denotes the phase of propagation which accumulates like a plane wave (as kz), but also has an additional Gouy phase that depends on the mode numbers ($-(1+m+p)atan(z/z_0)$) and a radial curvature term ($kr^2/2R(z)$).

where $H_p(x) = (-1)^p e^{x^2} \frac{d^p e^{-x^2}}{dx^p}$ are the Hermite polynomials of order p, some of which are stated below.

$$H_0(x) = 1$$
$$H_1(x) = 2x$$
$$H_2(x) = 4x^2 - 2 \hspace{3cm} (84)$$
$$H_3(x) = 8x^3 - 12x$$
$$H_4(x) = 16x^4 - 48x^2 + 12$$

Indexes n and m in Eq.(83) indicate how many nodes do the polynomials exhibit in x and y direction, respectively. In the following figure, some of the $TEM_{n,m}$ modes are depicted.
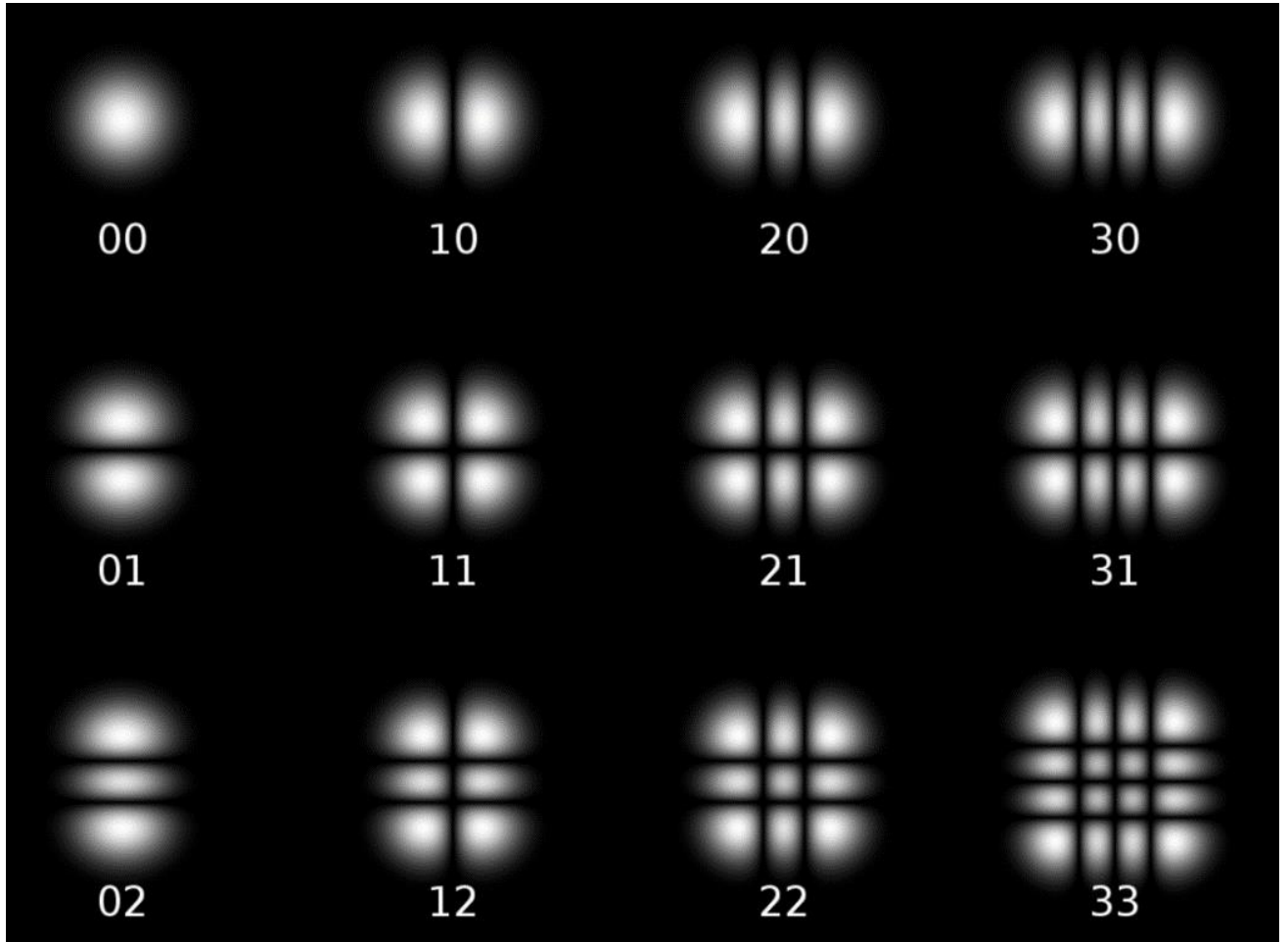

Fig. 28 *Graphical representation of some of the $TEM_{n,m}$ modes. (taken from* [10] *)*

2.3.2 Longitudinal/Axial Resonant Modes

When light enters an optical cavity, it experiences multiple reflections from both mirrors. By considering the light inside the cavity as just a plane wave, in one round trip, the factor of phase change of the wave is equal to:

$$\exp\left(-ik2L\right) \tag{85}$$

where k is the wavevector and L is the cavity length.

If the phase change is an integral multiple of 2π this means that the cavity is on resonance. This is called resonance condition:

$$2kL = q2\pi \tag{86}$$

where q is an integer number $(q = 1,2\dots)$.

Considering that $k = 2\pi n/\lambda_0$ and $n = \lambda_0/\lambda$, Eq.(86) can be written as:

$$L = \frac{q\lambda}{2} \tag{87}$$

which is a familiar result for someone that has studied wave mechanics. It reminds the condition for standing waves of some wavelength λ on a string of length L. Indeed, this is the case. Eq.(87) states that there must fit integral multiples of half the wavelength between the cavity mirrors. This is what the following image depicts.
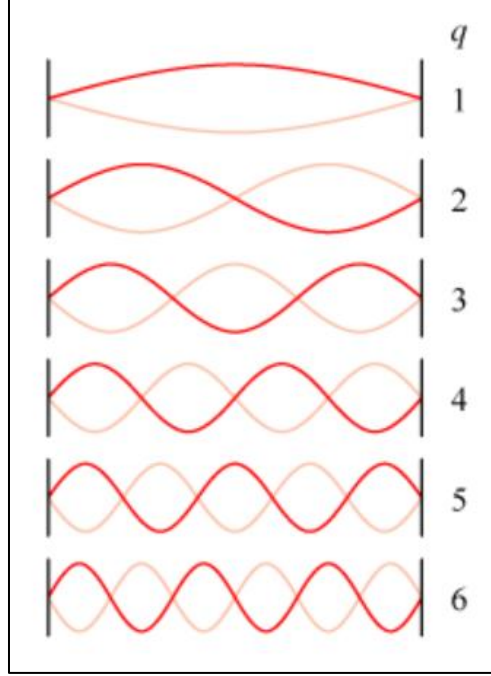
Fig. 29 *Longitudinal/axial modes inside a cavity (taken from* [11]*).*

In terms of frequency, considering that $\lambda = c/v$ and $c = c_o/n$, Eq.(87) results in,

$$v = q\frac{c_0}{2nL}$$

(88)

and for two consecutive resonant frequencies,

$$\Delta v = v_{q+1} - q_v = \frac{c_0}{2nL}$$

(89)

This spacing between two resonant frequencies in known as FSR (Free Spectral Range):

$$FSR = \frac{c_0}{2nL}$$

(90)

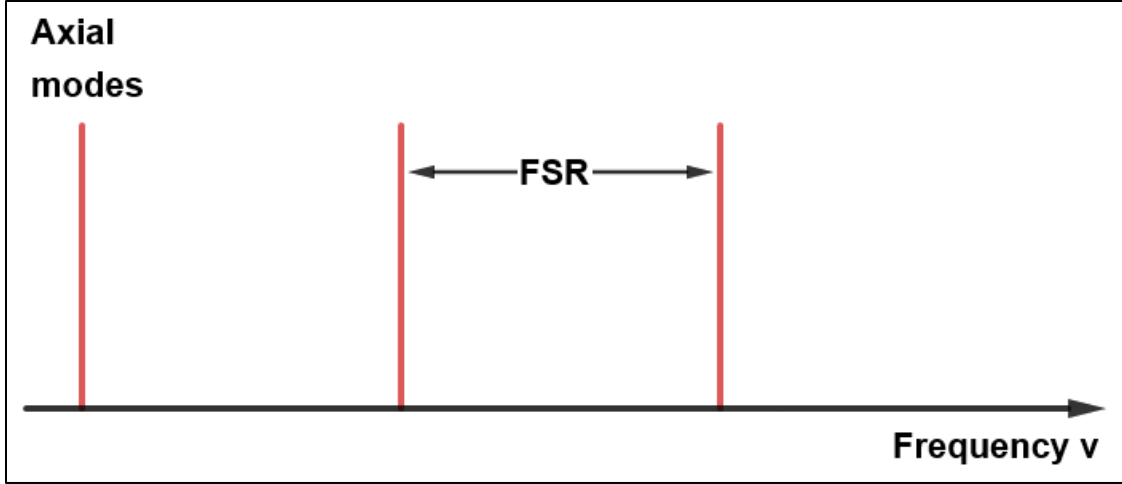In the following picture, there is a schematic description of the resonant frequencies.

Fig. 30 *Red lines represent only three of the longitudinal/axial resonant modes inside a cavity.*

2.3.3 Higher-Order Resonant Modes

By considering that the light inside the cavity has the general form of Eq.(83), higher-order modes arise, known as Hermite-Gaussian modes.

When cavity is on resonance, light described by Eq.(83) reproduces itself in both relative shape and phase after one round trip. Essentially, this occurs when a cavity's mirrors match exactly the beam wavefront. These boundary conditions fix the focus relative to the mirror positions. In the following image, a resonant cavity is depicted. At $z = 0$ is taken to be the beam waist or the focus inside the cavity and $L = z_2 + z_1$ is the length of the cavity. At points z_2 and $-z_1$ the radius of curvature of the beam, perfectly fits the curvature of the two mirrors.
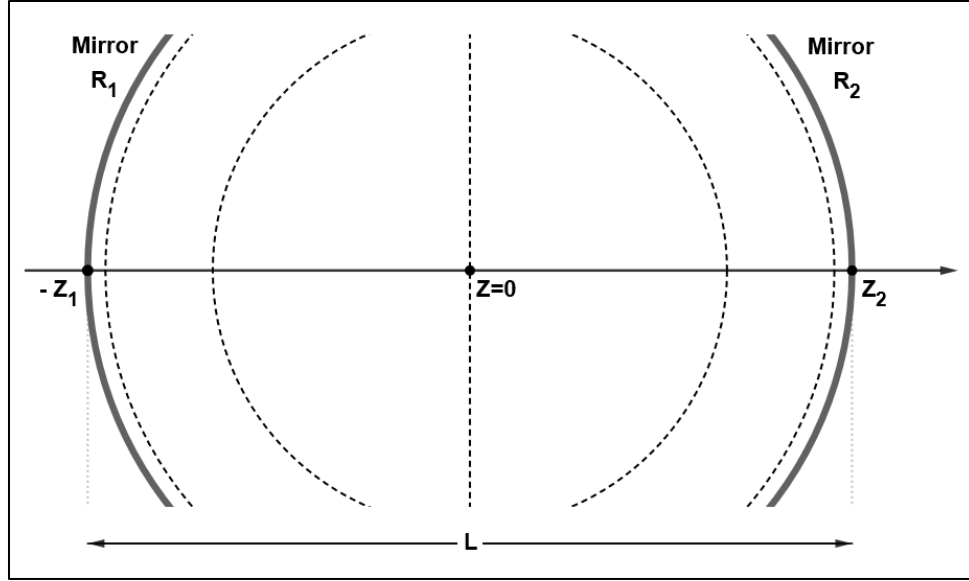
Fig. 31 *Wavefronts (dashed lines) inside a resonant cavity.*

In this case, the effect of the mirrors is to simply reverse the wavevector k of the light beam. After one roundtrip, light returns to itself.

From Eq.(83) the phase of the wave inside the cavity will be:

$$\varphi(r,z) = kz + \frac{kr^2}{2R(z)} - (1+n+m)atan\left(\frac{z}{z_0}\right) \tag{91}$$

Working on the optical axis $(r = 0)$, the phase change in one roundtrip, is twice the phase change accumulated from z_1 to z_2:

$$\Delta\varphi_{rt} = 2[\varphi(0,z_2) - \varphi(0,-z_1)] \tag{92}$$

or,

$$\Delta\varphi_{rt} = 2kL - 2(1+n+m)\left[atan\left(\frac{z_2}{z_0}\right) - atan\left(\frac{z_1}{z_0}\right)\right] \tag{93}$$

As stated in Eq.(86), for resonant cavities, the phase change for one roundtrip must be integral multiple of 2π, and by rearranging Eq.(93):

$$2kL = q2\pi + 2(1 + n + m)\left[atan\left(\frac{z_2}{z_0}\right) - atan\left(\frac{z_1}{z_0}\right)\right] \tag{94}$$

But $kL = 2\pi nL/\lambda_0 = 2\pi nvL/c_0$ and from Eq.(90) $kL = \pi n/FSR$. As a result, Eq.(93) gets the following form:

$$v = FSR\left\{q + \frac{(1 + n + m)}{\pi}\left[atan\left(\frac{z_2}{z_0}\right) - atan\left(\frac{z_1}{z_0}\right)\right]\right\} \tag{95}$$

In order to simplify the Gouy phase terms, Eq.(72) will be used, calculated in z_2 and $-z_1$, accompanied by the length of the cavity $L = z_2 + z_1$:

$$R(-z_1) = -R_1 = -z_1\left[1 + \left(\frac{z_0}{z_1}\right)^2\right] \tag{96}$$

$$R(z_2) = R_2 = z_2\left[1 + \left(\frac{z_0}{z_2}\right)^2\right] \tag{97}$$

$$L = z_2 + z_1 \tag{98}$$

The equations above, comprise a 3x3 system that can be solved. The results are:

$$z_0^2 = \frac{d(R_1 - L)(R_2 - L)(R_1 + R_2 - L)}{(R_1 + R_2 - 2L)^2} \tag{99}$$

$$z_1 = \frac{L(R_2 - L)}{R_1 + R_2 - 2L} \tag{100}$$

$$z_2 = \frac{L(R_1 - L)}{R_1 + R_2 - 2L} \tag{101}$$

Using these results in Eq.(95) and simplifying it further, one can get:

$$v = FSR\left\{q + \frac{(1+n+m)}{\pi} \, acos\left[\sqrt{sign\left[2L\left(\frac{R_1+R_2}{2L}-1\right)\right]\left(1-\frac{L}{R_1}\right)\left(1-\frac{L}{R_2}\right)}\right]\right\} \quad (102)$$

Looking at some special case, where the first mirror is flat and is located on $z = 0$, the second is curved with radius R_2 located on $z_2 = L$ and that the cavity is resonant (phase fronts matches exactly the mirror curvatures), one can get:

$$R(z_2) = R_2 = L\left[1 + \left(\frac{z_0}{L}\right)^2\right] \quad (103)$$

and solving for z_0 :

$$z_0 = \sqrt{(LR_2)\left(1 - \frac{L}{R_2}\right)} \quad (104)$$

But, z_0 is the Rayleigh range, a real and measurable quantity. This means that:

$$1 - \frac{L}{R_2} \geq 0 \quad (105)$$

or

$$\frac{R_2}{L} \geq 1 \quad (106)$$

In a similar way, the same relation can be argued for:

$$\frac{R_1}{L} \geq 1 \quad (107)$$

Adding up Eq.(106) and Eq.(107) , the result is:

$$\frac{R_1 + R_2}{2L} - 1 > 0 \tag{108}$$

And now it is clear that $sign\left[2L\left(\frac{R_1+R_2}{2L} - 1\right)\right] = +1$ in Eq.(102). Thus, the final relation for higher order modes is:

$$v_{qnm} = FSR\left\{q + \frac{(1+n+m)}{\pi} acos\left[\sqrt{\left(1 - \frac{L}{R_1}\right)\left(1 - \frac{L}{R_2}\right)}\right]\right\} \tag{109}$$

or using $g_i = 1 - \frac{L}{R_i}$ as it was defined in ABCD matrices for the stability condition $0 \leq g_1 g_2 \leq 1$:

$$v_{qnm} = FSR\left\{q + \frac{(1+n+m)}{\pi} acos\left(\sqrt{g_1 g_2}\right)\right\} \tag{110}$$

where, index q refers to the longitudinal modes and indices n and m to the transverse x and y modes.

From Eq.(109) it is obvious that more resonant frequencies have added up to the longitudinal/axial ones. These extra resonant frequencies are shown in the image below:
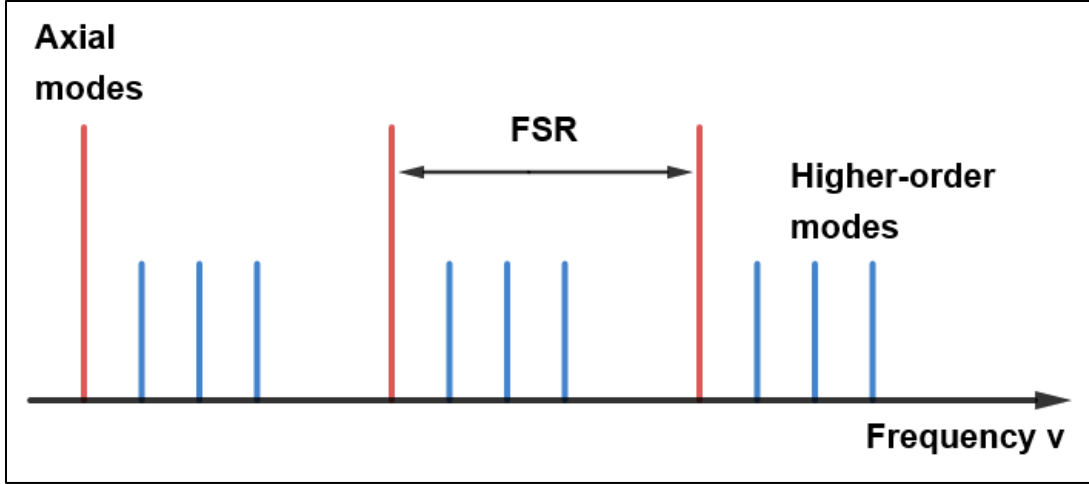
Fig. 32 *Longitudinal (axial) and the transverse modes in a cavity as a function of frequency.*

2.3.4 Degenerate Modes

Examining Eq.(110), it is possible to eliminate the Gouy term $\frac{(1+n+m)}{\pi} acos\left(\sqrt{g_1 g_2}\right)$ when $\sqrt{g_1 g_2} = 1$. This can occur for certain geometries like, for example, the concentric cavity, where $R_1 = R_2 = R$ and $L = 2R$ or the two plane mirrors cavity, where $R_1 = R_2 \to \infty$.

These cavities are referred to as degenerate because the resonant frequency v_{qnm} depends only on the longitudinal mode index q and if the same for all transverse modes n and m. Schematically, this means that in Fig.(32) all the higher order modes have collapsed to the axial mode.

Chapter 3 - Imaging System Design

In this chapter, we are going to present the optical system designed for the imaging part of our experiment. Optical design is the process of designing an optical system in order to comply with the required specifications like, for example, performance goals.

We will start by discussing about some important parameters, which characterize the performance of an imaging system and optical aberrations. Next, we will introduce an existing imaging system and then we are going to combine it with the cavity and evaluate its performance.

3.1 Performance Parameters and Optical Aberrations

Some important quantitative parameters that characterize the performance of an imaging system are the numerical aperture NA and the optical resolution.

3.1.1 Numerical Aperture

Numerical aperture NA was defined in section 1.2 and is given by Eq.(9) $NA = n\,sin\theta$. This quantity is restricted by the size of the first optical element (e.g. lens) after the light source, as rays are limited by the size of the lens (this can be seen in the following image). In that sense, numerical aperture has a maximum value when $\theta = \theta_{max}$.
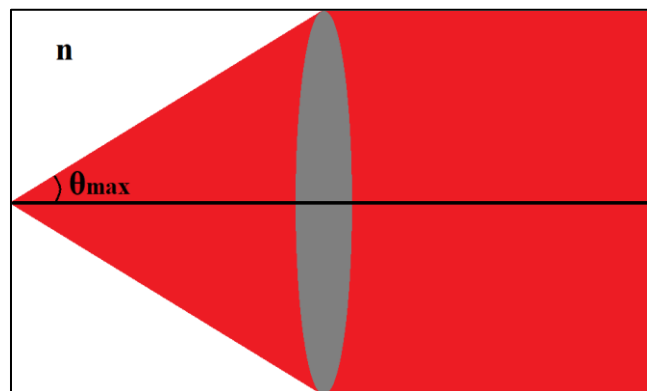

Fig. 33 *Light rays limited by the size of a lens.*

3.1.2 Optical Resolution

Optical resolution R, is defined as the minimum distance that an imaging system can separate between two point sources on the object [12]. It is affected by the numerical aperture NA, the wavelength λ of the source used and is given by,

$$R = \frac{0.612\lambda}{NA} \tag{111}$$

Optical resolution R is straightforwardly connected to the angular resolution of an imaging system which is the smallest angle between two different point sources that can be distinguished.

In microscopy, there is a limit of optical resolution R which is restricted by the wave nature of light due to diffraction. When light of a point source passes through a small circular aperture, diffraction of light occurs and a diffraction pattern is produced known as Airy pattern and the central brighter disc known as Airy disk. This pattern can be seen in the following image.
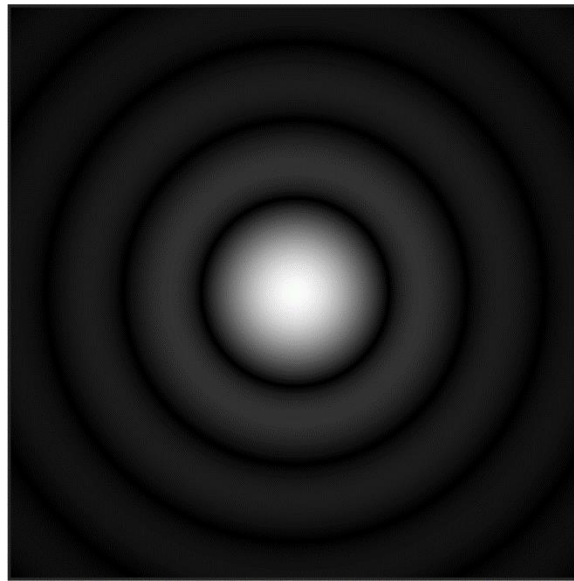

Fig. 34 Airy pattern due to diffraction from circular aperture. (taken from [13])

Airy disk defines the limit of resolution R that can be achieved by an imaging system, which is the smallest radius of the spot in image plane where an optical system can focus a light beam.

Rayleigh Criterion states that two objects will be resolved when they have at least distance R between them. In other words, this Criterion describes the ability of an imaging system to separate between two Airy discs coming from two different point sources in the diffraction pattern. In this case, the imaging system is said to be diffraction limited. This can be seen in the following image.
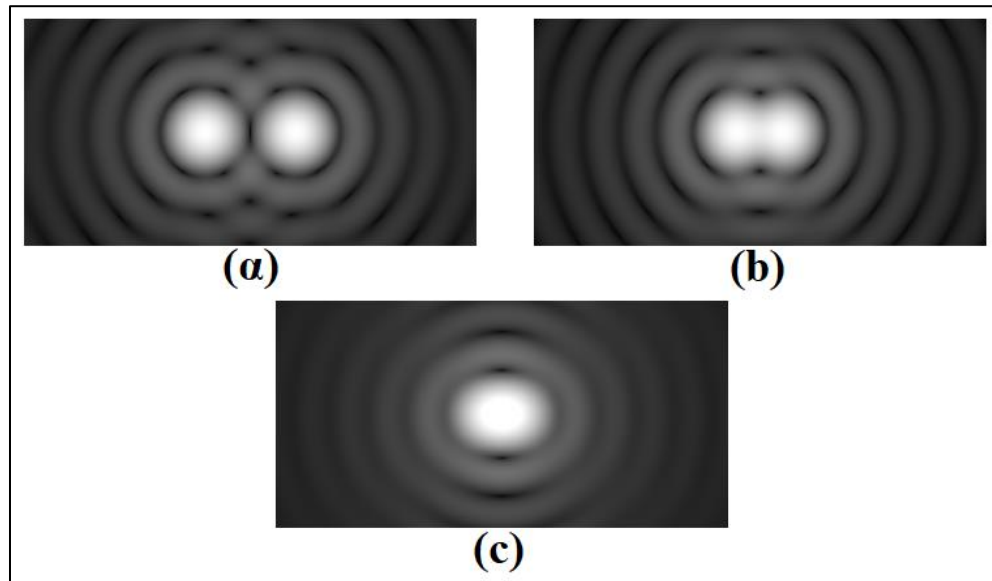

Fig. 35 *Airy discs coming from two different point sources of distance between them (a) greater than R, (b) equal to R (Rayleigh Criterion), (c) less than R. In (a) and (b) the two different point sources can be distinguished while in (c) they can't. (taken from* [14] *)*

3.1.3 Optical Aberrations

Optical aberrations refer to any deviation of the performance of an optical system from the ideal paraxial approximation predictions [15]. They are caused due to the geometry or the imperfections of the optical elements (e.g. lenses) used, or due to the fact that different wavelengths follow different paths when propagating in matter. Aberrations cause deformations to the ideal paraxial shape of the waveform that exits an optical system. As a result, the image formed in the exit of an optical system is either blurred or distorted depending on the type of the existing aberration [7]. In order to deal with aberrations when designing an imaging system, lenses with opposite sign aberrations (e.g. converging and diverging lenses) are combined together, trying to eliminate aberrations through the whole optical system as much as possible.

Aberrations are divided in two types, the monochromatic and chromatic aberrations [16]. Monochromatic aberrations are spherical aberrations, coma, astigmatism, field curvature, image distortion and defocus, while chromatic are divided in longitudinal and transverse aberrations.

For the purpose of this thesis, in what is to follow, only some monochromatic aberrations will be discussed.

Spherical aberrations

An ideal/thin lens, focuses all light rays passing along the lens in one point, as one can see in the following picture.
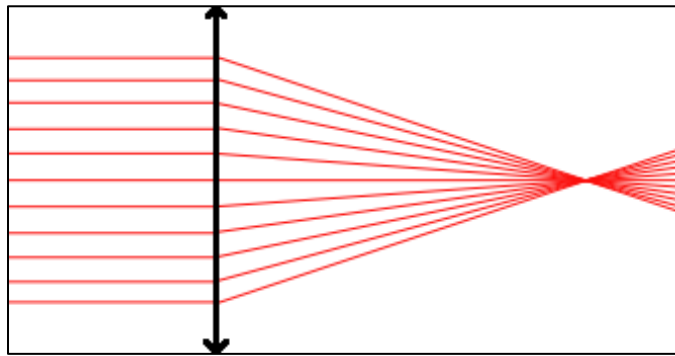

Fig. 36 *Perfect lens focuses all light rays in one point. (taken from* [17]*)*

But, of course, ideal lenses do not exist. Due to the geometry (curvature) and the thickness of the lens shown in Fig.(36), light rays coming from the edges of the lens (marginal rays) propagate in a shorter distance inside the lens and therefore they are refracted earlier than the rays near the optical axis (paraxial rays). As a result, lenses are unable to focus all light rays in the same point, as it is depicted in the following image.
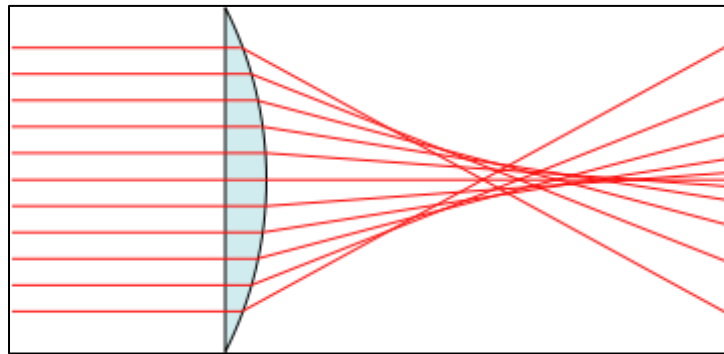

Fig. 37 *In a non-ideal lens, light rays do not focus at the same point in the exit. (taken from* [17]*)*

When the focal length of marginal rays of a lens is shorter than the focal length of its paraxial rays, the lens is characterized by positive spherical aberration, like the converging lens in Fig.(37). The opposite means that the lens is characterized by a negative spherical aberration (e.g. diverging lens). Consequently, spherical aberrations can be reduced by combining lenses of opposite spherical aberration.

Coma aberration

Coma aberration appears when the object we want to image is not located on the optical axis. It is defined as a variation in transverse magnification between marginal and paraxial rays and as a result, the image appears to have a tail (like a comet) known as coma tail. To deal with this aberration, one can tilt the lens or the whole optical system in order to locate the object on the optical axis [18].
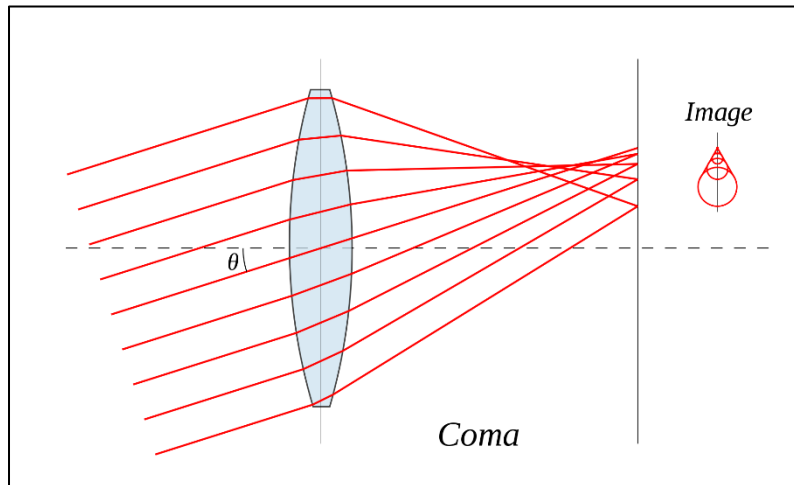

Fig. 38 *Coma aberration and the coma tail formed in the image plane. (taken from* [19]*)*

3.2 Optical Simulation Software

Nowadays, there are several optical simulation softwares that are used widely to design and analyze imaging systems. Zemax-OpticStudio [20] is a well-known raytracing optical software which we used for the purposes of this Master thesis. This software helped us to design our imaging system, evaluate its performance and tried to improve the performance further.

Getting started with Zemax, we need to define the actual optical materials comprising our optical system, in Zemax's interface. For example, this means that we need to define radii of curvature of

the two surfaces of a lens, its thickness and diameter and the type of the material (glass type) that it is made up from. Moreover, Zemax comes with built-in libraries that contain data for various lenses from many optics design companies and can use them straightforward instead of designing lenses from scratch.

As an example of designing an optical system using Zemax we perform the following steps. After creating the optical system we want, we choose type of source (e.g. point source of some NA), we choose the wavelength of the light rays and Zemax creates a layout showing how rays propagate in the optical system (Fig. 39) and a spot diagram calculating the spread of the rays at the end of the optical system scaled to the Airy disk (black circle) diameter (Fig. 40).
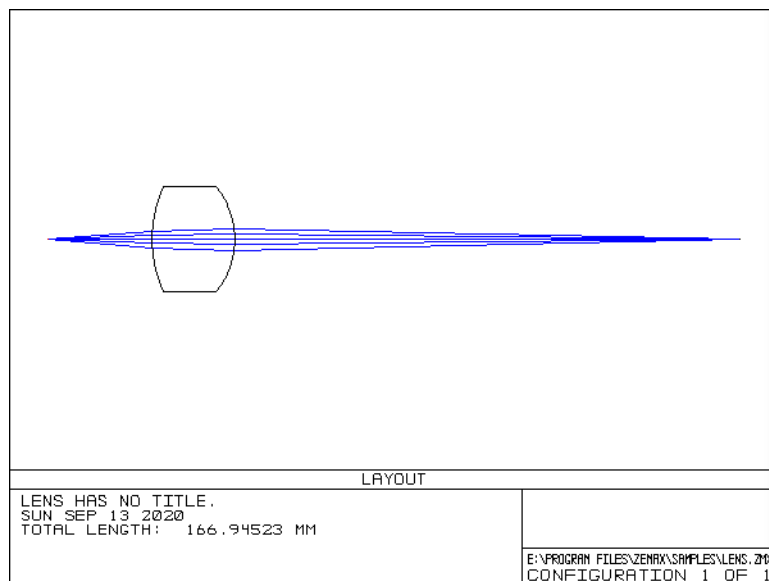

LAYOUT

LENS HAS NO TITLE.
SUN SEP 13 2020
TOTAL LENGTH: 166.94523 MM

E:\PROGRAM FILES\ZEMAX\SAMPLES\LENS.ZMX
CONFIGURATION 1 OF 1

Fig. 39 *Layout example in Zemax optical design software. Light rays (in blue) propagate through a lens.*
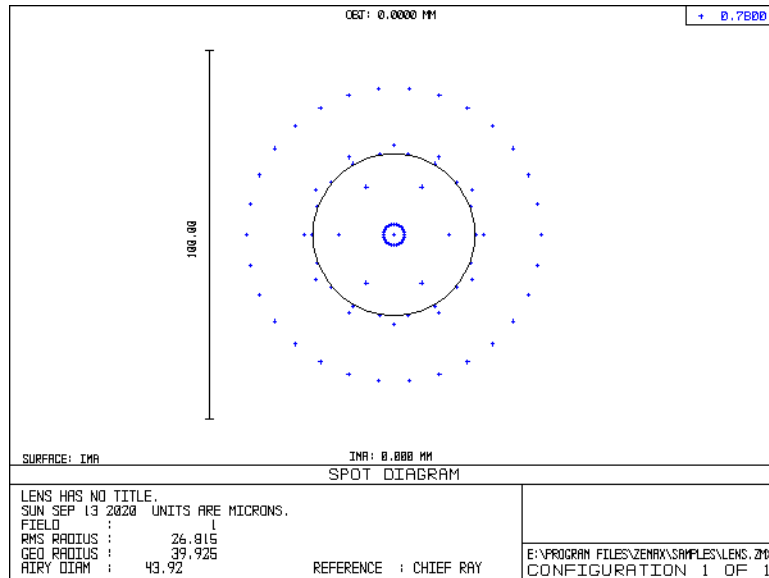
Fig. 40 *Spot diagram example in Zemax optical design software. Spot of the rays at the end of the optical system shown in Fig. 39 and the corresponding Airy disk (black circle).*

The spread of the rays shown in Fig. 40 of our example, is caused by spherical aberrations described in the previous section.

Zemax also gives the ability to move the light source off the optical axis or even to rotate either parts of the optical system or the whole optical system with respect to some axis. Furthermore, it can automatically optimize an optical's system performance, using the merit function which is defined as a least square function. At first, we need to define the optimization parameters. Such parameters can be the radius of curvature of an optical element or the distance between two optical elements. Next, the optimization target needs to be defined. For instance, we want to minimize the spot size of the light rays coming out from our imaging system (minimize with respect to RMS radius depicted in Fig. 40). Finally, we let Zemax run the optimization and it stops when the merit function reaches as close to zero as possible, giving us the optimized values for each of the parameters defined.

3.3 Designing the Imaging System

For the purpose of this master thesis, we want to combine the cavity with two optical systems, one before the cavity and one after the cavity. In this way, the optical system before the cavity will drive light inside the cavity to interact with our specimen and the latter optical system will collect light coming out of the cavity in order to create our image, as we can see in the following figure.
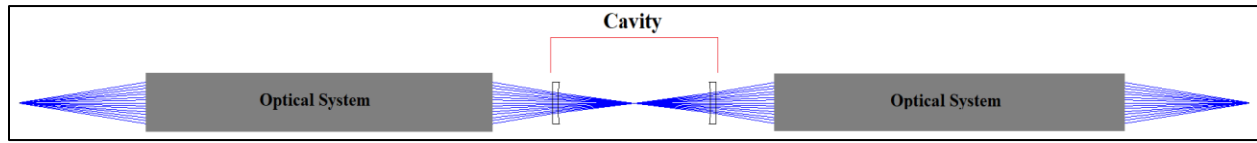
Fig. 41 *Optical system before the cavity will drive light inside the cavity to interact with our specimen and the latter optical system will collect light coming out of the cavity in order to create our image.*

At this point, we are going to present an existing imaging system, that was used in the past in our laboratory. Back in 2011 Dr. Melina Pappa, published her PhD research [21], which took place in Cretan Matter Waves (BEC) laboratory and for the purpose of her research, she constructed a *4 f* imaging system.

The imaging system is comprised of two identical lensets and each lenset is composed of an achromatic doublet (Melles-Griot, LAO-160.0-31.5-780) and a meniscus lens (Melles-Griot, MENP-31.5-6.0-233.6-780). Between the two lenses there is a 1mm distance.

Using Zemax, we optimized the distances for the lensets using a merit function, in order to get a minimized RMS radius (for NA=0.12 and a wavelength of 780nm). A layout is shown in the following image for a source on the optical axis of the system.
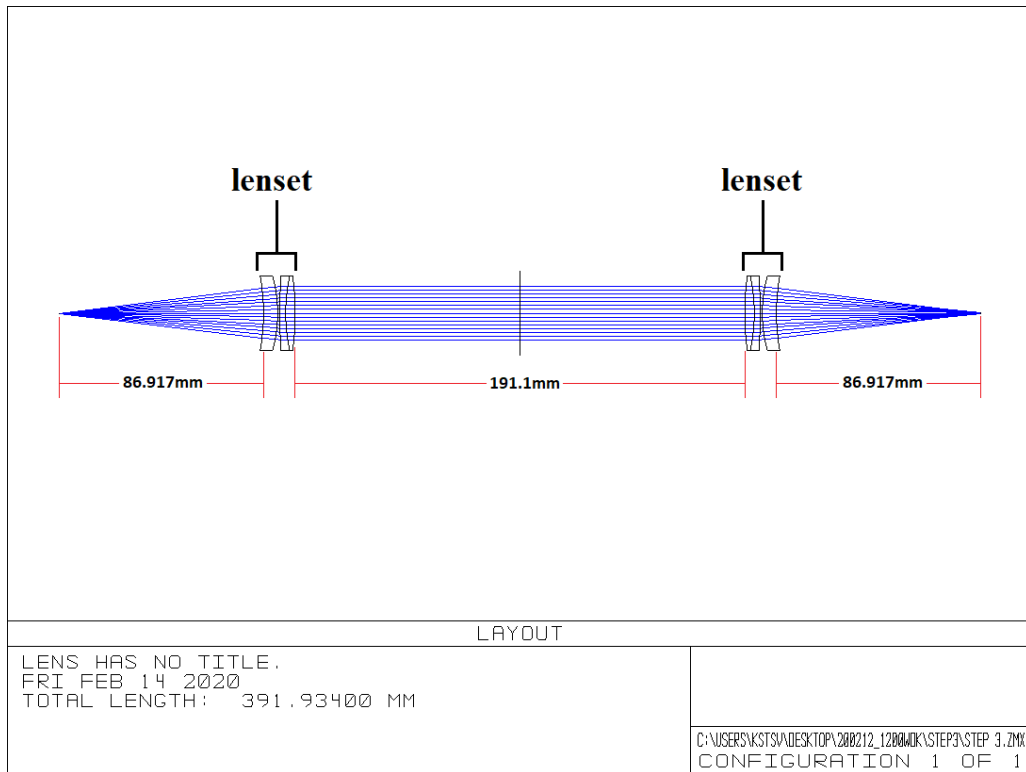
Fig. 42 *A layout of the existing imaging system with distances optimized with respect to the RMS radius of the spot in the image plane. The system is symmetric.*

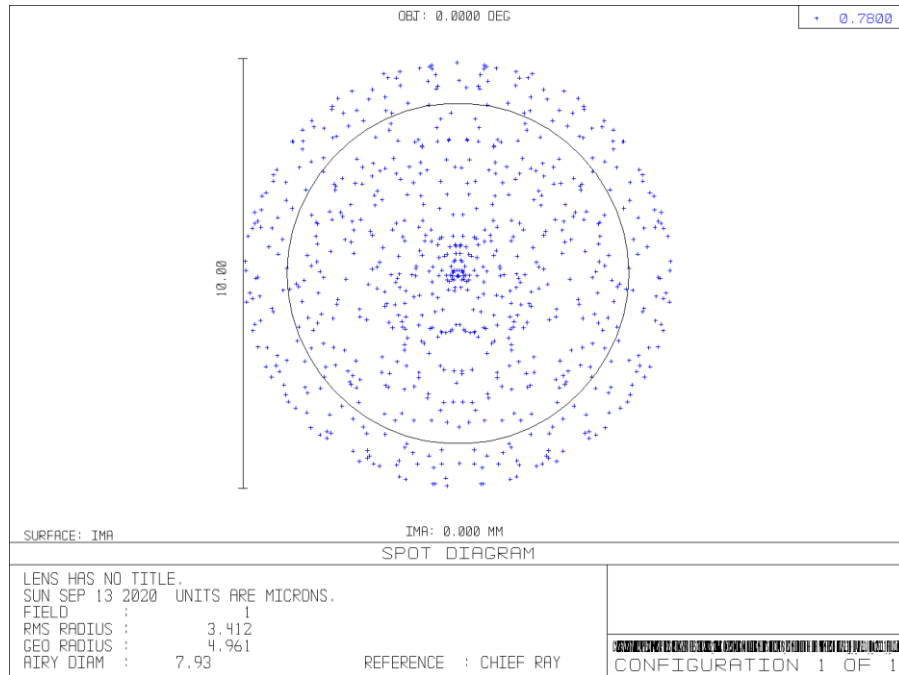And the corresponding spot diagram is the following.

Fig. 43 *Spot diagram of the optimized existing imaging system.*

As we can see the resolution corresponds to an Airy disk of 7.93μm diameter and the RMS radius is 3.4μm. This means that the imaging system is very close to the diffraction limit, as Dr. Pappa states in her thesis.

Due to its good performance and the fact that this imaging system is available in the BEC lab, we are going to combine it with the cavity. So, as we can see in the following figure, we will use the existing imaging system before and after the cavity, to serve as the optical systems in Fig.41.
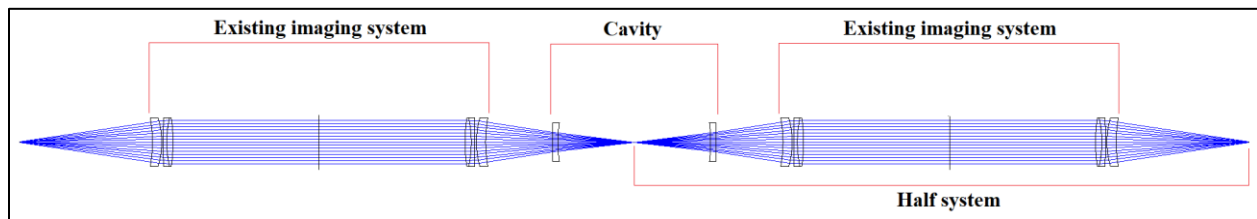

Fig. 44 *Cavity combined with the existing imaging system.*

Next step is to check the performance of this whole system in Zemax. But as we can see in Fig.44, the system is symmetric and we only need to check the performance for half the system, as we do in the following sections.

3.4 Cavity Combined with the Existing Imaging System

At this stage of the thesis, we are ready to combine an optical cavity with the imaging system described previously and check for its performance.

3.4.1 Confocal Cavity composed of Plano-Concave Mirrors

3.4.1.1 Source on the optical axis

At first, we want to check the performance of a confocal cavity comprised of two plano-concave mirrors (Laseroptik - S-00071) which have radius of curvature $R = -100mm$. This means that each mirror must have a distance of 50mm from the center of the cavity where we will place the specimen we want to image, as we can see in the next figure.
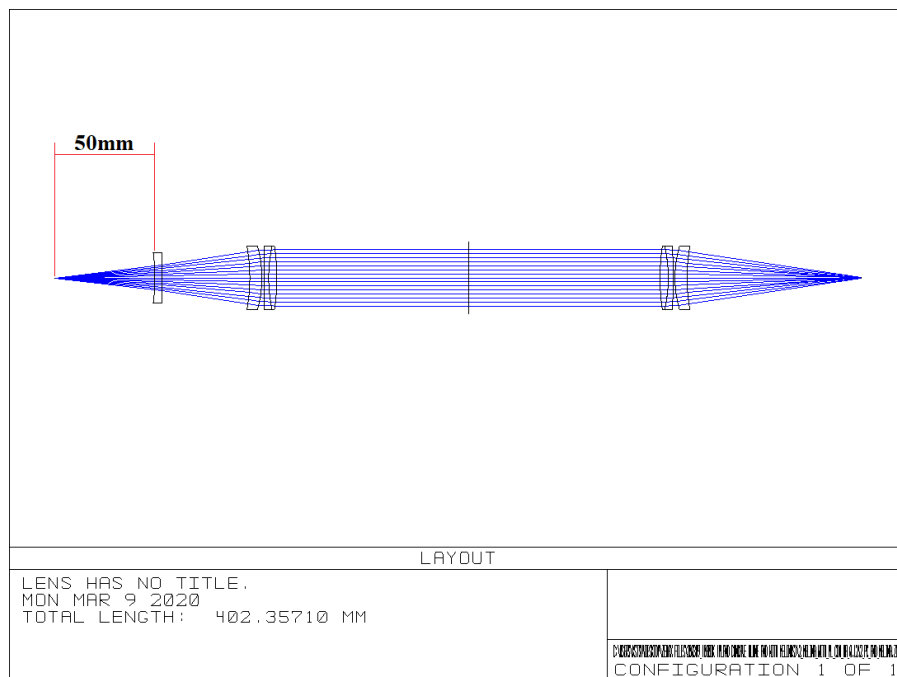

Fig. 45 *Layout of the confocal cavity combined with the imaging system.*

From now on, all optimizations are performed for NA=0.12 and λ=780nm.

We will now optimize the distance between the plano-concave mirror and the first element of the imaging system using merit function, in order to minimize the spot of the image at the end of the system. The optimal distance we find is 43.94mm, as it is depicted bellow. The rest of the distances not shown are the same as in Fig.42.
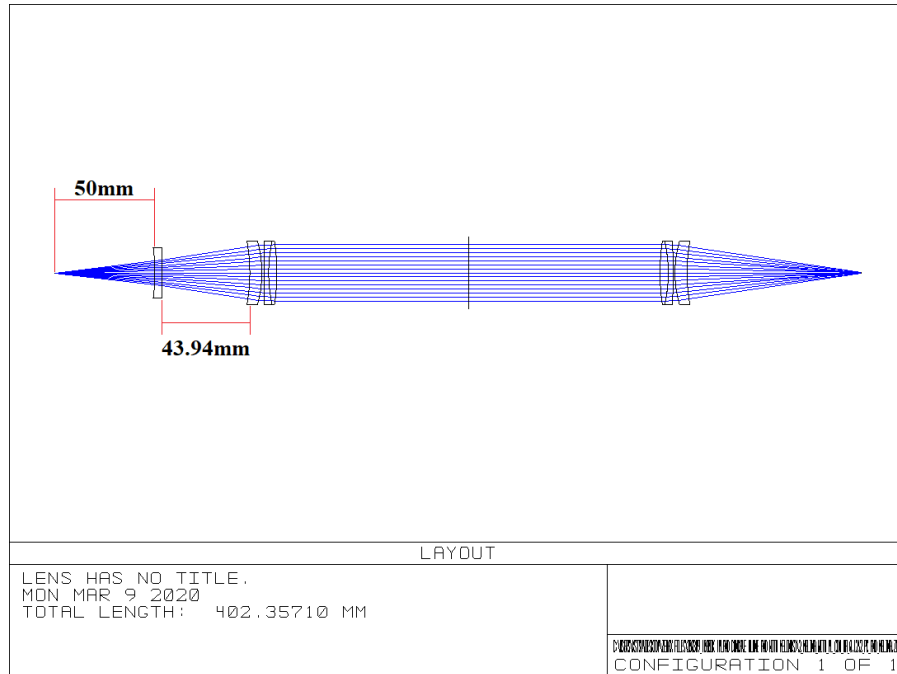

Fig. 46 *Optimized distance between the cavity and the imaging system.*

And the corresponding spot diagram for the optimized optical system is the following,
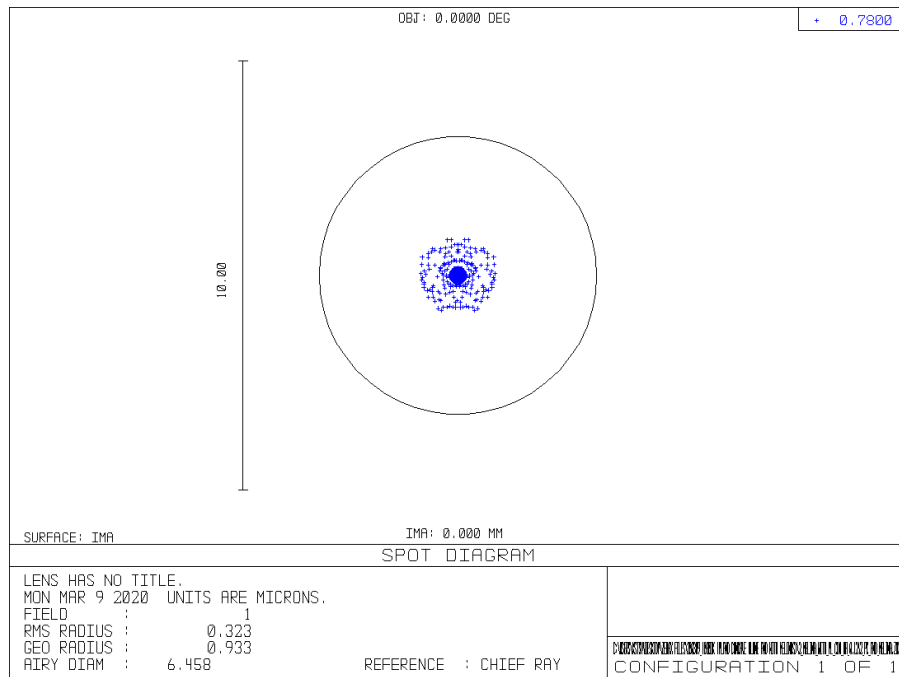
Fig. 47 *Spot diagram for the optimized optical system.*

All the rays fall inside the Airy disk which means that our optical system is diffraction limited and the resolution corresponds to an Airy disk diameter of 6.458µm.

Because we can't be sure that the specimen we want to image will be on the optical axis, we will also check for a source being off axis and see how the system deviates.

3.4.1.2 Source off axis by 1mm

Moving the source by y=1mm off axis, we see that not all rays from the source can pass through the optical system,

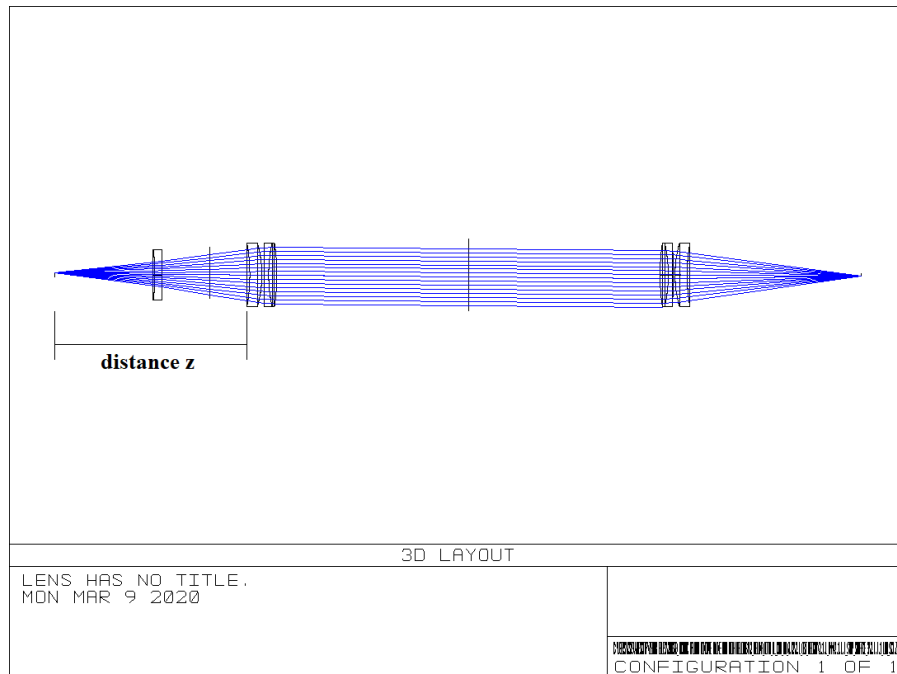**Fig. 48** *Layout for source at 1mm off axis.*

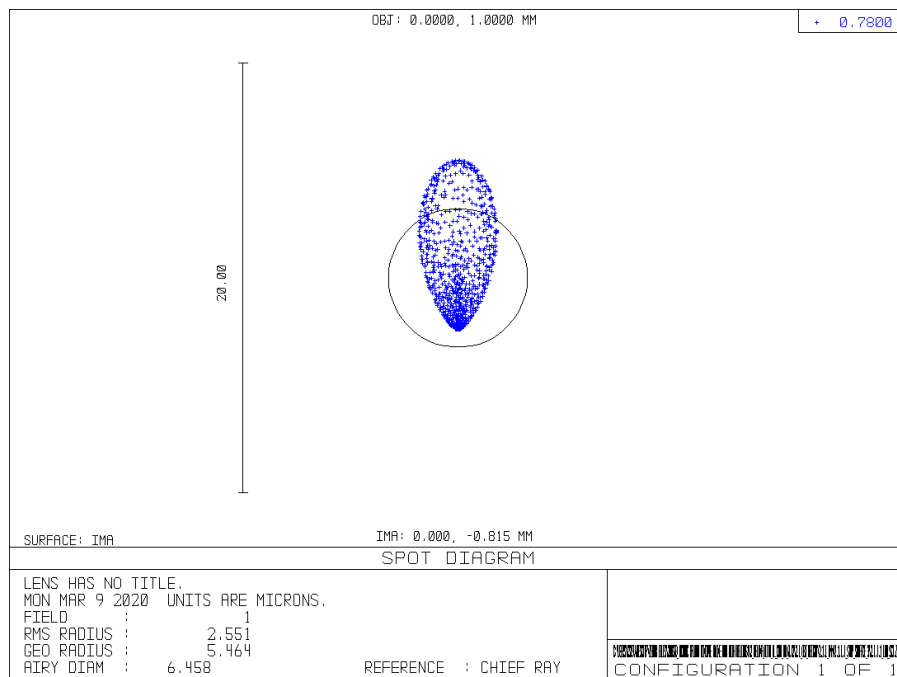And the corresponding spot diagram we get is,

Fig. 49 *Spot diagram for source at 1mm off axis.*

Which shows that the rays start to spread, extending beyond the Airy disk, and it seems to have introduced coma aberration, because we are off axis. To confirm that this is mainly due to coma aberration we tilt the imaging system, expecting in this case to fix the problem. So, we tilt the imaging system by angle θ equal to $\theta = \mathrm{atan}(y/z)$, where y is the height of the source from the optical axis (here 1mm off axis) and z is the distance pointed out in Fig.48. The tilting will be performed around x axis such that all rays pass again from the imaging system. In the following image all the axes are depicted and the part that was tilted is marked.
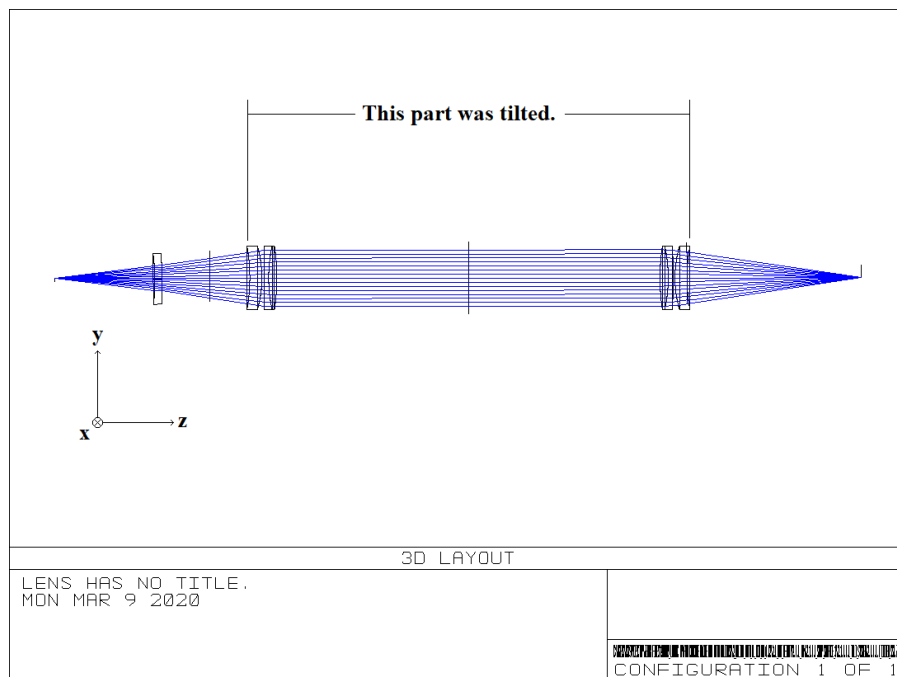

Fig. 50 *Layout for tilted imaging system.*

And the corresponding spot diagram we get is,

OBJ: 0.0000, 1.0000 MM   + 0.7800

20.00

SURFACE: IMA   IMA: 0.000, -3.054 MM
                                SPOT DIAGRAM

LENS HAS NO TITLE.
MON MAR 9 2020 UNITS ARE MICRONS.
FIELD   :   1
RMS RADIUS :   2.896
GEO RADIUS :   6.824
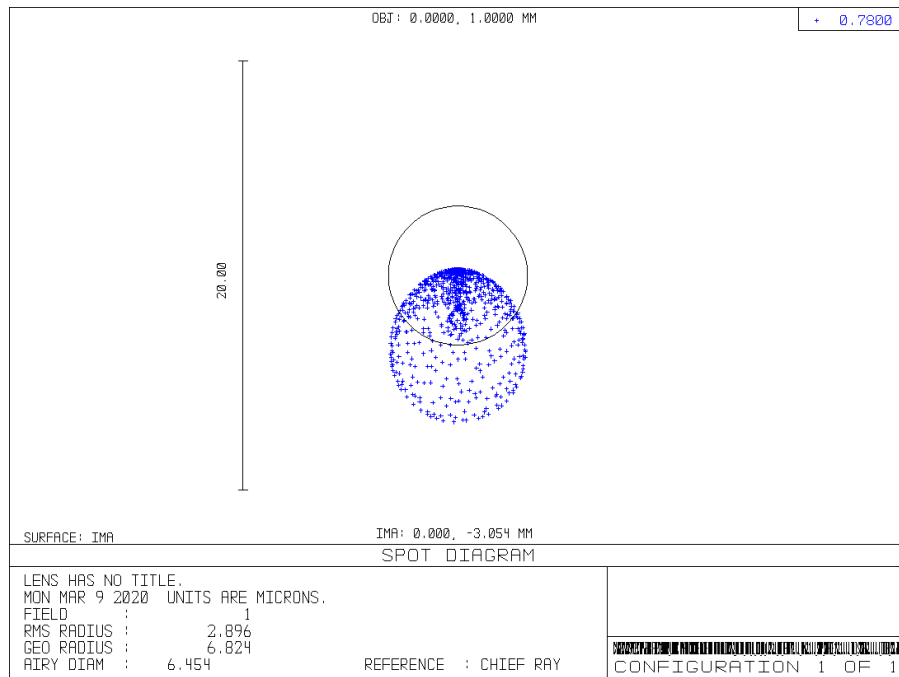AIRY DIAM :   6.454   REFERENCE : CHIEF RAY   CONFIGURATION 1 OF 1

Fig. 51 *Spot diagram for the tilted imaging system.*

Which seems to still suffer from some kind of aberration but the spot has improved on shape compared to that of Fig.49 and the RMS changes only slightly, when we perform tilting. Moreover, the spot is no more diffraction limited.

3.4.1.3 Source off axis by 2mm

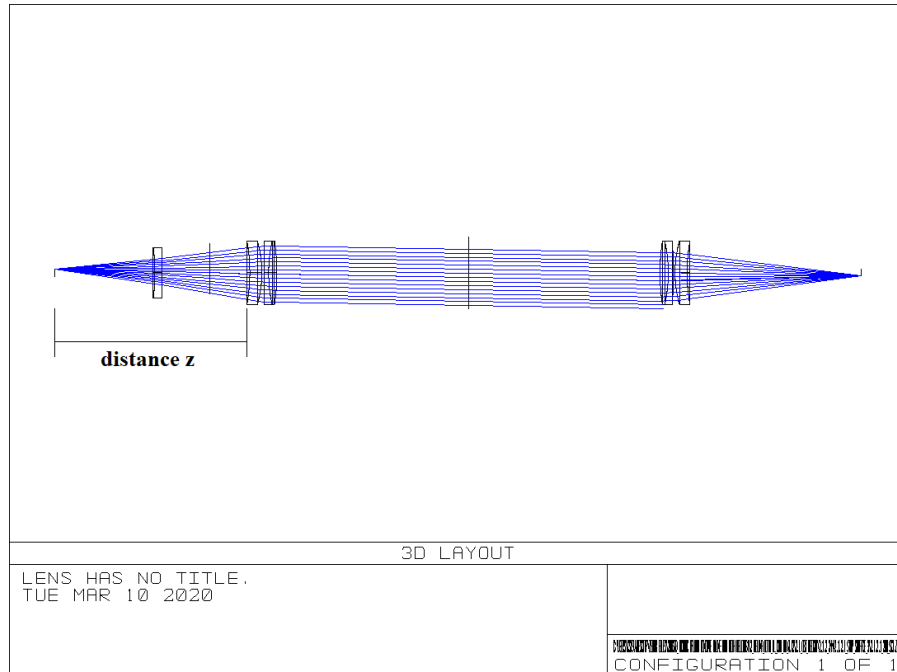Moving the source by y=2mm off axis, we see that not all rays from the source can pass through the optical system,

Fig. 52 *Layout for source at 2mm off axis.*

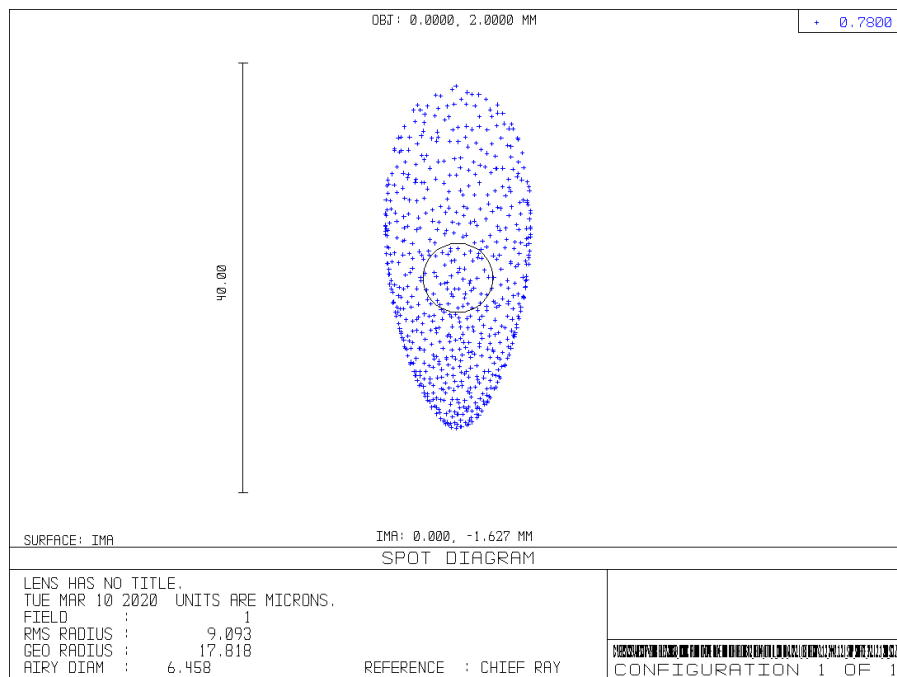And the corresponding spot diagram we get is,

Fig. 53 *Spot diagram for source at 2mm off axis.*

Which shows that rays spread out again, this time more than those in Fig.47 and it seems to have introduced coma aberration, because we are off axis. Again, the presence of coma aberration is confirmed since by tilting the imaging system, the problem is practically fixed. So, we have to tilt the imaging system by angle θ equal to $\theta = \mathrm{atan}(y/z)$, where y is the height of the source from the optical axis (here 2mm off axis) and z is the distance pointed out in Fig.52. The tilting will be performed around x axis such that all rays pass again from the imaging system. In the following image all the axes are depicted and the part that was tilted is marked.
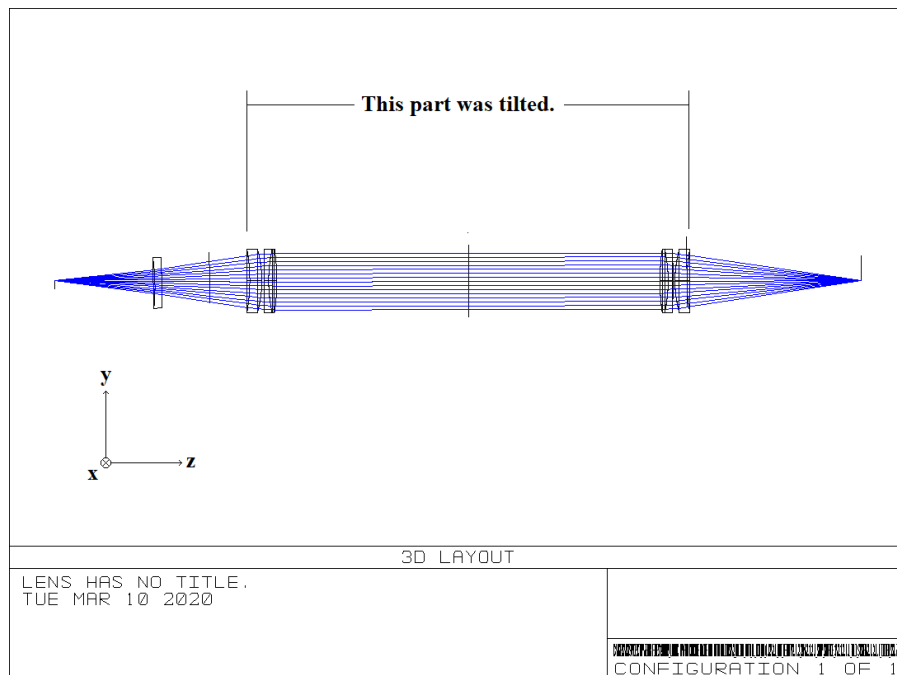

Fig. 54 *Layout for tilted imaging system.*

And the corresponding spot diagram we get is,

OBJ: 0.0000, 2.0000 MM   ⊹ 0.7800

100.00

SURFACE: IMA   IMA: 0.000, -6.109 MM
                                SPOT DIAGRAM

LENS HAS NO TITLE.
TUE MAR 10 2020   UNITS ARE MICRONS.
FIELD   :   1
RMS RADIUS :   9.124
GEO RADIUS :   20.239
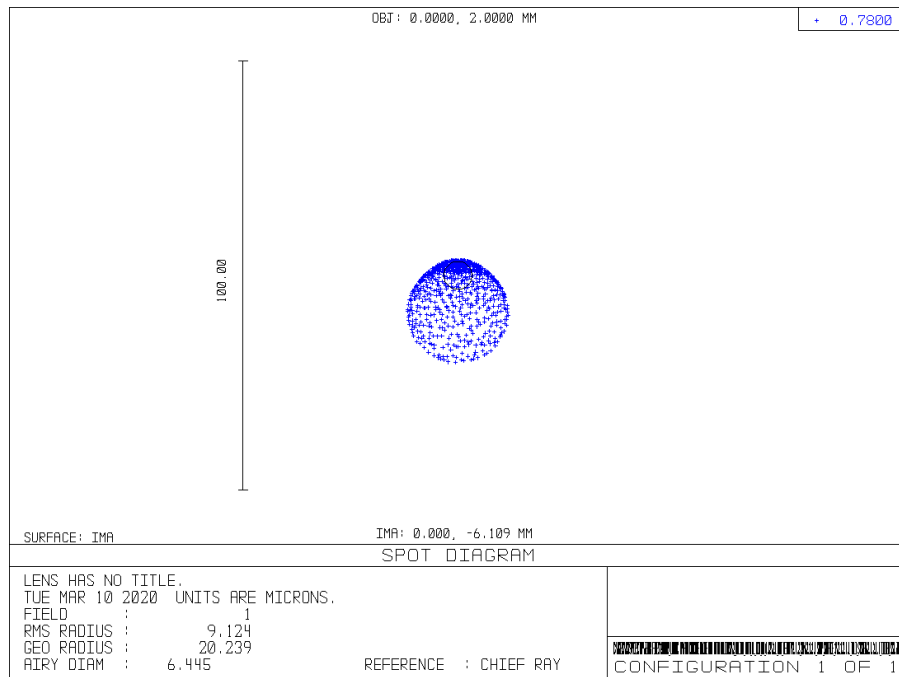AIRY DIAM :   6.445   REFERENCE   : CHIEF RAY   CONFIGURATION 1 OF 1

Fig. 55 *Spot diagram for tilted imaging system.*

Which seems to still suffer from some kind of aberration but the spot has improved on shape compared to that of Fig.53 and the RMS changes only slightly, when we perform tilting. Moreover, the spot is no more diffraction limited.

3.4.1.4 Source off axis by 3mm

Moving the source by y=3mm off axis, it is now clearer that not all rays from the source can pass through the optical system,
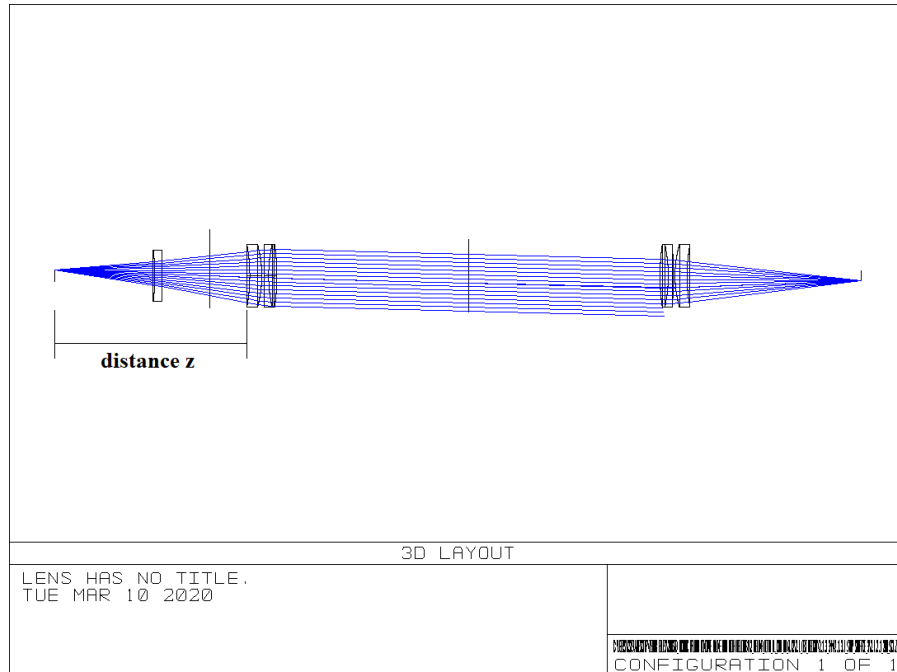
Fig. 56 Layout for source at 3mm off axis.

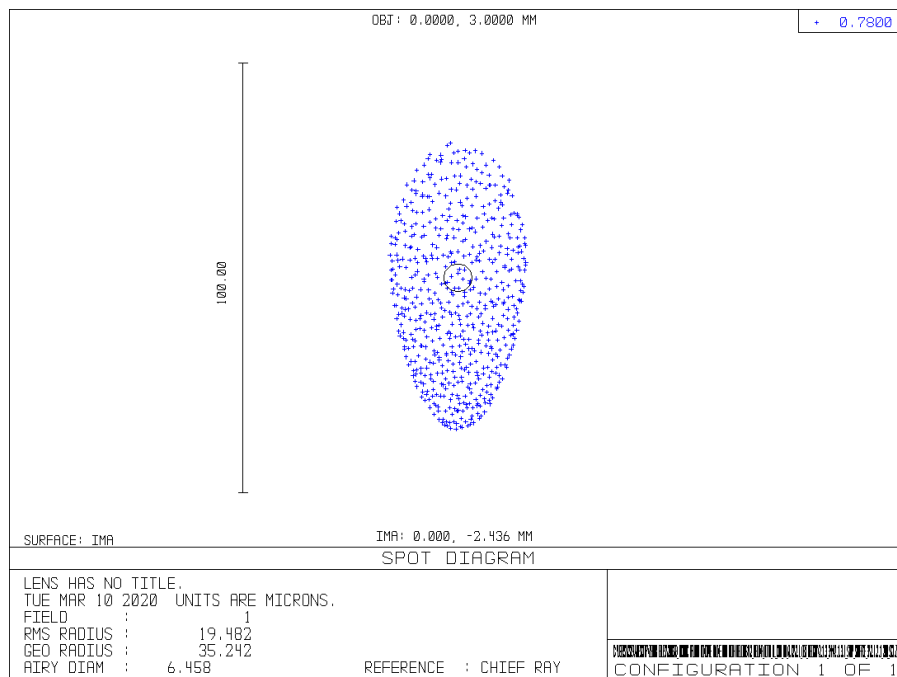And the corresponding spot diagram we get is,

Fig. 57 Spot diagram for source at 3mm off axis.

Which shows us that the rays spread way too much around the Airy disk and it seems to have introduced coma aberration, because we are off axis. Again, the presence of coma aberration is confirmed since by tilting the imaging system, the problem is practically fixed. So, we have to tilt the imaging system by angle θ equal to $\theta = \text{atan}(y/z)$, where y is the height of the source from the optical axis (here 3mm off axis) and z is the distance pointed out in Fig.56. The tilting will be performed around x axis such that all rays pass again from the imaging system. In the following image all the axes are depicted and the part that was tilted is marked.
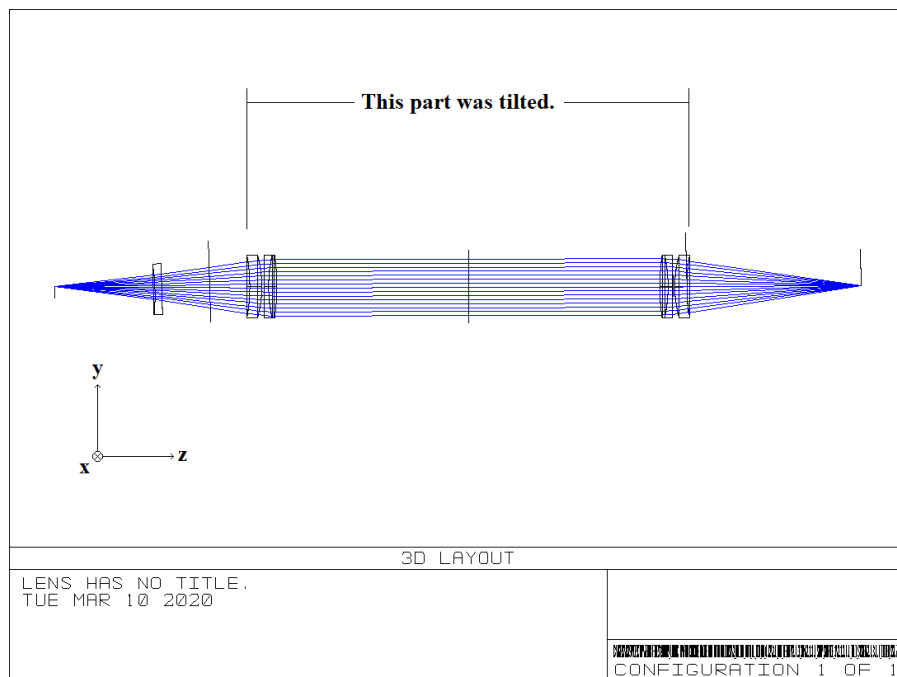

Fig. 58 *Layout for tilted imaging system.*
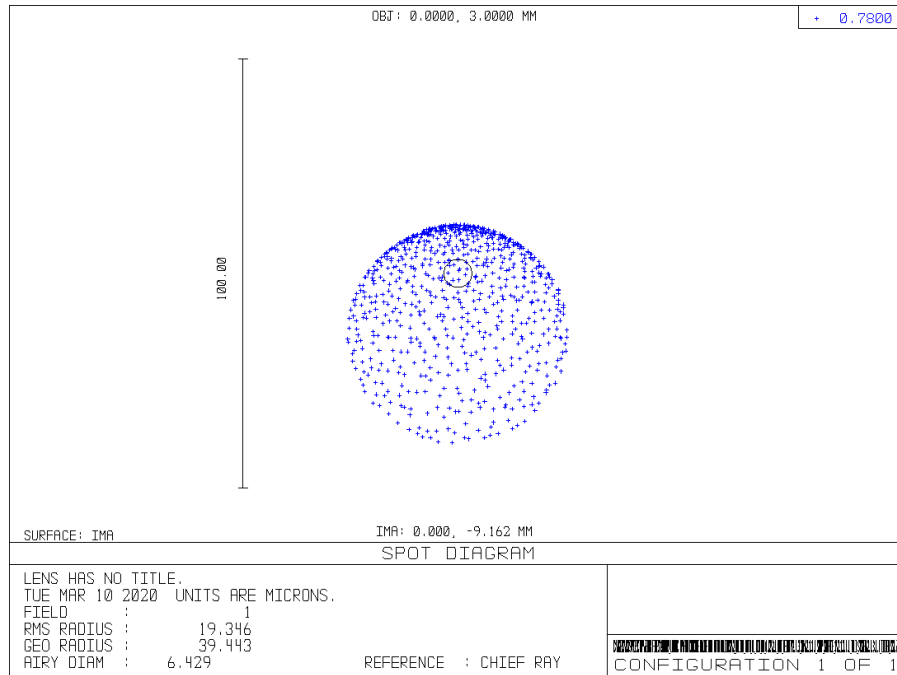
And the corresponding spot diagram we get is,

Fig. 59 *Spot diagram for tilted imaging system.*

Which seems to still suffer from some kind of aberration but the spot has improved on shape compared to that of Fig.57 and the RMS changes only slightly, when we perform tilting. Moreover, the spot is no more diffraction limited.

3.4.1.5 Annotation

As we have seen that using confocal cavity composed of two plano-concave mirrors accompanied with the imaging system presented in section 3.3, we manage to get a diffraction limited system, when the source is located on the optical axis. If the source starts moving away from the optical axis, some kind of aberrations start to appear (probably coma aberration), deforming the shape of the spot the rays create at the exit and spreading them out of the Airy disk. Tilting the imaging system, seems to improve the shape of the spot but the RMS radius of the rays does not show any improvement. The greater the distance of the source from the optical axis, the bigger the deviations appear to be. Last but not least, we would like to point out that the Airy disk diameter stays almost the same no matter the height of the source nor the tilting of the optical system.

3.4.2 Confocal Cavity composed of Zero-Lens Mirrors

Zero-lens mirrors are widely used to form optical cavities, because they do not produce much spherical aberrations. The two spherical surfaces of the zero-lens mirrors are of the same radius of curvature. In this section, we are going to use this kind of mirrors to check the performance of the cavity combined with the existing imaging system.

3.4.2.1 Source on the optical axis

In this section we will check the performance of a confocal cavity comprised of two identical zero-lens mirrors (Laseroptik - S-01090) which have radii of curvature $R_1 = -R_2 = -100mm$. This means that each mirror must have a distance of 50mm from the center of the cavity where we will place the specimen we want to image, as we can see in the next figure.
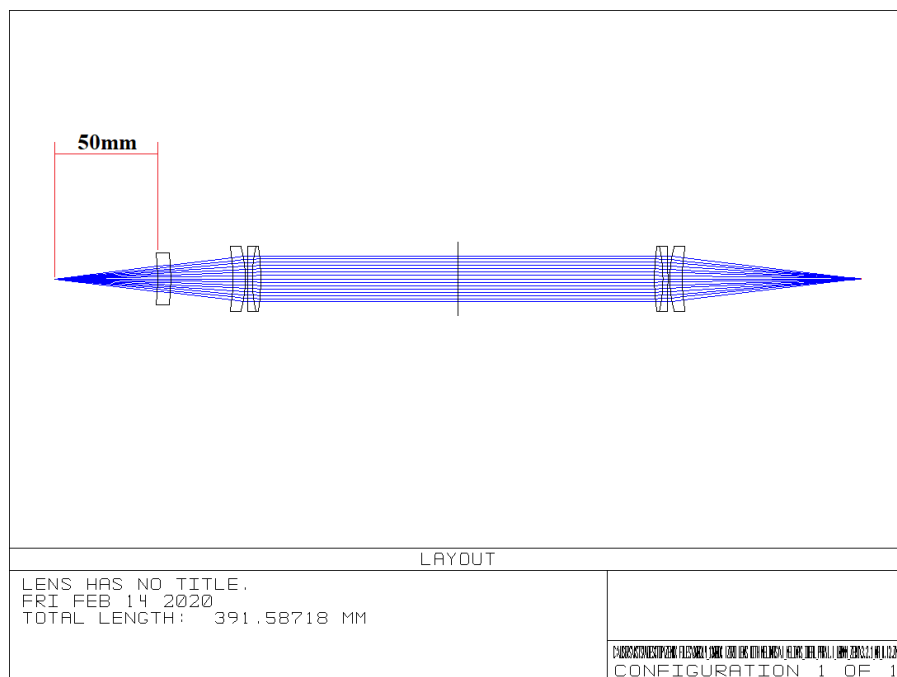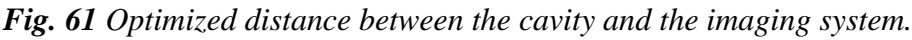

Fig. 60 *Layout of the confocal cavity combined with the imaging system.*

From now on, all optimizations are performed for NA=0.12 and λ=780nm.

We will now optimize the distance between the zero lens and the first element of the imaging system using merit function, in order to minimize the spot of the image at the end of the system.
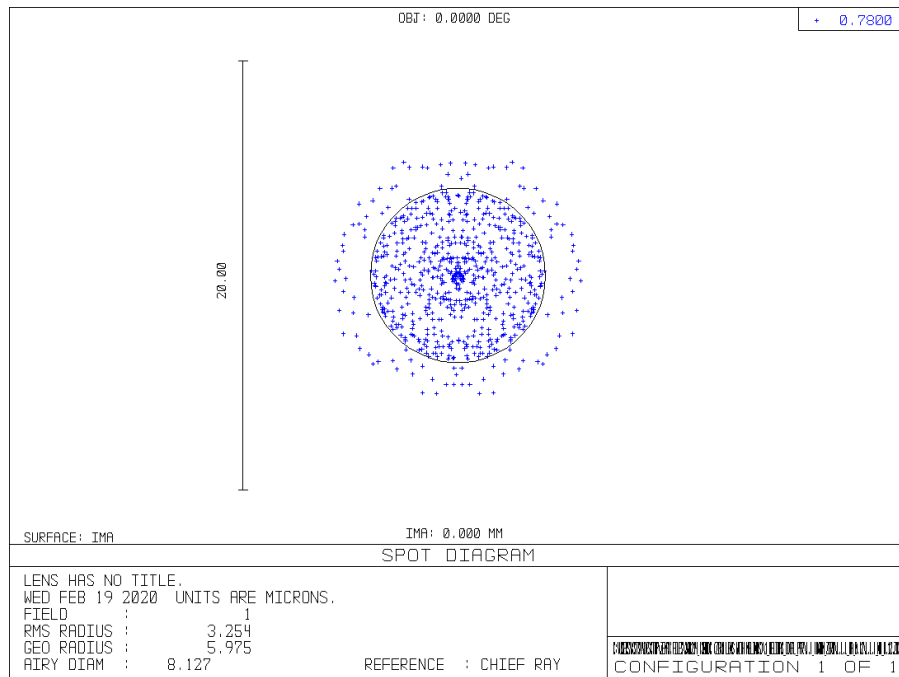
The optimal distance we find is 30.22mm, as it is depicted bellow. The rest of the distances not shown are the same as in Fig.42.

Fig. 61 *Optimized distance between the cavity and the imaging system.*

And the corresponding spot diagram for the optimized optical system is the following,

Fig. 62 *Spot diagram for the optimized optical system.*

As we can see, not all the rays fall inside the Airy disk which means that our optical system is not diffraction limited. Spherical aberrations that zero lens introduces are stronger than those of the plano-concave lens introduced in Fig. 47. Also, the resolution corresponds to an Airy disk diameter of 8.127μm while for the plano-concave arrangement was 6.458μm in Fig.47, meaning that optical system of Fig.61 has a worse resolution than the one in Fig.46.

In order to improve the spot size of Fig.62 we tried adding flat glass windows at the end of the imaging system, as one can see in the following image.
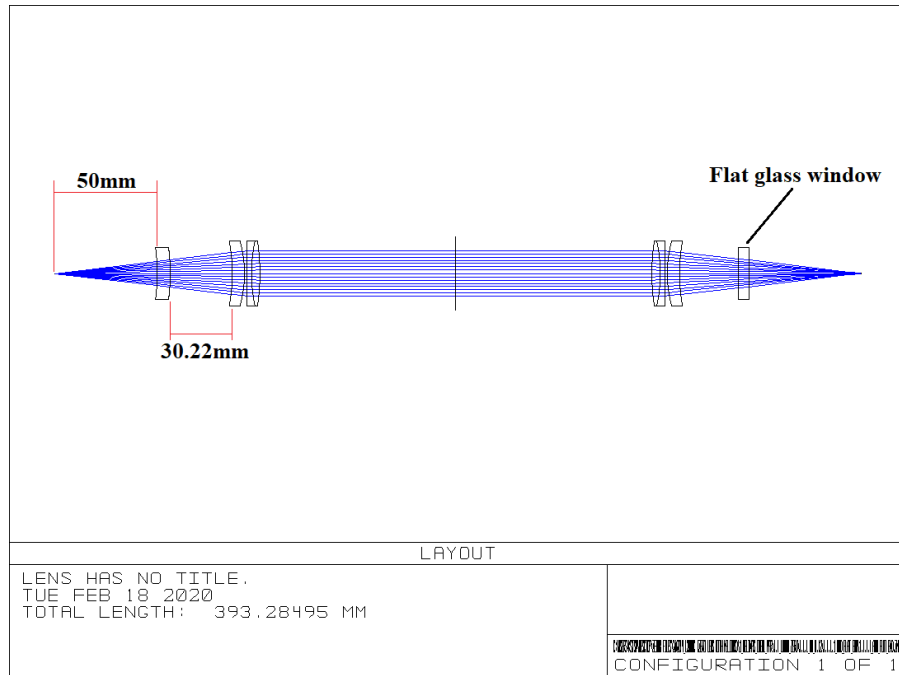
Fig. 63 *Layout of the imaging system with an extra flat glass window added at the end.*

And by introducing different thicknesses to the glass window, we observed how the spot size of Fig.62 was affected. What we found, was that for increasing thickness, the spot size was getting smaller until it reached to the diffraction limited case at some point.

Below, we have constructed a table showing the diameter D of the Airy disk and the RMS radius for different thicknesses T.

T(mm)	D(µm)	RMS(µm)
0	8.127	3.254
1	8.127	3.201
3	8.127	3.093
5	8.127	2.986
6.3	8.127	2.916
10	8.127	2.718
15	8.127	2.449
20	8.127	2.18

Table 3 *By changing thickness T of the flat glass window in Fig.63 we see that RMS radius of the spot in Fig.62 decreases while Airy disk diameter D, stays the same.*

We also plotted RMS radius as a function of thickness T using the data of Table 3.
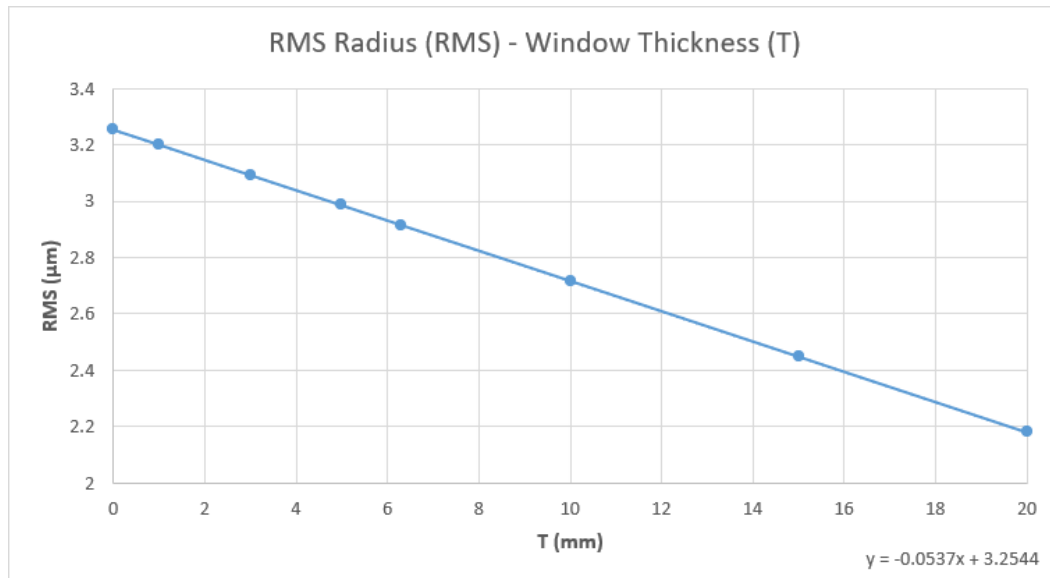

Fig. 64 *RMS radius as a function of thickness T of the flat glass window.*

What we found is RMS radius has a linear dependence with the thickness T of the flat glass window.

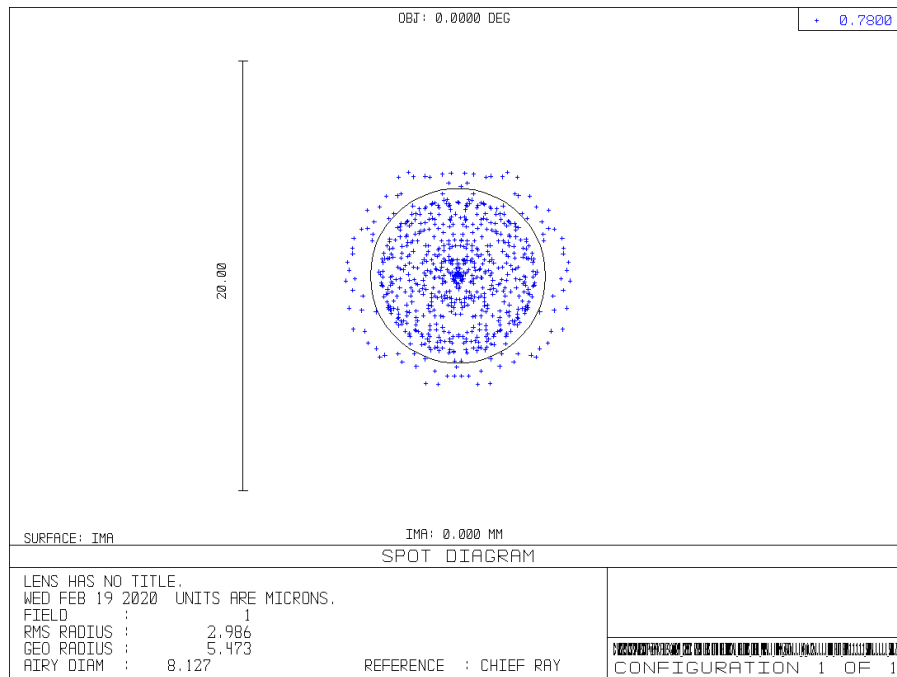We will now show some spot diagrams for different glass window thicknesses.

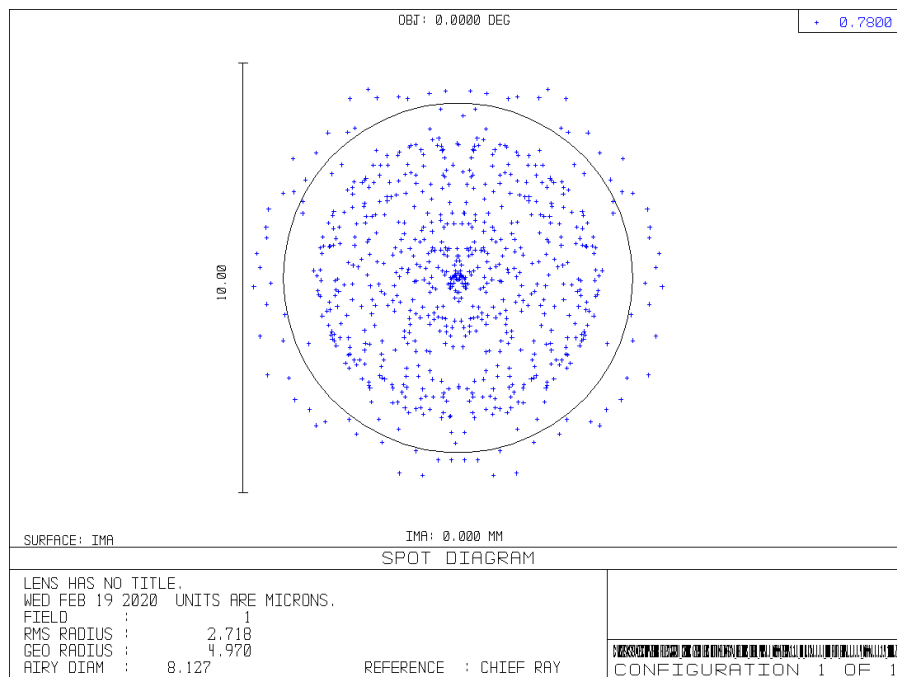**Fig. 65** *Spot diagram for 5mm flat glass window thickness.*

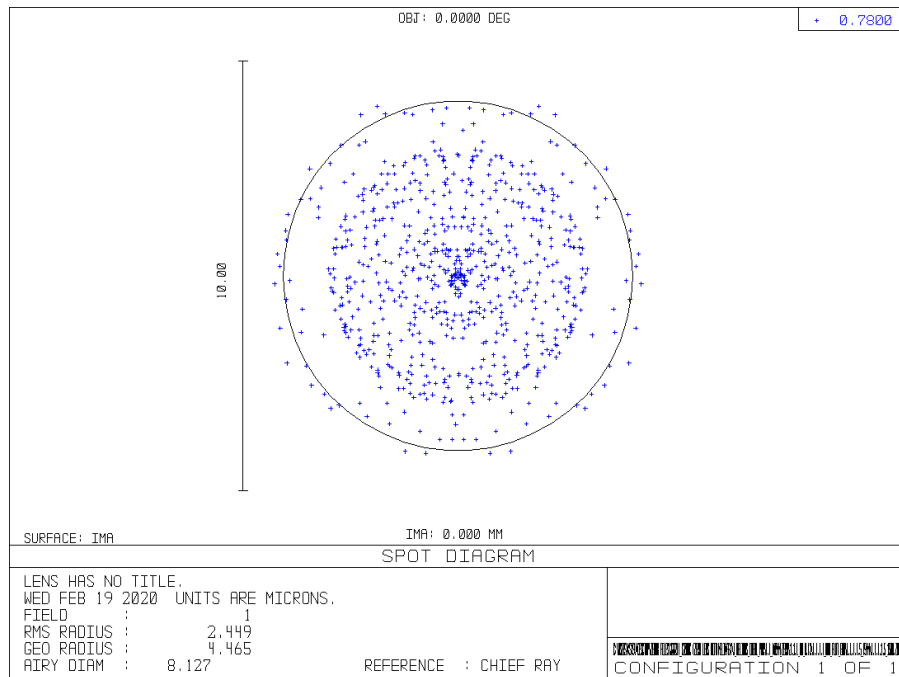**Fig. 66** *Spot diagram for 10mm flat glass window thickness.*

Fig. 67 *Spot diagram for 15mm flat glass window thickness.*
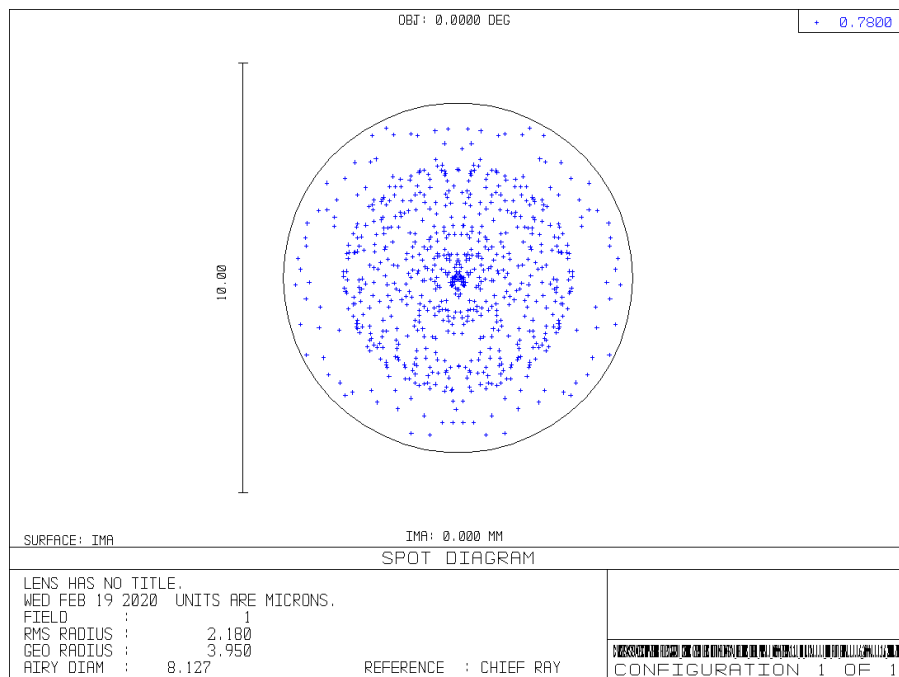

Fig. 68 *Spot diagram for 20mm flat glass window thickness.*

As we can see, for increasing window thickness, our system tends to the diffraction limit and for a window of 20mm thickness, we are already in the diffraction limited case.

3.4.2.2 Source off axis

As we saw in the previous section, by adding a flat glass window the system tends to the diffraction limit. We now want to see, how the system behaves with the flat glass at the end when the source is not located on the optical axis.

For glass window thickness of 3mm the on axis spot diagram is,
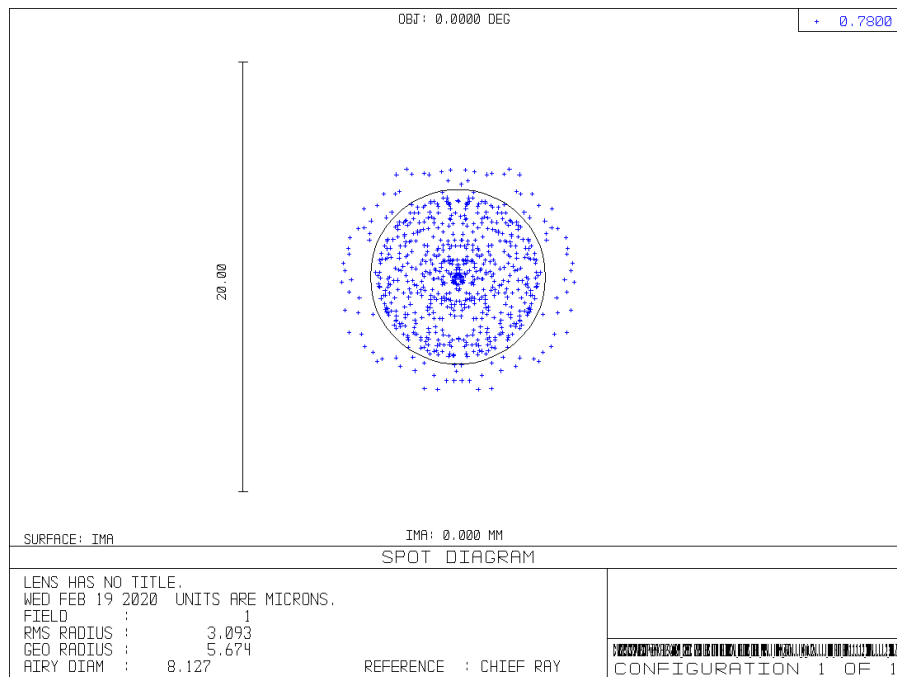

Fig. 69 *Spot diagram for 3mm flat glass window thickness and source on the optical axis.*

Moving the source by 1, 2 and 3mm off axis the spots we get, appear in the following figures.
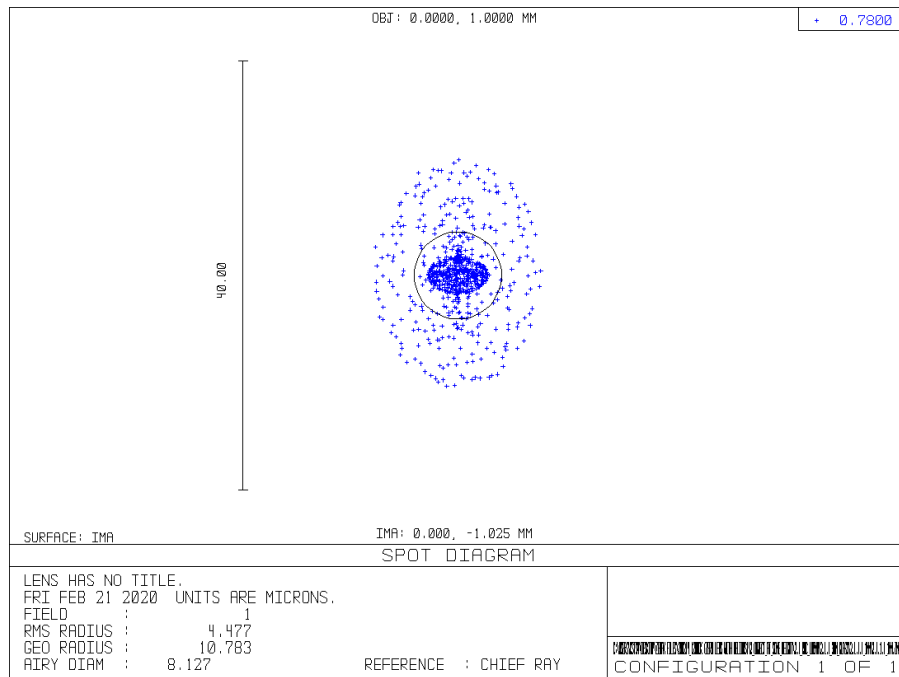
Fig. 70 *Spot diagram for 3mm flat glass window thickness and source 1mm off axis.*
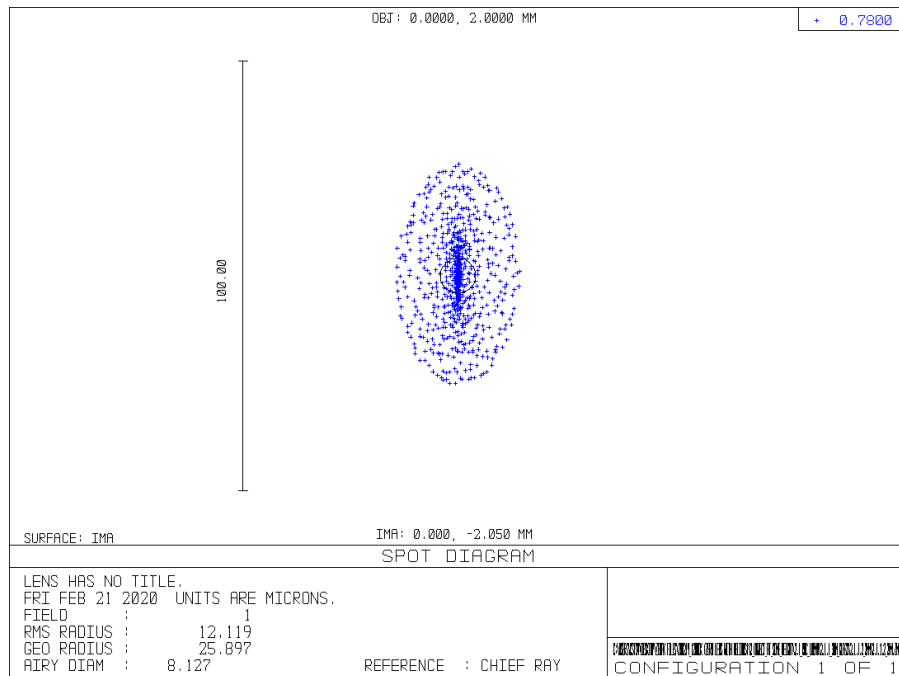
Fig. 71 *Spot diagram for 3mm flat glass window thickness and source 2mm off axis.*
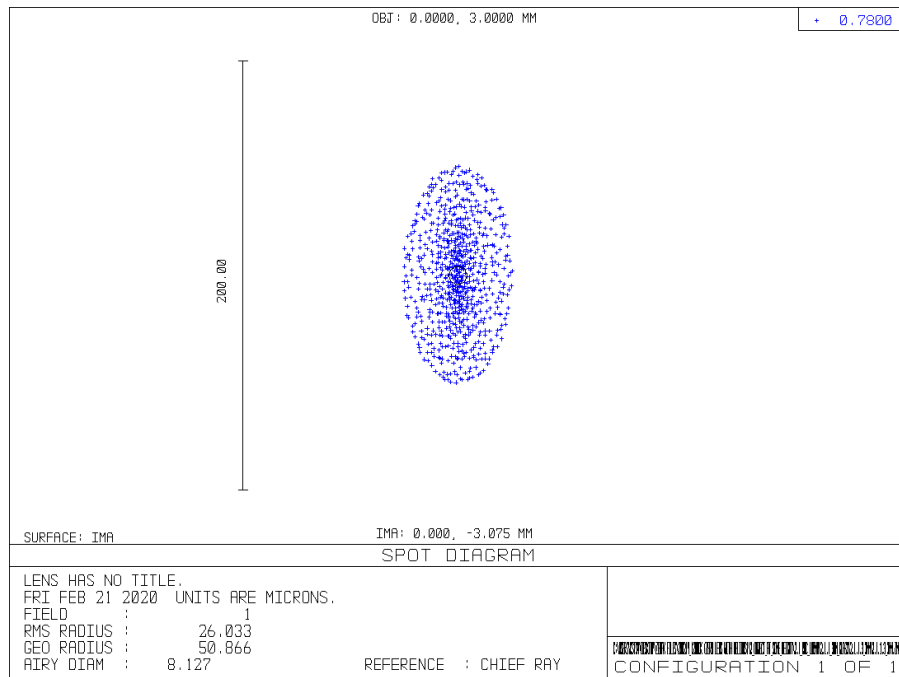
Fig. 72 *Spot diagram for 3mm flat glass window thickness and source 3mm off axis.*

It is obvious that more aberrations are introduced, but they do not seem to be the same as those in sections 3.4.1.(2-4). The rays seem to deviate in a same way both to the top and to the bottom. These do not seem to be coma aberrations so no tilting was performed here. The higher the distance of the source from the optical axis, the greater rays spread out of the Airy disk.

Chapter 4 – Experimental Study

As we described in Chapter 2, cavities are characterized by specific resonant axial modes. In this chapter we are going to check these resonant axial modes experimentally by presenting results of experimental studies performed in the BEC lab.

4.1 Cavity Modes

The purpose of this experimental exercise is to construct an optical cavity and by aligning a laser beam through the cavity to achieve resonance.

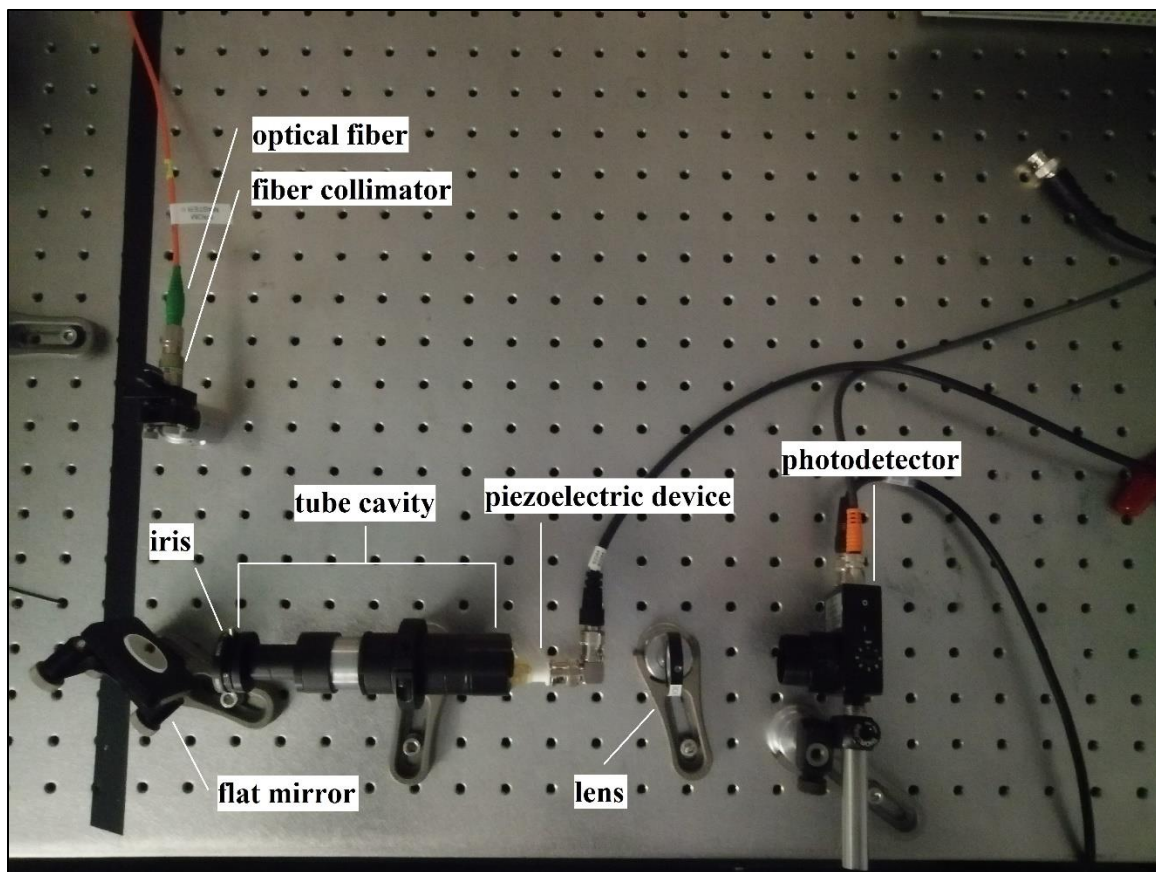The experimental arrangement can be seen in the following image, followed by a brief explanation.

***Fig. 73** Experimental arrangement.*

Laser beam (wavelength of roughly 780nm) enters the optical system through an optical fiber (PM780-HP - 770-1100 nm Polarization-Maintaining Fiber, 5.3 µm Mode Field Diameter) which is attached to a fiber collimator (60FC-4-A8-07 - Focal lengths up to 20 mm). This system is mounted in order to be able to steer the laser beam. What follows, is a mounted flat mirror (BB1-E03P - Ø1" Back Side Polished, Broadband Dielectric Mirror, 750 - 1100 nm) to reflect the beam at a 90 degrees angle. Then, laser beam enters the cavity which is comprised of a tube with mirror holders at the edges, roughly at 10cm distance between them. The attached mirrors are plano-concave with focal length of 50mm (CM127-050-E03 - Ø1/2" Dielectric-Coated Concave Mirror, 750 - 1100 nm, f = 50 mm). In the front end of the cavity, there is also attached an iris so that illumination is controlled, while in the back end of the cavity a piezoelectric (PZT) device is being attached in order to be able and control the length of the cavity. In the end, when light comes out of the cavity, it passes through a lens with focal length of 75mm, focusing the light in an amplified photodetector. Both photodetector and the piezoelectric device were attached to an oscilloscope.

When a proper alignment was achieved, the piezoelectric device was used (triangular pulse - frequency of 149.32 Hz) to make small changes to the length of the cavity and some resonance was found. A photo from the oscilloscope follows, showing the resonant peaks (yellow lines) and the triangular pulse (blue) infused in the piezoelectric device.

Fig. 74 *Photo from oscilloscope showing resonant peaks (yellow) and triangular pulse infused to the oscilloscope (blue). Horizontal axis measures time while vertical voltage.*

The piezoelectric device causes the mirror of the cavity to oscillate back and forth, changing the cavity length. In between the red lines that we have drawn in Fig.74, we can see the resonances of the cavity for one whole swipe for the mirror.

From Eq.(87) we know that the distance between two consecutive resonant peaks should be equal to $\lambda/2$. The wavelength used was 780nm, so the distance between two peaks in Fig.74 is equal to d_1=390 nm or d_1=0.39 μm.

From piezoelectric's device manual, we found that for every 1Volt, piezoelectric device displaces the mirror by 1μm. The peak to peak voltage of the blue pulse (from one red line to the other) in Fig.74 is 16.8 V, meaning that for that period of time, the mirror was displaced by d_2=1.68 μm.

Now, by dividing d_2 with d_1 we will find how many distances between two consecutive resonant peaks d_1 , should exist between the red lines in Fig.74.

Division gives 4.3 , rounded to the nearest integer we get 4. This means that we should see 4 whole distances d_1 , or else we should be able to see 5 resonant peaks.

Of course, as one can see, between the two red lines in Fig.74, we can see 5 resonant peaks in agreement with the analysis performed.

Conclusions

In this thesis, we have theoretically studied the operation of cavities and based on our analysis we have designed optical systems that involve the use of cavities, optimized to be used for imaging applications.

We performed numerical simulations to understand and visualize how light rays propagate inside optical cavities taking into account the stability of the cavity.

Based on the above we designed optical systems with integrated optical cavities. Our analysis shows that these systems seem to be well-behaved as far as the on axis optical aberrations are concerned. The first system we optimized, which contains a cavity comprised of plano-concave mirrors combined with the imaging system we introduced, behaves very close to the diffraction limit with minor spherical aberrations. On the other hand, the second one, composed of a cavity with zero-lens mirrors combined with the imaging system, is characterized by spherical aberrations which we eliminated by adding flat glass surfaces of different thicknesses at the back end of the whole system. In the off-axis cases we clearly see that coma aberration appears for the first system we checked. In the second system we see a more complex mixture of aberrations distorting the spot symmetrically to the top and to the bottom. The more distant the source from the optical axis, the greater these optical aberrations.

Moreover, we studied cavities experimentally and we observed the resonances inside a tube cavity with the help of a piezoelectric device. The theoretical analysis we performed agrees with the experimental observations, as we concluded in the fourth chapter.

Considering the work on this master thesis, the future of imaging using optical cavities is a promising technique.

Bibliography

[1]   J. Mertz, *Introduction to Optical Microscopy*. Cambridge University Press, 2019.

[2]   J. Hornak, *Encyclopedia of Imaging Science and Technology*. John Wiley & Sons, Inc., 2002.

[3]   M. Mueller, *Introduction to Confocal Fluorescence Microscopy*. 2005.

[4]   D. G. Papazoglou, "Notes of Postgraduate Course : Foundations in Modern Optics. (https://www.materials.uoc.gr/en/general/personnel/dpapa.html)." [Online]. Available: https://www.materials.uoc.gr/en/general/personnel/dpapa.html.

[5]   J. T. Verdeyen, *Laser Electronics*, 3rd ed. Prentice Hall, 1995.

[6]   A. E. Siegman, *Lasers*. University Science Books, 1986.

[7]   E. Hecht, *Optics*, 5th ed. Pearson Education, 2017.

[8]   M. Born and E. Wolf, "Principles of Optics." Cambridge University Press, 1999.

[9]   "Maxima." [Online]. Available: http://maxima.sourceforge.net/.

[10]   "Wikipedia - Gaussian beam." https://en.m.wikipedia.org/wiki/Gaussian_beam.

[11]   "Wikipedia - Longitudinal mode." https://en.wikipedia.org/wiki/Longitudinal_mode.

[12]   P. Török and F.-J. Kao, *Optical Imaging and Microscopy - Techniques and Advanced Systems*. Springer, 2007.

[13]   "Wikipedia - Airy disk." https://en.wikipedia.org/wiki/Airy_disk.

[14]   "Wikipedia - Angular resolution." https://en.wikipedia.org/wiki/Angular_resolution.

[15]   W. Smith, *Modern Lens Design*. McGraw-Hill Professional, 2004.

[16]   R. Kingsklake, *Applied Optics and Optical Engineering*, Vol. III. Academic Press, 1965.

[17]   "Wikipedia - Spherical aberration." https://en.wikipedia.org/wiki/Spherical_aberration.

[18]   J. Braat and P. Török, *Imaging Optics*. Cambridge University Press, 2019.

[19]   "Wikipedia - Coma (optics)." https://en.wikipedia.org/wiki/Coma_(optics).

[20]   "Zemax-OpticStudio Software." https://www.zemax.com/products/opticstudio.

[21]   M. Pappa, "Imaging Bose-Einstein Condensates at Ultra-Low Atom-Numbers and Time Averaged Adiabatic Potentials," *PHD Thesis*, no. June, 2011.